Title
Excited Electronic States and Ultrafast Dynamic Electron Trapping at Alkali Halide / Metal Interfaces

Author
Suich, David Edward Stuart

Publication Date
2015

Peer reviewed|Thesis/dissertation

Excited Electronic States and Ultrafast Dynamic Electron Trapping at Alkali Halide / Metal Interfaces

by

David Edward Stuart Suich

A dissertation submitted in partial satisfaction of the

requirements for the degree of

Doctor of Philosophy

in

Chemistry

in the

Graduate Division

of the

University of California, Berkeley

Committee in charge:

Professor Charles B. Harris, Chair
Professor Gabor A. Somorjai
Professor Alex Zettl

Fall 2015

Excited Electronic States and Ultrafast Dynamic Electron Trapping at Alkali Halide / Metal Interfaces

Abstract

Excited Electronic States and Ultrafast Dynamic Electron Trapping at Alkali Halide / Metal Interfaces

by

David Edward Stuart Suich

Doctor of Philosophy in Chemistry

University of California, Berkeley

Professor Charles B. Harris, Chair

Angle- and time-resolved two-photon photoemission is used to study the ultrafast electron dynamics at alkali halide-metal interfaces under ultrahigh vacuum conditions. The initial excited states and electron localization at trap states are characterized on the ultrafast timescales.

For NaCl on Ag(100), the well characterized island growth of NaCl on low Miller indices noble metal substrates in the ultrathin coverage limit is studied. The initial excited states observed correspond to the n = 1, n = 2, and n = 3 image potential state (IPS) progression of the NaCl-metal interface. The delocalized n = 1 IPS electrons, evidenced by their light effective mass, $m^* = 0.7m_e$, are found to localize via population transfer to two localized states on the hundreds of femtosecond timescale. The first localized state, indicated by its flat band dispersion, is located at the bottom of the free state band with a decay lifetime comparable to the free n = 1 electrons of $\leq$ 100 fs. The second, discrete, localized state observed leads to a binding energy gain of hundreds of meVs and results in a substantial lifetime increase of 0.5-1 ps versus the ca. 100 fs of the initial delocalized n = 1 IPS. The long-lived localized state's lifetime shows an exponential dependence with increasing coverage, indicating the NaCl film acts as a tunneling barrier and that the localized state is located at the surface-vacuum interface, versus inside the film. The long lived localized state is assigned to low coordinated defect sites on the NaCl surface such as step edges, corners, and NaCl pair vacancies. The binding energy and decay lifetime of electron trapping at low coordinated defects shows strong temperature dependence but qualitatively similar behavior for temperatures of 125-350 K.

A new emerging trap state is observed at the NaCl/Ag(100) upon cooling to temperatures $\ll$ 125 K. This state is only observed after long time delays ($\geq$ 500 fs) and at increased binding energies of 380 meV. Additionally, the emerging trap state shows an even further enhanced lifetime of a few picoseconds. A transition temperature for observing this state is identified as 81 K or 7 meV of thermal energy. Furthermore, the emerging state is shown to arise from electron population transfer from trapped electrons at low coordinated defect sites.

In temperatures > 100 K, the lifetime of electrons trapped at low coordinated defect sites decreases as temperature increases due to thermally activated tunneling back to the metal. However, the reverse behavior is observed for the same state for temperatures < 90 K, where cooling results in a *decreased* lifetime. At this temperature regime, which overlaps with the observed transition temperature, the emerging trap state opens an additional pathway of decay for electrons trapped at low coordinated defect sites, resulting in the observed decreased lifetime with decreasing temperature. The emerging trap state is assigned to small polaron formation via low coordinated defect intermediates. Polaron formation only becomes stable via defect intermediate at two-dimensional interfaces, whereas the electron small polaron is known to be unstable in a bulk perfect NaCl crystal.

Finally, these results are generalized for other alkali halide systems (KCl, NaF, RbCl) on Ag(100) which show qualitatively similar behavior. The above results are also shown for NaCl on Cu(111) and Ag(111). NaCl on Cu(111) shows a clear image potential state progression through the n = 4/5, providing conclusive evidence the initial excited states predominately correspond to the IPS and not the conduction band of NaCl. On both Cu(111) and Ag(111) substrates, the emerging trap state at low temperatures is observed, revealing that this phenomenon is not system specific. In qualitative agreement with polaron formation observed for NaCl on Ag(100), on Ag(111), and on Cu(111), polaron formation results in binding energy increase of ca. 400 meV, an enhanced lifetime of an order of magnitude greater than electrons trapped at low coordinated defect sites, and is only observed at temperatures < 100 K.

To my parents, Paul and Cynthia Suich, and to Ann P. Suich (Grams) and the late John E. Suich (Big John)

Contents

List of Figures

Acknowledgments

I would not be at the end of graduate school without the support and help of a number of people. I was fortunate to have many great academic advisers. First off, I would like to thank Charles Harris. Charles provided me the opportunity to explore scientific questions with independence. He always placed his highest confidence in his students and afforded me many unique opportunities. I would also like to thank Rich Saykally, whose interest in me and chance to have frank and fruitful discussions have meant a great deal to me. Finally, I would like to thank my undergraduate adviser, Durwin Striplin. His teaching, passion, and belief in me are the reason I pursued a Ph.D. in chemistry. I am grateful for his friendship and ability to call him anytime when graduate school seemed to be getting the better of me.

I owe a great thanks to the people who were my greatest source of scientific training and education and have spent innumerable hours with over the years; my co-workers on the Surface Side. When I joined the group, Eric Muller was the senior on surface side. Eric was an excellent mentor who made the difficult transition of starting graduate school a lot smoother. I am grateful to maintain his friendship after his leaving and our continued encounters in Colorado or Berkeley. I owe my scientific training, accomplishments, and example of a good scientist to Ben Caplins more than anyone. Ben set the standard for attention to detail, mastery of equipment troubleshooting and fixing, and comprehensive knowledge of two-photon photoemission. Ben was not only my greatest source of scientific learning, but also introduced me to backpacking and the beauty of the Sierra Nevadas, and for this and more, I am indebted to him. I also want to thank Alex Shearer, my fellow last of the Harris graduate students, for his companionship in the last year together and pursuit of data.

I also had the great pleasure of overlapping with many Liquid Side members. Jacob Schlegal brought a deep appreciation for good food and drink. Adam Hill always displayed an enthusiasm for science. Matt Zoerb and I shared a love for southern goodness and bourbon. Son Nguyen set the standard for a hard work ethic. And while Justin Lomonts mastery of geography may have been rather limited, his kindness and support certainly were not.

I could not imagine graduate school and life in Berkeley without Erich and Caroline Kreutzer. We all moved to Berkeley after graduating Davidson College, and while I did not have deep friendships with either in college, they quickly became one of those rare friendships that likens to family. They made California home for me, and I have shared with them numerous adventures, Thanksgiving feasts, intensively competitive games, and an ongoing 7 year bet. They have shown me an extraordinary degree of love and patience in those dark days known as the final years of graduate school. I am forever grateful for them. When I was not third wheeling, I was fifth and seventh wheeling with Callan and Ken Elswick Fockele and Zack and Catherine Stergar. Their friendship and support made graduate a lot more fun and gave me an escape from life in dungeon level of Hildebrand.

Above all, I wish to thank my parents. They have always been my biggest supporters, and their devotion and unconditional love are the only reason I could obtain my Ph.D. They

have afforded me every opportunity grow and learn. They have spent countless hours on the phone providing wisdom and comfort, and when graduate school was most difficult and full of uncertainty, they were a constant source of security. I am blessed to have them for parents. My brothers optimism and confidence is something I always wish to emulate. Last but not least, I wish to thank my grandmothers, who have both played an active role raising and shaping who I am. Ann Suich (Grams) took me on my first visit to Berkeley and throughout life has opened my world beyond the confines of my childhood.

This work was supported by the Director, Office of Energy Research, Office of Basic Energy Sciences, Chemical Sciences Division of the U.S. Department of Energy, under Contract No. DE-AC02-05CH11231.

Chapter 1

Introduction

1.1 Introduction

The behavior of electron excited states at interfaces of dissimilar materials is of crucial importance to a variety of fundamental and technological fields of study. Photoexcitations at metal or semiconductor surfaces and adsorbates lead to desorption and dissociative processes important to photocatalytic reactions such as water splitting on TiO_2 [1], oxidation of carbon-monoxide [2], and a wide variety of photochemical transformations [3, 4]. Such processes involving the photoexcited electron transfer into dissociative states represent a large research front in the search for efficient materials for solar fuels such as H_2 from water splitting and formation of hydrocarbons from CO_2 reduction [5, 6]. Electron and hole transfer across interfaces is also a crucial step in the operation of numerous molecular electronic technologies such as organic field effect transistors, organic light emitting diodes (OLED), and organic photovoltaics (OPV).

Simplified schematics of an OPV and OLED devices are shown in Figure 1 to highlight the importance of interfacial charge carrier behavior to device operation. The operation of an OPV can be broken down to four steps [7, 8]. (1) Sunlight enters the OPV through a transparent anode where upon adsorption by the donor material leads to exciton formation. (2) The exciton, a tightly bound electron hole pair, subsequently diffuses to the donor/acceptor interface. (3) Electron transfer to the acceptor material creates a charge transfer state needed to dissociate the exciton whose Coulombic attraction is $\gg$ thermal energies. (4) After subsequent dissociation in free carriers, electrons and holes, the charges are collected at their respective electrodes for current generation. Currently, each step of this process is the focus of active research in the organic electronics community. Often cited as a source of poor efficiency in OPVs is the inefficient exciton separation at the donor/acceptor interface [9]. However, for such a crucial step in device operation, there exists an ongoing debate over different models and mechanisms of exciton dissociation. Two prominent competing models are that exciton dissociation occurs through a manifold of charge transfer states (CTS), where the initially populated higher energy CTS are more delocalized than the thermally

equilibrated ground CTS, and therefore dissociation only occurs through 'hot' CTS states [9, 10, 11]. The competing mechanism largely comes from theoretical modeling that find the disordered energetic landscape and band bending effects can efficiently dissociate an exciton in thermally equilibrated CTS [12, 13].

The issues highlighted above serve to emphasize the crucial importance of electron dynamics at the interface of dissimilar materials. However, the work herein by no means answers or solves the highlighted technological challenges. Early on, the focus was on the observation of excitonic states in donor materials such as α-ω-dihexyl-sexithiophene (DH6T) and 6,13-Bis(triisopropylsilylethynyl)pentacene (TIPS-pentacene) in order to subsequently study exciton dissociation at donor/acceptor interfaces. After many failed attempts to observe excitons in prototypical small molecule donor materials, focus shifted to creating a thin insulating layer to establish an exciton blocking layer that would decouple the exciton in the donor material from the metallic substrate. However, the ultrafast electron dynamics at the insulator/metal interfaces studied proved to be interesting and full of rich physics in their own right. The work presented in this thesis seeks to understand and characterize the electronic states and dynamics present at metal/alkali halide interfaces. Such systems lay an important groundwork for the emerging field of microelectronics.

1.2 Electronic States at Metal/Adsorbate Interfaces

The electron dynamics and transport across interfaces will be largely governed by the energetic location, coupling and interaction between interfacial electronic states present. The various electronic states at interfaces can be broadly broken down into three categories. The first of these is derived from the adsorbate's electronic structure, while the other two are derived from the metal.

Adsorbate States

The first class of observable electronic states includes those derived from the adsorbate. One common example observed in TPPE experiments is the highest occupied molecular orbitals (HOMOs) and lowest unoccupied molecular orbitals (LUMOs) of small molecule organic semiconductor adsorbates such as thin films of C_{60} on Cu(111) [14], monolayer films of lead phthalocyanine (PbPc) on graphite substrates, pyridine films $>$ 1 ML on Cu(111) [15], and 3,4,9,10-perylene-tetracarboxylic acid dianhydride (PTCDA) on Ag(111) [16]. While the above observations of molecular LUMOs involve exciting an electron from the substrate into the molecular unoccupied states, excitonic states involving the intramolecular excitation from the HOMO into the LUMO are also observed. The difference between exciting an electron into the LUMO from the substrate versus the HOMO is often distinguished by the electronic bandgap and optical bandgap, respectively. The optical bandgap is typically energetically less than the electronic bandgap due to the strong Coulomb attraction between the photoexcited electron and intramolecular hole versus the electronic bandgap observed in

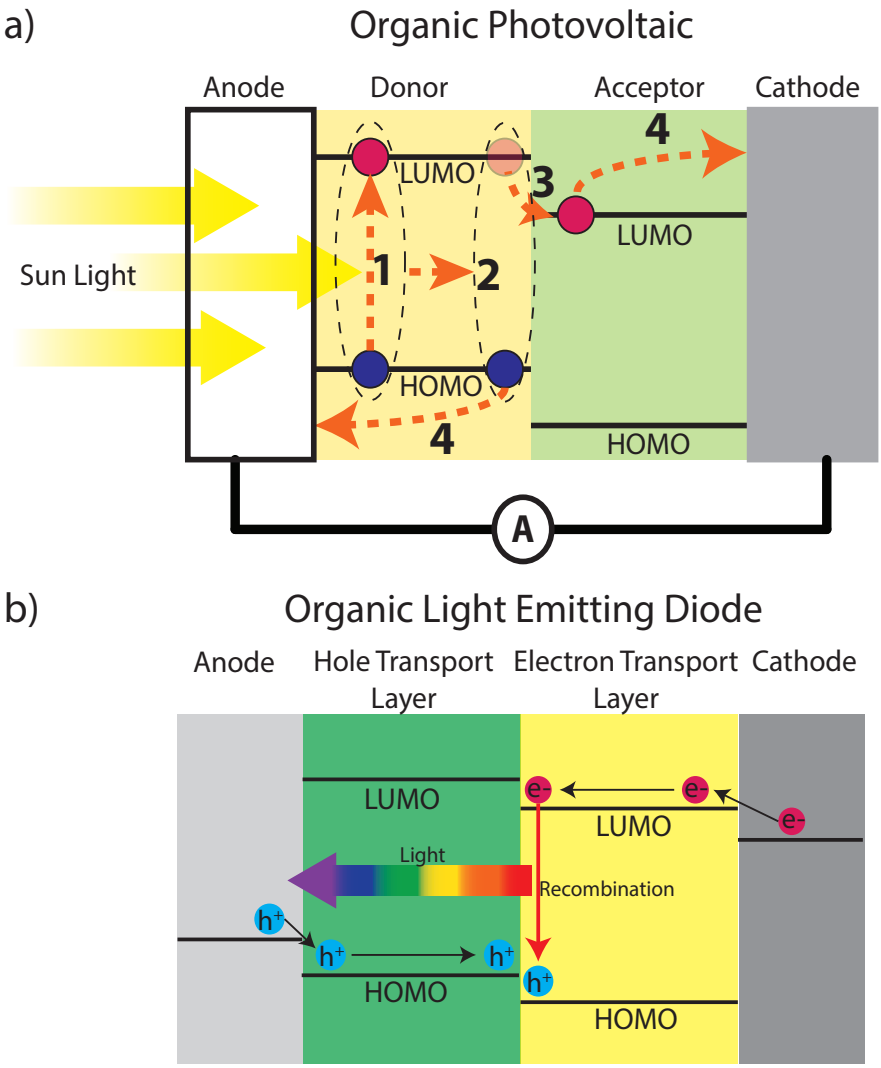

Figure 1.1: (a) Simplified diagram of organic photovoltaic operation (see text). Sunlight adsorption in donor leads to formation of exciton (1) which diffuses to the interface (2) where the electron transfers to the acceptor material forming charge transfer state (3), after which further dissociation results in free charges that travel to electrodes to produce a current (4). (b) Simplified diagram of OLED. Holes injected into the HOMO of the HTL and electrons injected into LUMO of ETL diffuse to interface, where upon recombination, tunable light is emitted.

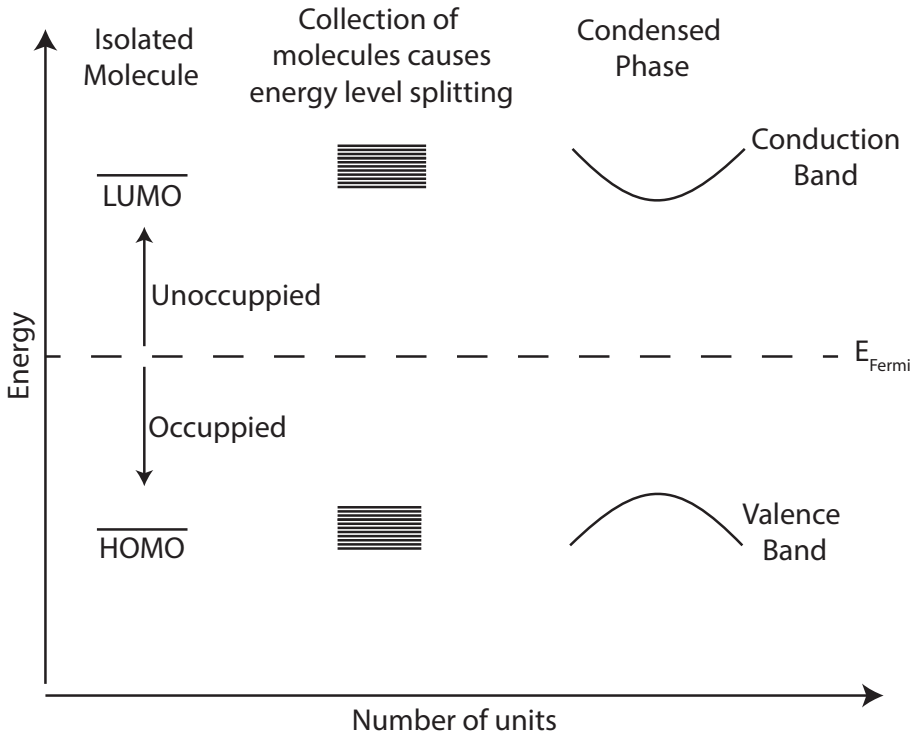

Figure 1.2: Simplified illustration describing electronic bands in the solid state. A large collection of n units each contribute n HOMO/LUMO or atomic orbitals, which leads to a splitting of energy levels. This forms a large collection of energetically overlapping states to form a continuum or band. Thus the HOMO becomes the valence band and LUMO becomes the conduction band in condensed matter.

two-photon photoemission where the substrate hole is screened by the metallic free charges. Excitons in thin film adsorbates have been observed for oligothiophene and sexithiophene [17, 18], and copper phthalocyanine (CuPc) [10].

While chemists think in terms of individual molecular orbitals (HOMO and LUMO), the realm of condensed matter physics for large periodic systems is concerned with the material's valence and conduction bands. When a large number, n, of repeat units come together to form a solid, each unit contributes its own HOMO/LUMO or atomic orbitals. As n approaches a large limit, each of these n states is split in energy and forms a continuum of energetic states referred to as a band [figure 1.2]. See the article "How Chemistry and Physics Meet in the Solid State" by Roald Hoffmann for a detailed description of electronic bands in solids [19]. Two-photon photoemission studies have observed the conduction bands of clean Si(111) and Si(001) surfaces [20], and amorphous ice layers on metal substrates [21, 22]. More recently, two-photon photoemission studies have characterized the highly correlated topological states of the well-studied topological insulator Bi_2Se_3 [23] and Bi_2Te_3 [24, 25].

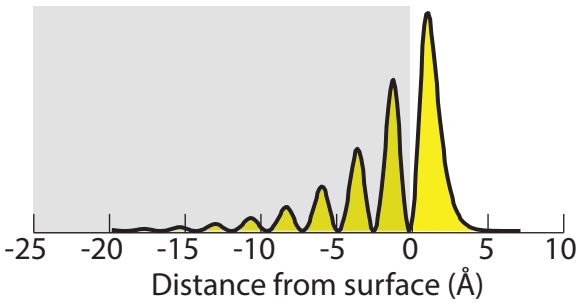

Figure 1.3: Wavefunction for the Shockley surface state of Ag(111).

Shockley Surface State

The next two classes of electronic states at metal/adsorbate interfaces are those intrinsic to the metal and arise due to the broken translational symmetry of the bulk at the surface. The first of these is the Shockley surface state, which arises as a new solution to the Schrödinger equation that occurs from the broken symmetry in the crystal potential. This state resides energetically within the bulk bandgap below the Fermi level [26]. The wavefunction for the Shockley surface states is characterized by having Bloch-like character with an exponentially decaying envelope inside the metal and by an exponentially decaying portion approaching the surface into the vacuum [27]. The calculated wavefunction for Ag(111) is depicted in figure 1.3, which reveals the state is located primarily at the surface with some portion decaying into the vacuum. These states are characterized by a light electron effective mass, $m^* \approx 0.5m_e$, where $m^* = 1m_e$ represent a free electron. These states are observed as occupied states for the (111) facets of noble metal surfaces. For Ag(111) the Shockley surface state has an effective mass of $m^* \approx 0.4m_e$ [28, 29] and located 63 meV below the Fermi level (E_F) [29], and for Cu(111), the state is located 435 meV below E_F with $m^* = 0.41m_e$ [29] or 390 meV below E_F and $m^* = 0.46m_e$ from reference [30]. However, for Ag(100), which much of this dissertation utilizes, the Shockley surface state is > 3 eV below E_F, and therefore experimentally inaccessible in these experiments [31].

Image Potential States

The second class of electronic states intrinsic to metal surfaces is the image potential states (IPS). These are unoccupied states that arise from the abrupt change in the dielectric constant at the surface, rather than derived from the electronic structure as in the case of the Shockley surface state, and are therefore more ubiquitous in time-resolve photoemission experiments. Image potential states were first discussed by Cole and Cohen [32], and then later experimentally proven by Grimes and Brown [33] for liquid helium. Echenique and Pendry subsequently extended their predicted existence to metal surfaces [34]. The observation and characterization for metal surfaces and metal/adsorbate interfaces has since been an active research area by many groups using two-photon photoemission and inverse photoemission.

For a more detailed description, see the excellent reviews by Fauster and Steinmann [35], Echenique [36, 37], and Chulkov [38, 39].

Conceptually, image potential states arise from an electron residing in the vacuum near the surface of a medium inducing a polarization of charges (figure 1.4). The induced polarization can be treated by the method of images, where a charge of equal and opposite magnitude, $+\beta$q, is located behind the mirror of the surface plane and replaces the polarization. The term β is determined from the static dielectric constant, ϵ, of the medium, and is equal to $\frac{(\epsilon-1)}{(\epsilon+1)}$. For a metal or perfect conductor, $\beta = 1$. The resulting Coulombic attraction between the electron and its image charge leads to the image potential which equals,

$$V_{im}(z) = -\frac{q^2}{16\pi\epsilon_0 z}.$$

The image potential (for an electron) is exactly one-fourth of the Hydrogen atom due to two factors: (1) the distance between the electron and its image charge is 2z rather than z and (2) because no electric fields exists inside a metal, the integration occurs from the surface (z = 0) to $+\infty$ instead of -∞ to $+\infty$. This analogous situation to the Hydrogen atom gives rise to a Rydberg series of states, labeled by a principle quantum number n, which are bound and converge to the Vacuum level. The energies of the IPS are expressed as

$$E(n) = E_{vac} - \frac{0.85eV}{(n^2 + a)},$$

where a is the quantum defect parameter. The binding energies are reduced by a factor of 16 compared to the Hydrogenic states. The wavefunctions of the first two image potential states, n = 1 and n = 2, were simulated by Benjamin Caplins for Ag(111) and Ag(100) and shown in figure 1.5. One finds that IPS wavefunctions reside primarily in vacuum, are localized and bound perpendicular to the surface, and are similar to the radial wavefunctions of the Hydrogen atom. An important feature of IPS wavefunctions is that the expectation value based on the hydrogenic model scale as

$$\langle z \rangle = 3.17n^2 \mathring{A},$$

which means the n = 1 IPS will be primarily located 3.17 Å outside the surface. Therefore, this will serve as a sensitive probe to any changes in the surface potential arising from an adsorbate. This will prove to be an important feature for this work.

While the electron is strongly bound perpendicular to the metal surface, the electron shows a very a weak interaction parallel to the surface. Models describing image potential states typically treat the perpendicular and parallel directions separately, where the potential parallel to the metal surface is effectively flat. This results in plane-like wavefunctions parallel to the surface, ψ(x) $\propto e^{(-ikx)}$, where k is a continuous index for wavevector of the crystal momentum. The total energy for the electron will then be a sum of the perpendicular and parallel components,

$$E_{total} = E_n + \frac{(\hbar k)^2}{2m_e}.$$

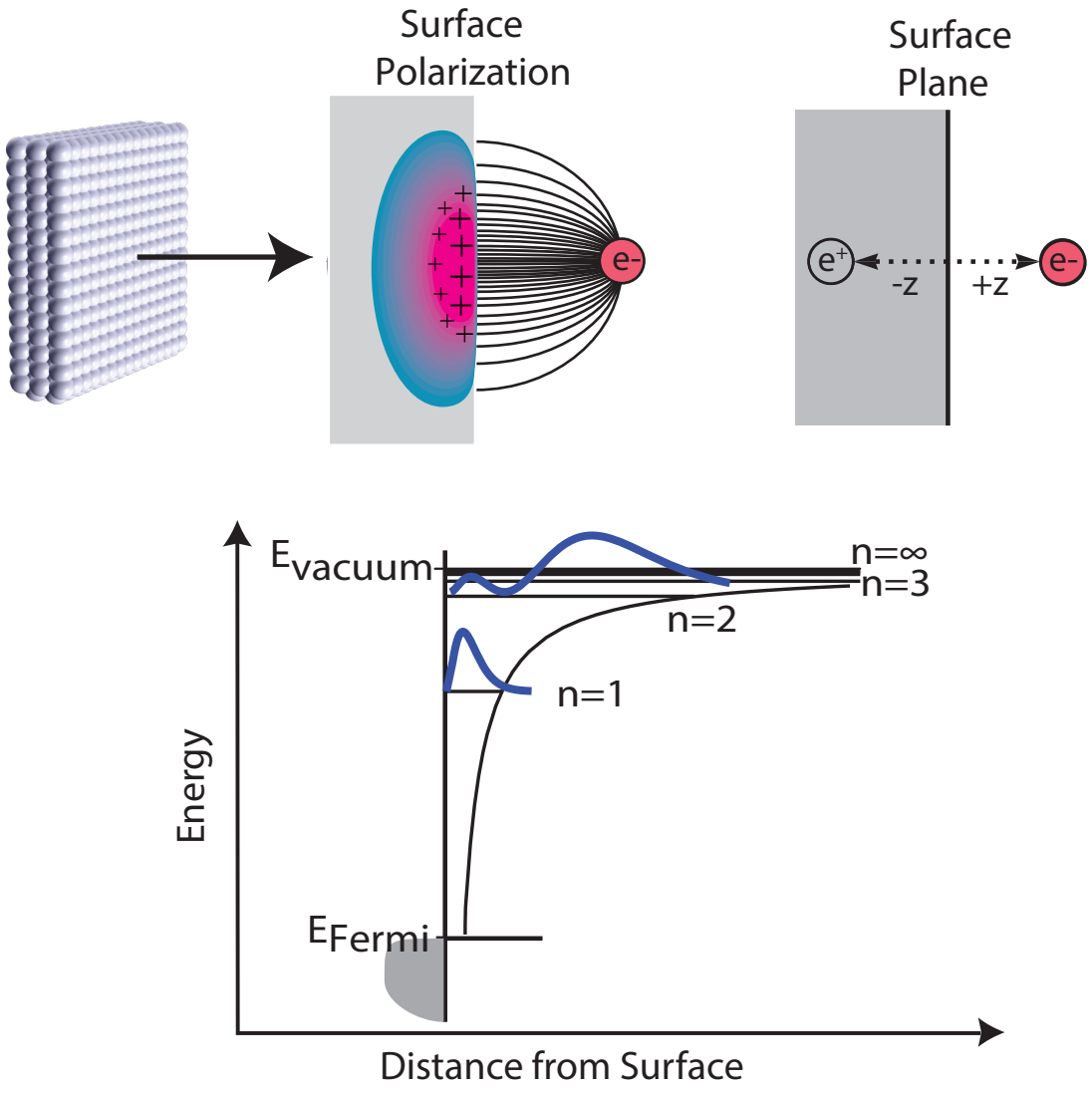

Figure 1.4: A photoexcited electron in the vacuum induces a polarization of free charges in the metal resulting in a Coulombic attraction. The polarization can formally be treated by the method of images, and gives rise to the image potential. The image potential, which is $\propto \frac{1}{z}$ perpendicular to the metal surface, is isomorphic to the hydrogen atom, and gives rise to a Rydberg series of states converging to the vacuum level labeled with the principle quantum number, n.

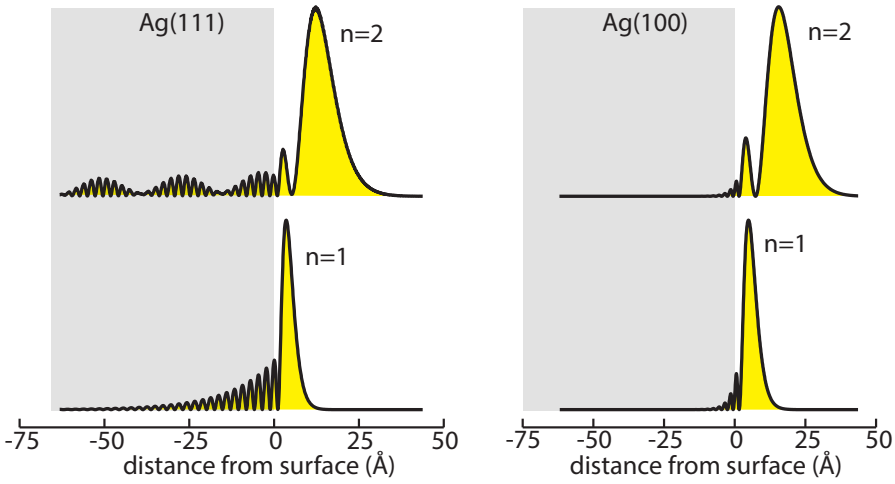

Figure 1.5: Wavefunctions for the n = 1 and n = 2 IPS calculated using a one-dimensional model provide by Chulkov for Ag(111) and Ag(100).

Treating the electron as 'free' parallel to the surface is supported by momentum-resolved measurements that typically measure the effective mass of IPSs on clean metal surfaces as $m^* \approx 1m_e$, i.e. a free electron.

1.3 Angle- and Time- Resolved Two-Photon Photoemission (TPPE)

The technique by which the excited states and ultrafast electron dynamics of metal surfaces and interfaces are probed is two-photon photoemission (TPPE). This is an ultrafast optical pump-probe spectroscopic technique that measures photoemitted electrons as a function of time, energy, and momentum. Unlike Ultraviolet Photoemission Spectroscopy (UPS), TPPE is capable of observing both occupied and unoccupied states. A schematic for the TPPE process is presented in figure 1.6. In TPPE, a pump pulse, $h\nu_1$, excites an electron from below the Fermi to an unoccupied or virtual intermediate state. Typically, the pump pulse energy will be less than the workfunction of the sample, Φ, so as to prevent one photon photoemission. After a variable time delay, $\Delta t = t_i\text{-}t_f$, a probe pulse, $h\nu_2$, will photoemit the intermediate electron into the vacuum, where its kinetic energy (KE) is measured by a time-of-flight spectrometer. Knowing the probe pulse energy and kinetic energy, one can determine the binding energy (BE) = $h\nu_2$ - KE of the intermediate state referenced to the vacuum or Fermi level. Having an absolute energy reference allows TPPE to distinguish between transitions with similar optical gaps, whereas in other pump-probe techniques, such as transient adsorption, two transitions with similar gaps would appear isoenergetic and therefore indistinguishable.

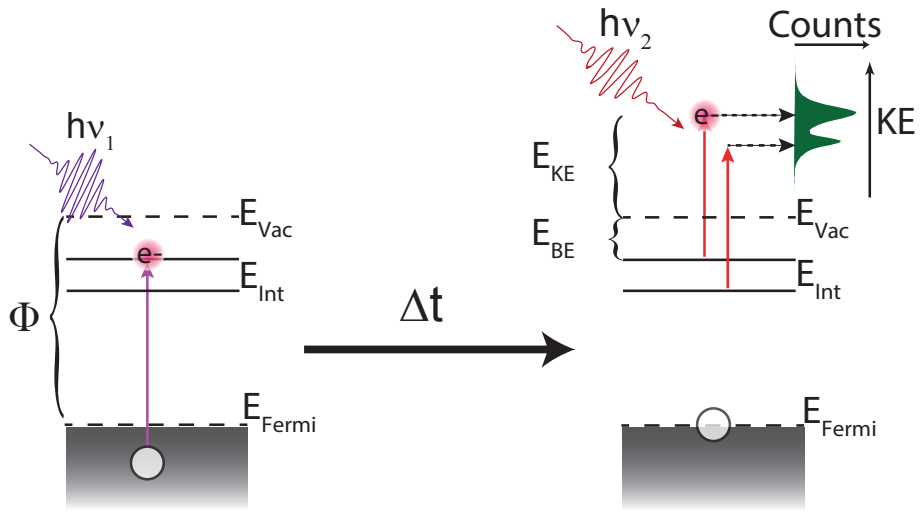

Figure 1.6: Schematic representation of two-photon photoemission. An initial pump pulse, hν_1, excites an electron from below the Fermi to an intermediate state. After a variable time delay, Δt, a probe pulse, hν_2, photoemits the intermediate state electron into the vacuum and its kinetic energy is measured by time-of-flight analysis.

In this implementation of TPPE, a visible pulse is provided by an optical parameteric amplifier, which is subsequently frequency doubled in a Beta-barium borate (βBO) crystal to provide a second, ultraviolet (UV) pulse. For intermediate state lifetimes $\gg$ 100 femtoseconds (fs), the ordering of the UV and visible pulse in the pump-probe sequence will be apparent. However, for lifetimes $\leq$ 100 fs, which pulse serves as the pump or probe will be unclear. Performing a wavelength dependence of the photoemitted electron kinetic energy will allow one to assign the pump and probe pulse to the UV and visible pulse. Additionally, it will determine if the intermediate state is a real unoccupied state or an occupied state photoemitted via two photon adsorption through a virtual state. Changing the tunable visible pulse, hν_1, by a known energy, Δhν, will change the UV, hν_2, pulse energy by 2Δhν. For intermediate states photoemitted by the visible pulse, the kinetic energy will change by Δhν, whereas intermediate states photoemitted by the UV pulse will change by 2Δhν. Photoemission from initial occupied states by two-photon adsorption will change by 3Δhν.

What separates TPPE from other pump-probe spectroscopies is its ability to carry out momentum-resolved measurements in an angle-resolved version of the technique. The total momentum of the photoemitted electron can be divided between the perpendicular and parallel momentum components, labeled by $\hbar$k$_\perp$ and $\hbar$k$_{||}$, respectively. Upon photoemission, the parallel momentum of the electron, $\hbar$k$_{||}$, is conserved. This is due to the fact that light carries a negligible momentum relative to the electron, and that the periodicity of the potential parallel to the surface is invariant in the surface normal direction. The perpendicular component of the momentum, however, is not conserved because the potential changes as

the electron crosses the surface barrier. Due to the conservation of the parallel momentum, the interfacial band-structure can be mapped out by varying of the angle of the sample with respect to the detector axis. Varying the sample angle allows picking out various slices of parallel momentum through the relation,

$$k_{||} = \frac{\sqrt{2m_e E_{kin}}}{\hbar} \sin\theta,$$

where m_e is the mass of a free electron, E_{kin} is the electron's kinetic energy, θ is the angle of sample with respect to the detector, and $k_{||}$ is the parallel wavevector. The relationship between energy and $k_{||}$ is referred to as the state's dispersion or its two dimensional band structure, and is given by,

$$E_{kin}(k_{||}) = E_{n(k_{||}=0)} + \frac{\hbar^2 k_{||}^2}{2m^*},$$

where m^* is the state's electron's effective mass. In dispersion measurements, the effective mass is the fitted parameter obtained from experiments, and reflects the band curvature of the intermediate state. One of the important implications of the observed effective mass is its indication of the extent of the wavefunction's delocalization or localization in the plane of the sample. For free-electron, delocalized states, the band dispersion will show a parabolic relationship between energy and increasing angle, and $m^* \approx 1$, i.e. a free-electron. However, for a spatially localized state, $E(k_{||})$ is independent of $k_{||}$, and the dispersion shows a flat band with $m^* \gg 1$. The angle-resolved TPPE schematic is represented in figure 1.7. Additionally, dispersion measurements can be carried out in a time-dependent manner that allows the observation of electron localization in two-dimensions as will be discussed in the following section.

1.4 Dynamic Electron Localization

Much of the results of this work concerns the localization of electrons on ultrafast timescales, and therefore a brief overview of electron localization in two-dimensions is presented. The first distinction to make is whether the localized state observed is a result of static or dynamic localization. Static localization refers to direct population of a localized state. Static localization was observed for the n = 1 IPS of 1 ML C_{60} on Cu(111) due to confinement by a surface dipole arising from metal charge transfer to C_{60} [40]. Static localization was also observed for the n = 1 IPS of ultrathin layers of benzene on Ag(111), which was due to structural disorder in benzene films [41]. Finally, static localization was observed for the non-dispersive LUMO of methanethiolate on Ag(111) in ultrathin coverages, which became dispersive (delocalized) upon thicker coverages. This behavior was attributed to a phase transition, where in ultrathin limit, the methylthiolates lie flat on the surface, and at thicker coverages, become upright, resulting in a decreased nearest-neighbor distance and increased overlap integral creating a dispersive band [42].

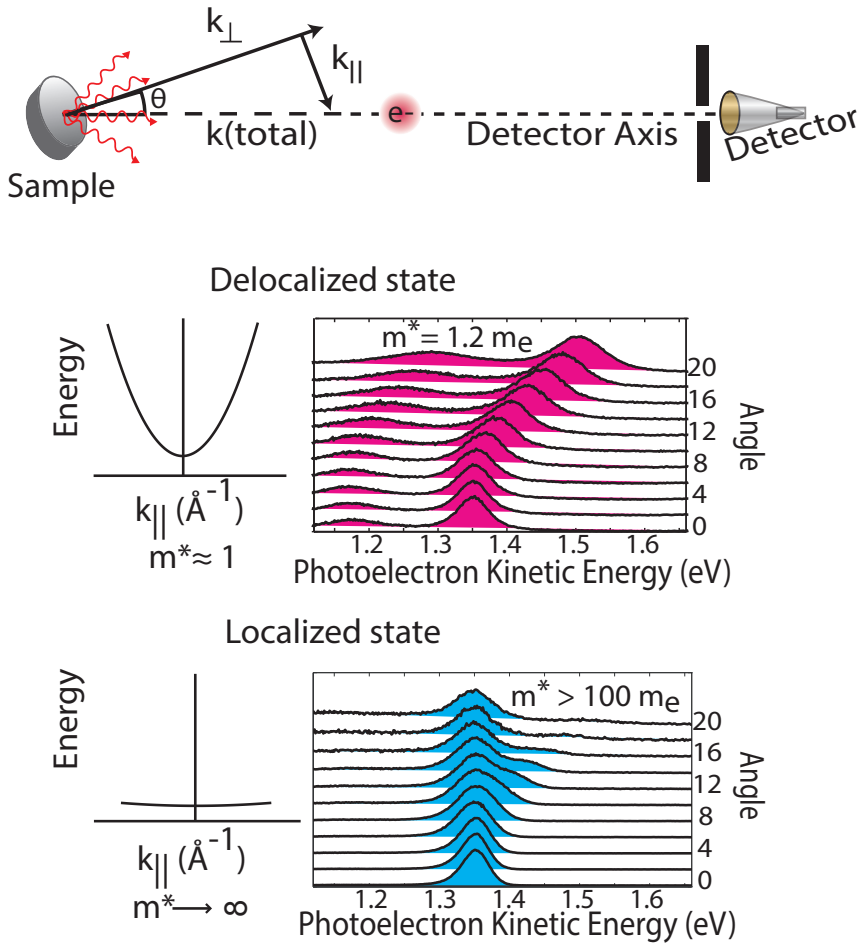

Figure 1.7: Schematic representation of angle-resolved TPPE. The parallel momentum of the electron is related to the angle, θ, between the sample and detector, and only electrons within acceptance range of the slit enter the detector. Experimentally, photoelectron spectra are collected as a function of angle. The angle is converted to the parallel wavevector, $k_{||}$, and a band dispersion plot of E_{kin} versus $k_{||}$ is created to fit the intermediate state's electron's effective mass, m^*. For nearly free electron states (delocalized), the dispersion will show a parabolic relationship and $m^* \approx 1$. Localized states will show a flat band dispersion (energy independent of angle) and $m^* \gg 1$.

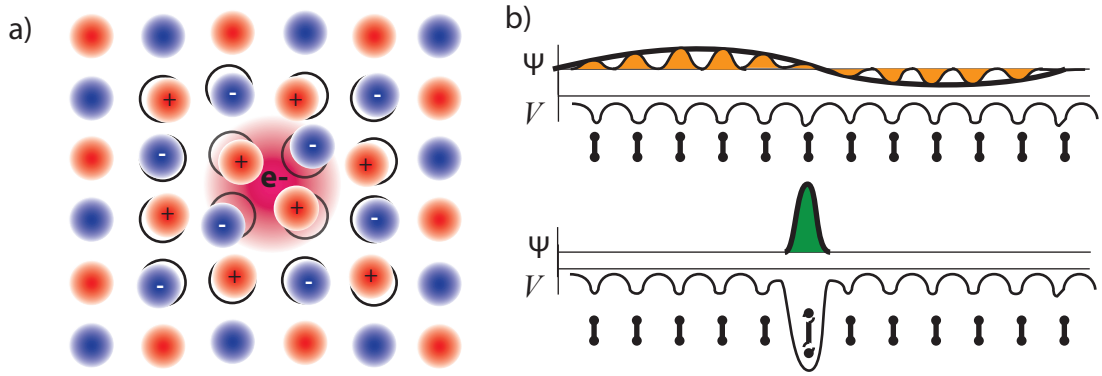

Figure 1.8: (a) An electron in a deformable medium, such as an ionic crystal, can induce a polarization and distortion of lattice ions. The coupling of the electron to the polarization is a quasi-particle termed a polaron. (b) The coupling of an electron to phonon or vibrational can result in self-trapping of the electron and a collapse of the wavefunction to size the size on the order of the unit cell.

Dynamic electron localization arises from an initially delocalized state's wavefunction collapsing and localizing due to the electron's interaction with the surrounding environment. Dynamic electron localization will involve the competition between energies favoring delocalization and those that favor localization. Electron localization in 2D is often referred to as the marginal case, because energies of localization and delocalization are comparable, whereas localization is strongly favored in 1D, and delocalization strongly favored in 3D [43]. Energetically, it remains unfavorable to localize an electron from a delocalized free electron state. Localized states can be thought of as a superposition of all $k_{||}$ states in the free state band, and thus to localize an electron without any change in nuclear coordinate or interaction with its environment requires the formation of a wavepacket of all the Bloch states of the band. The consequence is that the localized state will be higher in energy than the delocalized state, and therefore unfavorable. However, if the localized state is able to interact with its environment to result in an energetically lower state, localization can be become favorable.

Localization from delocalized states can arise from a variety of phenomena. One cause of localization is trapping at pre-existing defect sites in the ultrathin sample. This was observed for electron localization on the femtosecond timescale for crystalline and amorphous ice on noble metal surfaces due to trapping at defect sites. These defect sites were assigned to flucations and disorder in the hydrogen bonding network on the surface [21, 44, 45]. Localization can also arise due to a dynamic response from the material such as solvation or small polaron formation.

A small polaron refers to a quasi-particle composed of an electron in a deformable medium coupled with its self-induced polarization of the lattice atoms (figure 1.8) [46]. When the electron couples to a phonon or vibrational mode of the medium, the resulting small polaron

can have a lower potential energy from the lattice distortion and result in localization on the order of the size of the lattice unit cell (figure 1.8). Small polaron formation by TPPE was first observed for thin films of alkanes on Ag(111), where the delocalized n = 1 IPS electron localized with a self-trapping energy of 10 meV as a result of the electron coupling to vibrational modes of the condensed alkane film [47]. Small polaron formation was also observed for standing films alkyl substituted sexithiophenes, evidenced by a large increase in the electron's effective mass after 200 fs [48].

TPPE studies of electron localization have also observed the dynamic solvation response, i.e. a reorientation of molecular dipoles, causing an energy relaxation and localization of an initially delocalized electron. Solvation-induced localization was observed for acetonitrile/Ag(111) and butyronitrile/Ag(111) interfaces [42]. More recently, the solvation response to a photoinjected electron has been studied in room temperature ionic liquids [49, 50].

It is important note that for all the known studies of electron localization by TPPE, only one discrete localized state is observed. Initially, the electron is excited into a delocalized state, such as an IPS or conduction band, and subsequently the delocalized electron wavefunction collapses to one localized state as a result of its interaction with its environment. The work herein shows a new phenomenon of electron localization and migration through multiple discrete localized trap states.

h

Chapter 2

Experimental

As described previously, angle- and time-resolved two-photon photoemission is an ultrafast pump-probe spectroscopy that measures photoemitted electrons as a function of time, energy, and momentum. Performing TPPE experiments requires a large collection of experimental apparatus and technologies for operation. This collection can be broadly broken down into three sections; (1) an ultrafast laser system providing pump and probe pulses, (2) the ultrahigh vacuum (UHV) chamber for sample preparation and functional conditions, and (3) detection electronics for single electron counting. Much of the apparatus details and upgrades have been described in previous group theses. The original vacuum chamber design and time-of-flight detector details are provide in thesis of W. R. Merry [51]. The detection electronics and data acquisition are described in thesis of J. D. McNeill [52]. Upgrades to sample dosing is described in the thesis of B. W. Caplins [53]. In recent years, the equipment saw an upgrade in the sample dosing chamber, the extension of substrate samples to Ag(100) and Cu(111), and a replacement of a turbo-pump. The following sections will highlight the details of the three major components described above.

2.1 Ultrafast Laser System

532 nm Continuous Wave Pump Laser

The dynamics of excited electrons and electron-transfer events occur on the femtosecond (fs, 10^{-15}s) timescale and therefore require pulses of light with femtosecond or shorter timewidths. Fortunately, this is readily possible with the advent of the Titanium Sapphire laser. General laser operation requires population inversion in a gain medium. This of course cannot be achieved with normal ambient photons, and therefore requires a pump laser generating high-power light from electricity. This is performed by the diode-pumped solid-state Neodymium Vanadate (Nd:YVO_4) Verdi V-18 which outputs 18 Watts (W) of continuous 532 nm light. Briefly, a diode-array pumps the gain media, Nd:YVO_4, outputting 1064 nm light. This light is frequency doubled by second harmonic generation in a Lithium triborate

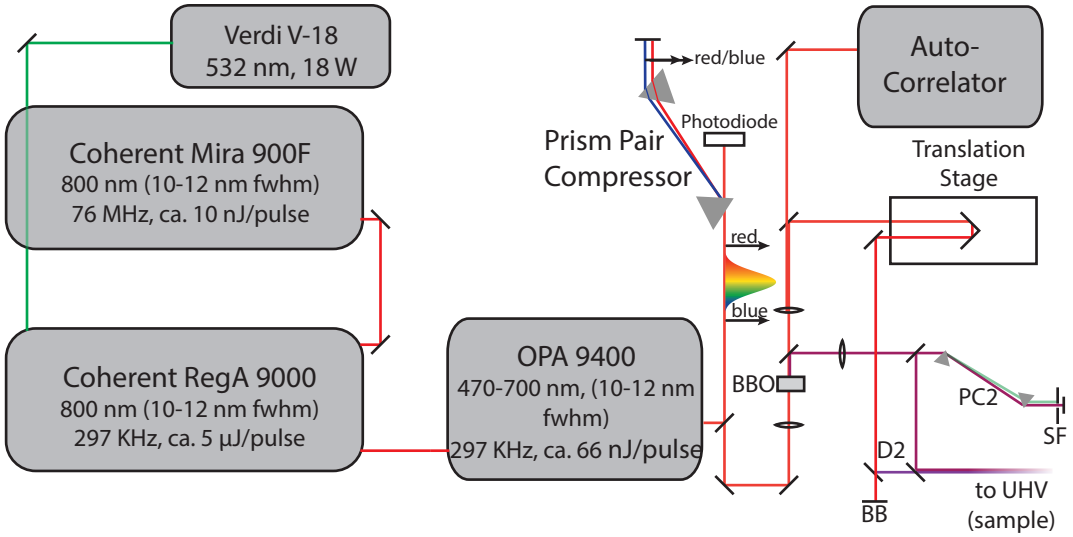

Figure 2.1: Table layout of pump laser, oscillator and regenerative amplifier, optical parameter, and additional optics for pump and pulse generation used for TPPE experiments. Prism pair compressor illustrates group velocity dispersion compensation by causing red leading edge to travel a greater effective path length, allowing the blue tailing edge to catch up to red edge and compress the pulse.

(LBO) crystal to provide the 532 nm output. The operating amperage of the diode-array should be monitored. Typically operation is approximately 49 Amps, and should not exceed $\gg$ 50 amps. One common error found with the Verdi pump laser is the Error Code # 4: Vanadate 2 Temp Fault. This can be fixed by simply turning off the power supply switch on the control box for about 10 seconds and turning back on.

Ti:Sapphire Oscillator

Part of the 18 W 532 nm output is used to pump the Ti:Sapphire gain medium of the Coherent Mira 900 Kerr-lens mode-locked oscillator. The 532 nm is centered at the maximum of the gain medium's adsorption spectrum. The emission from the gain medium is centered at 800 nm, and is placed in a cavity between two high-reflecting end mirrors. As the 800 nm emitted light travels back and forth between the cavity end mirrors, the passing light is amplified in the gain media by stimulated emission. Only light passing directly perpendicular between the cavity end mirrors will be substantially amplified, providing a high directional preference for lasing. Femtosecond pulses are generated by active and passive mode-locking mechanisms. In a laser cavity, only certain resonant longitudinal modes are allowed as standing waves. This is determined by $2d = \mathrm{n}\lambda$, where d is the distance between the cavity end mirrors, n is the longitudinal mode, and λ is the wavelength. Of course, no

laser light is purely monochromatic, and will have some characteristic spread in frequency. Active mode-locking is achieved by random fluctuations in the cavity length with a butterfly reflector starter. The rapid fluctuation in the cavity length creates a large number of cavity modes. The high number of longitudinal standing waves are able to constructively interfere creating an intense, phase-locked pulse. Passive mode-locking is achieved by the Kerr lens effect, where the high intensity of the Gaussian mode-locked pulse alters the refractive index, causing the media to act as a lens due to the distribution in refractive index across the profile beam. This causes a self-focusing of the mode-lock beam, and in conjunction with a manual slit, the 532 nm light is preferentially blocked, and only the 800 nm pulse propagates in the cavity and is amplified. Group velocity dispersion effects are compensated by a prism pair compressor folded into the cavity's arm. The output of the Mira is a 76 MHz train of 800 nm, 200 fs pulses with a 10-12 nm FWHM Gaussian width. The output power is > 1 W, corresponding to ≈ 13 nJ pulses. This pulse energy is insufficient for experimental operation, so the pulses are then sent to an amplifier.

Regenerative Amplifier

The Coherent RegA 9000 Ti:Sapphire regenerative amplifier is used to amplify the 13 nJ pulses from the oscillator to energies in the μJ range. The remaining portion of the 18 W 532 nm pump light is used to pump a Ti:saph gain medium used for pulse energy enhancement in the amplifier. The 76 MHz train of pulses from the oscillator enter the amplifier, and a single pulse is selected by an acousto-optic SiO_2 cavity dumper to be injected into the amplifier laser cavity. The single injected pulse then undergoes 20 to 30 round trips in the cavity and amplified by stimulated emission in the gain medium pumped by the 532 nm light. During the amplification, the pulse also increases in pulse duration to ca. 30 ps. The amplified pulse is then ejected from the cavity by the cavity dumper, and compressed using a holographic diffraction grating. Historically, the amplifier was operated at a 225 kHz repetition rate. However, TPPE detects single electron events, so the repetition rate was increased to 297 kHz to provide more electron events and better statistics. The operating power at 297 kHz was typically 1.2-1.3 W with daily cleaning and tuning, corresponding a pulse energy of 4 μJ. Realignment of the amplifier was performed multiple times to keep power and stability high. Directions are provided in the manual, and additional comments and tips are described in the laser notebook, but it should be noted that it is a non-trivial, multi-day affair. While the output power might typically drop 10-20 %, much of this power can be regained through careful cleaning of the cavity dumper, Ti:saph gain medium, and quick tuning.

Optical Parametric Amplification (OPA)

In order to provide greater experimental flexibility in the pump and probe wavelengths, the 800 nm output of the regenerative amplifier is fed into a Coherent 9400 Optical Parametric Amplifier. The 800 nm pulse is split at a beamsplitter, with about 75% of the energy being frequency doubled into 400 nm light in a BBO crystal. The second harmonic power of the

800 nm RegA pulse in the OPA is used as a tuning parameter for pulse compression in the RegA. Shorter pulses typically give increased SHG power, and 200 mW of SHG should easily be achieved with powers going as high as 230 mW. The remaining 25% of pulse energy is focused into a sapphire crystal to create a broad white light continuum. The 400 nm SHG and broad white light are then focused and recombined into a second BBO crystal. The angle of light mixing with the BBO crystal and the delay between the 400 nm and white light provide a means of creating a tunable visible pulse of 470 nm to 700 nm. Typical output power of the OPA is 30 to 40 mW at 297 kHz, with greater conversion efficiency at redder wavelengths.

The output of the OPA is then sent to the prism pair compressor to compensate group velocity dispersion and compress the visible pulse to $\approx$ 75-120 fs, with redder wavelengths having shorter pulses. The compressed pulse is then focused into a β-BBO crystal (Inrad 250 μm θ=44 MgF_2 coated) to generate an ultraviolet (UV) pulse via second harmonic generation of the visible pulse. The visible and UV pulses are then physically separated by a dichroic mirror. The visible pulse is sent onto a translation stage, which takes 1 μm step sizes, providing 6.66 fs delay step size between visible and UV pulse for time dynamics. The visible and UV pulse are then recollimated and enter the UHV housing the sample and electron detector. A layout of the ultrafast laser system and optics is provided in figure 2.1.

2.2 Ultra High Vacuum

Ultrahigh High Vacuum (UHV) conditions, defined as pressures $< 10^{-7}$ Torr, are needed for successful TPPE experiments. TPPE is inherently a surface sensitive technique due to the short inelastic mean free path of low energy electrons generated in the pump-probe sequence. UHV conditions are needed to achieve a high level control over ultrathin layer growth of samples as well as maintaining surface cleanliness from any gas adsorption contaminants. Assuming a sticking coefficient of 1 (any gas molecule that hits the sample surface will adsorb), the surface would be completely covered and therefore contaminated in 10^{-6} Torr seconds. This implies that if the base pressure is 10^{-6} Torr, the surface will be covered in 1 second, which is clearly insufficient time for successful experiments. To achieve surface cleanliness over a long period of time, pressures $< 10^{-9}$ Torr are needed. UHV conditions are also required to keep the mean free path of the photoemitted electrons greater than the distance traveled to the detector. If the photoemitted electron interacted with any gas molecules traveling to the detector, its resulting energy would be altered, nullifying meaningful electron dynamics occurring at the sample.

UHV condition in the sample chamber is achieved by a set of three pumps. A roughing pump (Edwards RV5 rotary vane pump) is first used to bring the chamber from atmospheric pressure to $\sim$ 200 mTorr. Once this base pressure is achieved, a turbomolecular pump (Edwards EXT 250) can safely operate and achieve a base pressure of 10^{-6} Torr. The Edwards EXT 250 turbo pump failed after 20 years of successful operation, and was replaced with a refurbished Edwards EXT 255H turbo pump modified with a KF10 flange adapter to

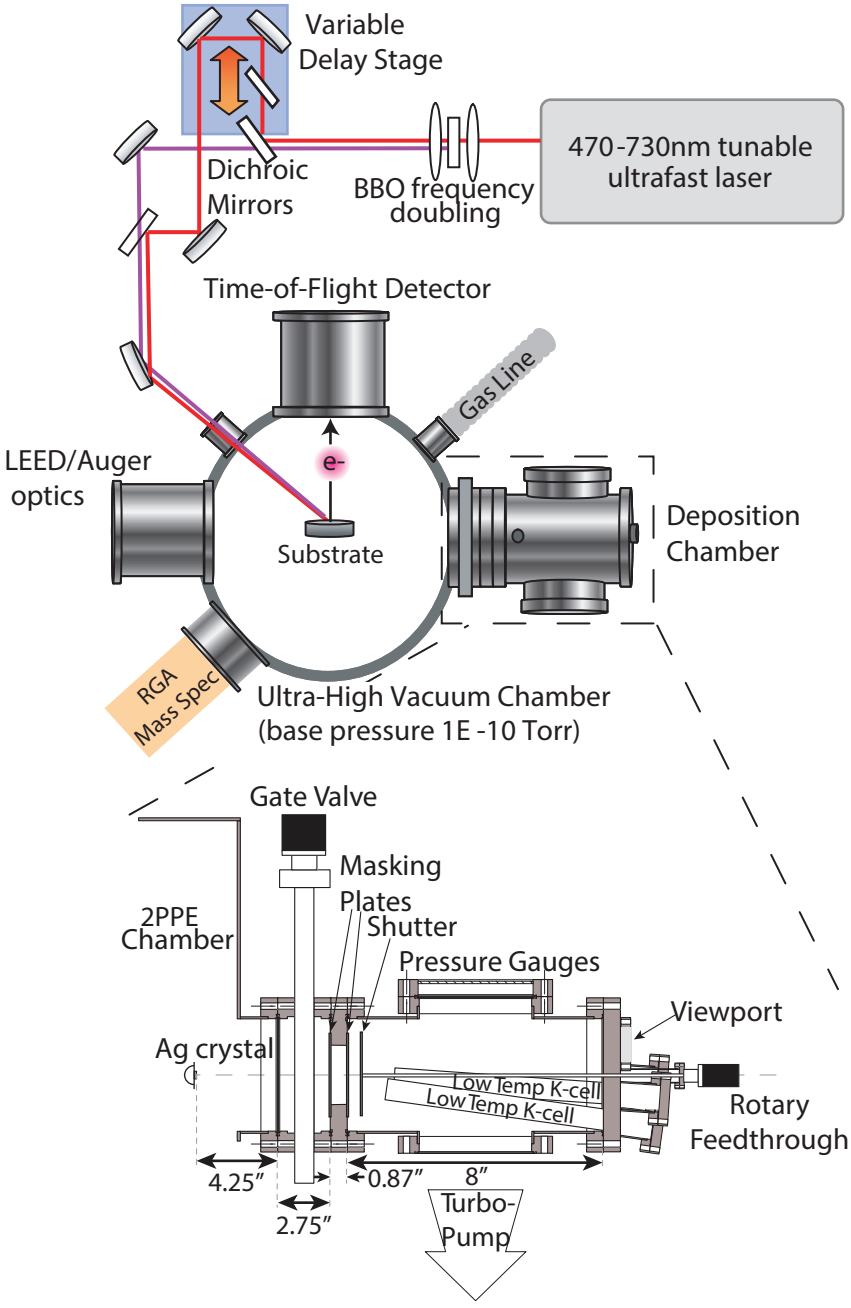

Figure 2.2: Schematic of complete TPPE experimental apparatus, including the laser system and Ultra-High Vacuum chamber. An expanded view of the upgrade side chamber for sample dosing and preparation is provided. Upgraded design was headed by B.W. Caplins.

allow purging with N_2 gas. Upon vacuum chamber exposure to atmosphere, adsorption of water and other gas molecules to the chamber wall prevent base pressures lower than 10^{-6} Torr being achieved in a reasonable time. Sufficient sealing of ports needed for successful UHV can be verified by Helium leak checking with a quadrupole mass spectrometer (SRS RGA-300). To expedite UHV pressure, the chamber is covered in a fiberglass tent, and baked to 100 ^{o}C to desorb water molecules. Note that temperatures much greater than 100 ^{o}C must be avoided to prevent sealing and window failure. Once a base pressure during baking of roughly 3.8 x 10^{-8} Torr is achieved, the bakeout is turned off and the the tent removed. At this point, a base pressure of 1 x 10^{-9} Torr is readily achieved. Lower pressures of 1 x 10^{-10} Torr can be achieved with simultaneous pumping by a Perkin Elmer TNBX ion pump. A full layout of the laser system and UHV chamber is shown in figure 2.2.

Metal Substrate Samples

Single crystal metal samples are used as substrates for two-photon photoemission experiments. Single crystals of 99.9999% purity were purchased from Princeton Scientific Corporation. Crystals of 12.70 mm diameter were cut with an edge angle of 8.5 $\pm$ 1 degree, and face polished with a roughness $<$ 3 microns. Historically, much of the work done in the group was performed on a Ag(111) single crystal substrate. However, it became necessary to perform experiments with Ag(100) and Cu(111) crystals. A simple comparison of the band structure between Ag(100), Ag(111), and Cu(111) is provided in figure 2.3.

Single metal crystal surfaces were cleaned daily by sputtering the surface with Ar^+ and annealing. During a sputter, Argon gas is leaked into the chamber through a leak valve with a pressure $\approx$ 5 x 10^{-6} Torr, ionized, and accelerated by 0.5 keV impacting the single metal substrate at grazing incidence. After the sputter, the crystal is subsequently annealed to remove impurities and reduce surface roughness. Ag(100) was sputtered for 20 min (20 A) at 500 K and annealed to 700 K for 60 min. Ag(111) was sputtered at 500 K for 20 min and annealed at 725 K for 20 min, and Cu(111) was sputtered for 20 min at 500 K and annealed to 725 K for 40 min. Sample cleanliness was determined by the appearance of surface states with narrow Voigt FWHM as well with Auger electron spectroscopy and low energy electron diffraction (LEED). Small spot sizes with correct lattice diffraction pattern are indicators of surface cleanliness. LEED images were acquired with an Omicron SpectaLEED, and images on the phosphor screen were captured with a CCD camera. LEED images of Ag(100), Cu(111), and Ag(111) are shown in figure 2.4. Samples could be restively heated to 725 K, or cooled with liquid N_2 to ca. 120 K, and further cooled with liquid Helium to ca. 60 K by means of a cryostat attached to a copper braid. Due to resistance in heat transfer at interfaces between the cryostat and copper braid, and the copper braid and sample holder, the lowest temperature achieved is 120 K with liquid N_2 rather than its temperature of 77 K.

Single metal crystal substrates were placed on sample holder and manipulator arm providing 5 degrees of freedom. Three degrees of freedom are provided in the orthogonal directions, x, y, and z. Additionally, the sample could be rotated throughout the various ports

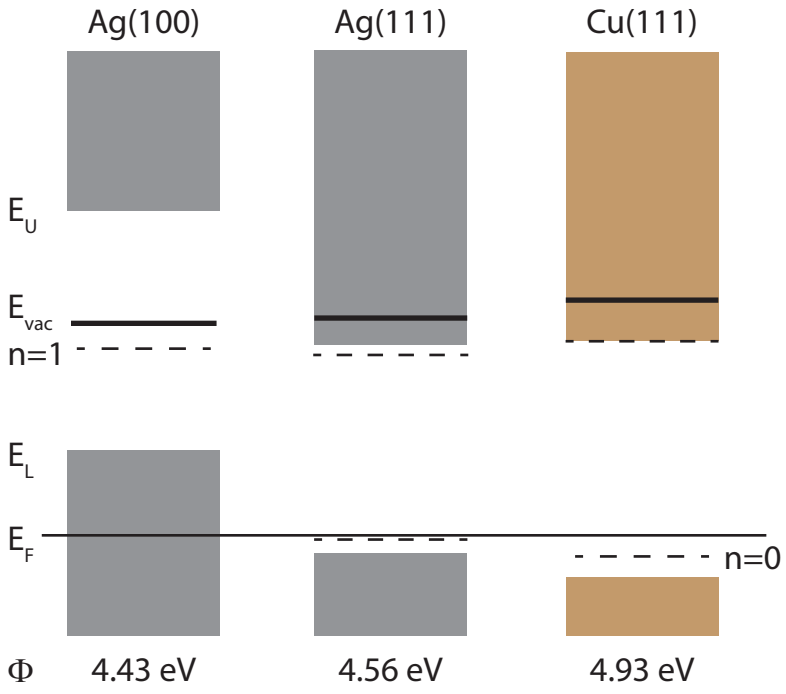

Figure 2.3: Simple band structure comparison between Ag(100), Ag(111), and Cu(111) referenced to the Fermi energy, E_F. The bulk upper valence band edge and lower conduction band edge are denoted as E_L and E_U, respectively. Dotted lines denote the energy location of the n = 1 IPS and dotted lines below E_F denote the location of the Shockley surface state (n = 0). Finally, the vacuum level, E_{vac}, is denoted as thin solid line. A comparison of the workfunctions, $\Phi = E_{vac} - E_F$, is provided below and taken from [35].

in the vacuum chamber for sample deposition, time-of-flight detection, LEED/Auger measurements, sputter/annealing, and temperature-programmed desorption. The final degree of freedom is rotation of the sample with respect to the detector axis provided by a gioniometer for angle-resolved measured. The goniometer allows for rotation of -12^o to 20^o. Samples are intentionally cut at a wedged angle to access higher angles between the sample and detector and therefore higher parallel momentum states.

Ag(100) Characterization

As mentioned, much of the prior TPPE studies in the Harris group were carried out with a Ag(111) substrate. However, the use of Ag(100) offers potential advantages in studying electron dynamics of thin film adsorbates. First, the Shockley surface state of Ag(100) remains experimentally inaccessible (see figure 2.3). The occupied Shockley state dominates photoelectron spectra during the cross correlation of the pump and probe pulse (100 fs) due to its high cross sectional area for photo-excitation, and thus obscures electron dynamics in

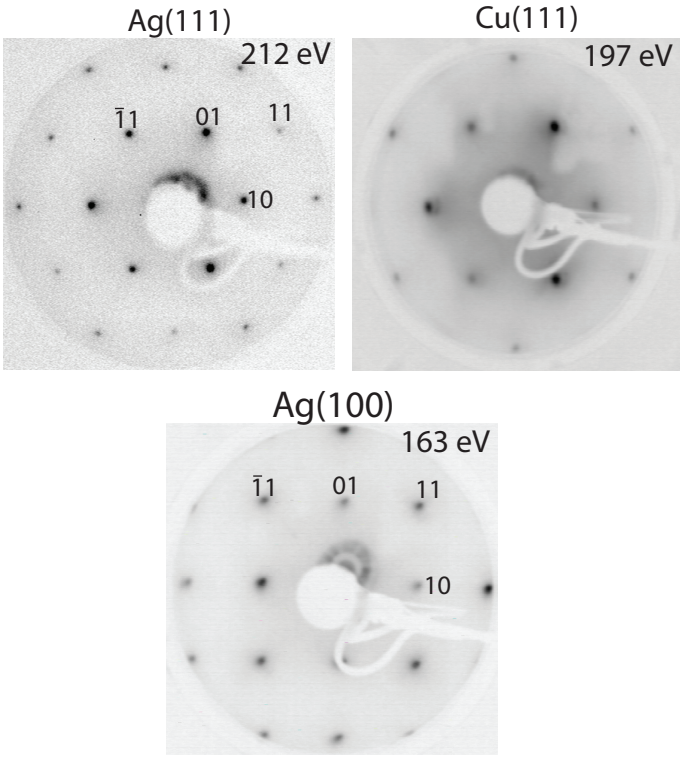

Figure 2.4: Low energy electron diffraction images of reciprocal lattices of Ag(100), Ag(111), and Cu(111). Energies in upper corner of images correspond to energy electron beam used for diffraction image. Small spot size and correct diffraction pattern for fcc(111) and fcc(100) lattices indicate surface cleanliness.

thin films at early time delays. The IPS and E_{vac} lie well within the projected bulk bandgap of Ag(100) versus Ag(111), and thus removes any possibility of adsorbate states coupling with bulk substrate states.

As much of the work in this thesis uses Ag(100), a characterization of the surface states and electron dynamics of pristine Ag(100) are provided. These are summarized in figure 2.5. Other experimental works reporting the excited states and lifetimes of Ag(100) can be found in the following references: [16, 54, 55, 56, 57, 58, 59]. The experimental binding energies for the n = 1, n = 2, and n = 3 IPS of clean Ag(100) observed in this work are 0.55, 0.17, 0.08 eV, respectively. Excellent agreement between the observed BEs and those reported in the above references are found. Additionally, the lifetimes for the n = 1, n = 2, and n = 3 IPS, found in figure 2.5, are 56 ± 10, 181 ± 26, and 443 ± 52 fs, and are also in good agreement with those reported previously. The binding energies and lifetimes in this work support the pristine cleanliness of the Ag(100) used in the experiments herein.

An additional figure of merit to confirm the surface cleanliness is the band dispersion of the clean Ag(100) surface states, which is shown in figure 2.6. The raw angle dependent

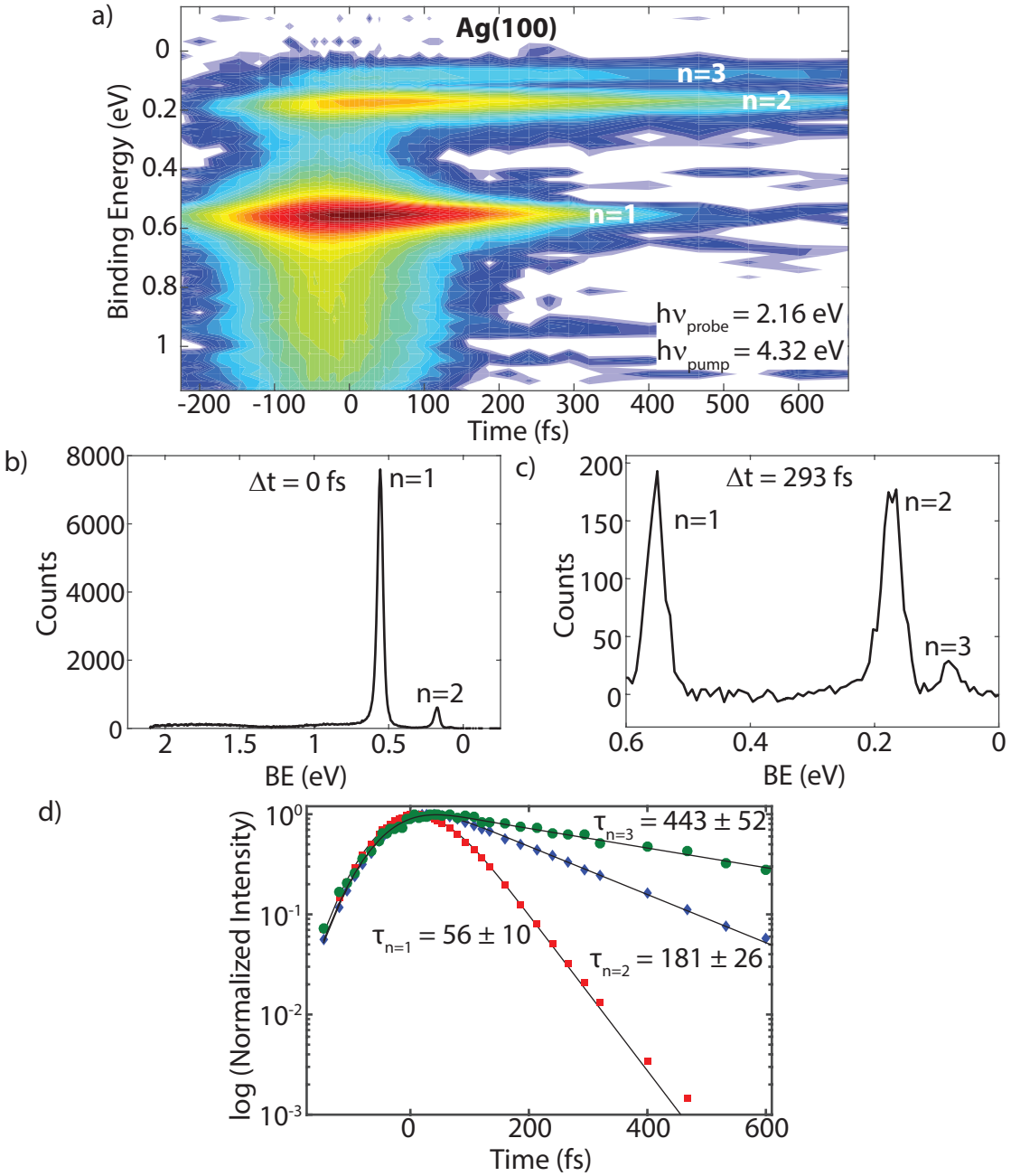

Figure 2.5: (a) Logarithmic false color contour plot of Ag(100), with pump pulse of 287 nm and probe pulse of 574 nm at 300 K and $k_{||} = 0$ Å. (b) Individual time slice of (a) at time delay of 0 fs. Presence of n = 1 and n = 2 IPS of clean Ag(100) clearly visible. (c) Time slice of (a) at 293 fs, showing the presence of the n = 1 and n = 2 as well as the n = 3 IPS. (d) Fitted lifetimes of the n = 1, n = 2, and n = 3 IPS of Ag(100) at 300 K. Time-dependent population is from 50 meV integration window about peak center and fit to an exponential decay convoluted with the instrument response function.

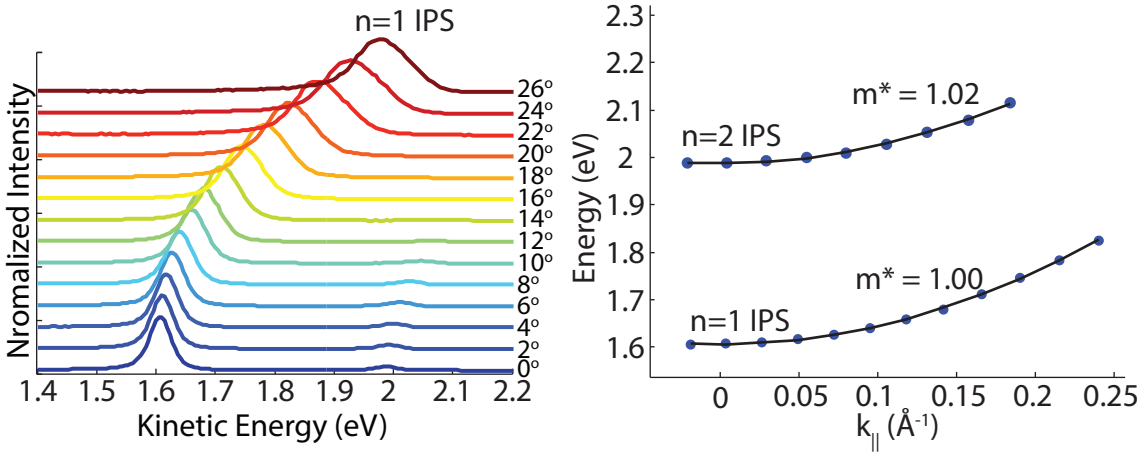

Figure 2.6: Left: Raw angle dependent photoelectron spectra of clean Ag(100). Each slice is an increment of 2^o and intensity normalized to peak maximum. Taken with pump and probe photons of 287 and 574 nm, respectively. Right: Effective mass fits for the n = 1 and n = 2 IPS of Ag(100).

photoelectron spectra is displayed in the top of figure 2.6, revealing a parabolic dependence between the n = 1 and increasing angle. The fitted effective mass of the n = 1 and n = 2 IPS are $m^* = 1m_e$ and $m^* = 1.02m_e$, respectively. These are also in good agreement with other reported values for the effective masses of the IPS on clean Ag(100), and further confirm the long range order and surface cleanliness of Ag(100). In summary, the observed IPS series shows the correct energetic, time-dependence, and free electron character of clean Ag(100). The surface cleanliness of Cu(111) is verified in figure 2.7, which also shows the correct effective masses for the Shockley state and n = 1 IPS.

Sample Dosing and Characterization

Ultrathin layers of organic semiconductors and alkali halide films are achieved by molecular vapor deposition from the side chamber (see figure 2.2). Original attempts to grow thin films of alkali halides, primarily NaCl, were done using a 3 cell evaporator from MDC heated by electron bombardment. The commercial evaporator was manually modified by E. A. Muller being fitted with a customized stainless steel Knudson cell heated restively and controlled by a proportional-integral-derivative controller (PID). The setup is described in the thesis of E. A. Muller [60]. However, it was found that when heating the NaCl under vacuum at temperatures $\geq$ to reported temperatures for vapor deposition, no ultrathin growth was observed, and upon breaking vacuum, the white pure NaCl crystals were light brown in color. The side chamber housing sample deposition was substantially modified and upgraded by B. W. Caplins to allow for multiple material deposition over an independent and wide variable temperature range. See figure 2.2 for a schematic of the upgraded deposition and thesis of

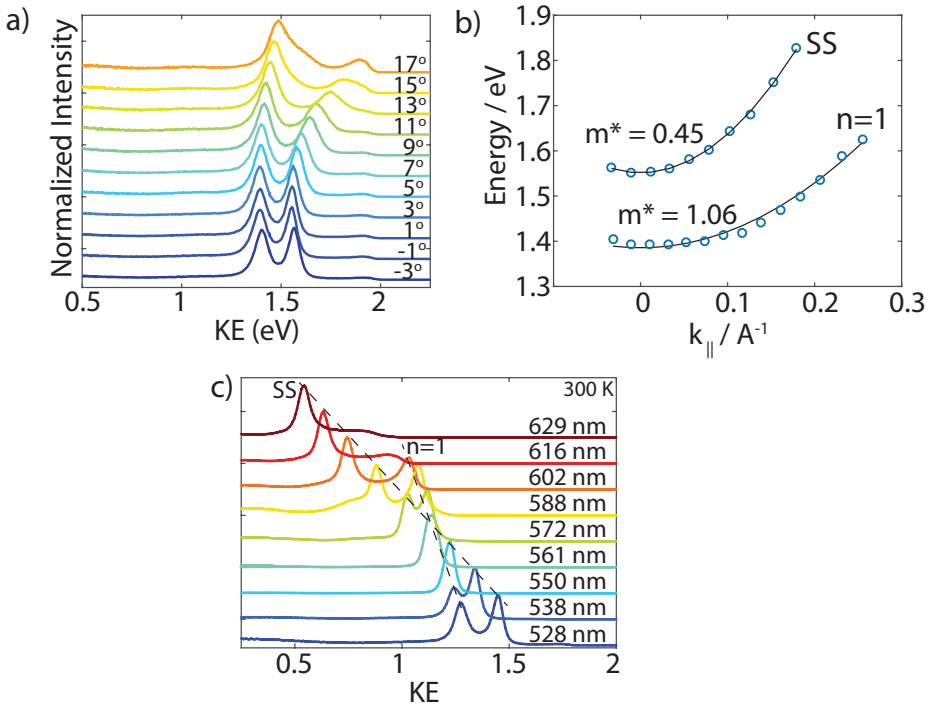

Figure 2.7: a) Raw angle dependent photoelectron spectra of clean Cu(111). Each slice is an increment of 2^o and normalized intensity to peak maximum. Spectra taken with pump and probe photons of 264 and 528 nm, respectively. b) Effective mass fits for the SS (n = 0) and n = 1 of Cu(111). c) Wavelength survey of clean Cu(111). Resonance between the n = 1 and SS observed around 550 nm to 560 nm. Because the SS is initially occupied, peak KE versus wavelength has a slope of 3hν versus 1hν of unoccupied n = 1

Caplins for further details [53].

The upgraded design included two separate commercial, single effusion cells mounted into a single flange. The flange was customized such that the angles of the Knudson cell would point the molecular beam to the center of the single crystal metal substrate. The setup also included a manual shutter. One cell used previously was from Applied EPI (Applied EPI EPI-10-MLT), and the other was newly acquired from MBE-Komponenten. Both Knudson evaporators used high-grade pyrolytic boron nitride cells, and provided substantial improvement in high-quality ultrathin film growth.

Growth of NaCl on noble metal substrates (Ag(100), Ag(111), Cu(111), used in this work) has been described in great detail [61, 62, 63, 64, 65, 66]. NaCl growth on noble metal substrates forms three-dimensional rectangular islands, which tend to nucleate at substrate step edges, with the NaCl islands forming a carpet like growth over the step edges. This is due to the increased interaction with the small dipole at step edge versus terrace sites [62]. As much of the work herein concerns NaCl on Ag(100), its growth mode will be discussed in more detail, and has been carefully detailed in the work of the Cabailh et. al. [61]. It

should be noted that all alkali halides purchased were of highest purity ($\geq 99.999\%$) and that NaCl evaporates as NaCl pair monomers, rather than Na+ and Cl- ions, such that largely defect-free and non-polar islands are formed. During sample deposition, when the substrate is held at temperatures approximately > 340 K, a large NaCl base island 2 ML in height will be formed. The NaCl islands align with their (100) main crystallographic direction either parallel with the Ag(100) direction (0^o) or rotated 45^o with respect to the Ag(100) lattice. As the temperature of the substrate is heated during island growth, the size of NaCl base islands increases, whereas the island density decreases. Upon further deposition, smaller ad-islands of 3 ML and 4 ML in total height form typically in the center of the large 2 ML base islands [61].

The growth of high quality NaCl crystalline islands with long range order can be verified by LEED and are shown in figure 2.8. Of specific interest, NaCl on Ag(100) shows high quality LEED spots, indicating long range order. Additionally, NaCl islands aligned 0^o and 45^o with respect to the Ag(100) lattice are easily identified. LEED images of NaCl on Ag(111) and Cu(111), however, show a diffuse diffraction ring of NaCl, indicating a more random orientation of NaCl island alignment with the metal lattice. The bottom half of figure 2.8 shows equal quantities of NaCl dosed with the Ag(111) substrate held at 335 K (left) and 400 K (right). There is some evidence that holding the Ag substrate at higher temperatures results in higher preferential alignment with one of the three possible lattice orientation, indicated by more pronounced spots for NaCl rather than a diffuse ring.

Growth of NaCl at substrate temperatures well below room temperature result in 1 ML height island formation. Dosing NaCl while holding the Ag substrate at 120 K (versus 400 K for much of this work) results in less intense and broader spot size, implying reduced long range order. Assuming the NaCl is much less mobile while the Ag substrate = 120 K, and that growth follows a more 'hit and stick' model of growth, dosing rate can be calibrated using Auger spectroscopy. This is done by tracking the Cl Auger peak intensity as a function of dosing time, and finding a change in the resulting peak slopes. The first change in slope is defined as a monolayer equivalent (MLE). This is described in more detail in Chapter 3.

2.3 Electron Detection

The electron detector and data acquisition is described in great detail in the theses of W. Merry and J. D. McNeill [51, 52] and will only be described briefly. Time-resolved two-photon photoemission spectra are collected by single electron time-of-flight detection. After the two photon absorption, photoemitted electrons travel a distance of 13.5 cm to the electron detector. The length of flight time, typically on the order of hundreds of nanoseconds, depends on the photoemitted electron's kinetic energy. The flight tube is covered in μ metal shielding to prevent stray electric fields distorting the electron's flight. The electron detector in the system is a microchannel plate detector (Galileo Electro-Optics model FTD-2003) with a pair of microchannel plates (MCP, Photonis MCP 25/12/10/12 D 40:1 @ 900V MGF2, MS) in a chevron configuration to act as an electron multiplier. Electron detection

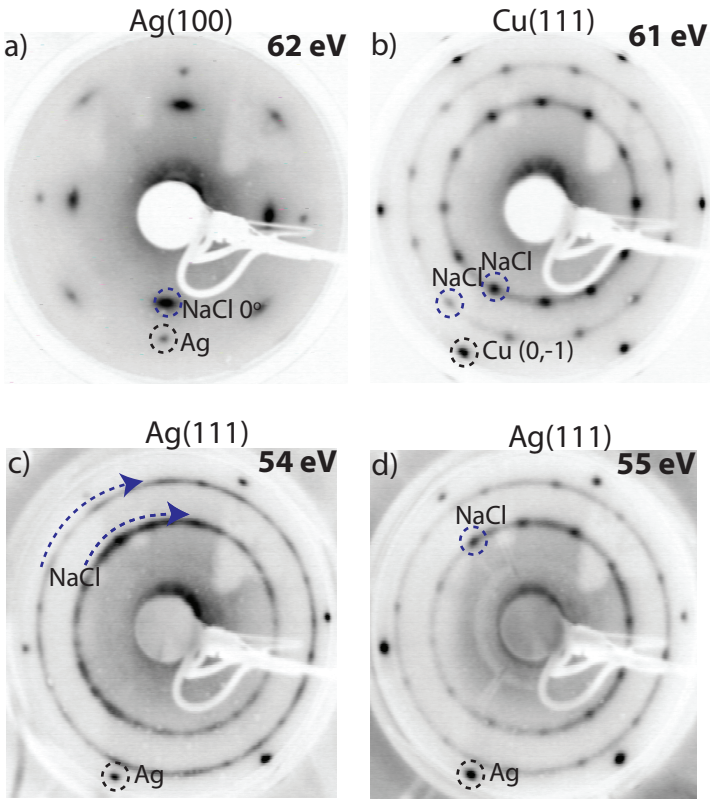

Figure 2.8: LEED images of ultrathin layers of NaCl on Ag(100), Cu(111), and Ag(111). Energies of electron beam used to take image are indicated in the top right corner, and identification of substrate above image. a) On Ag(100): 9 min of NaCl, dosed at 820 K, Ag = 400 K, Image = 175 K. b) On Cu(111): 39 min of NaCl, dosed at 790 K, Cu = 335 K, Image = 125 K. c) On Ag(111): (Left) 21 min of NaCl, dosed at 775 K, Ag = 335 K, Image = 130 K. On Ag(111): (d) 21 min of NaCl, dosed at 775 K, Ag = 400 K, Image = 130 K.

works as follows: photoemitted electrons are accelerated by a bias to the first MCP plate. The MCP acts as an electron multiplier. When the photoemitted electron impinges upon the plate, secondary electrons are emitted, creating a cascade effect. A very large bias is applied between the two MCP plates, resulting in amplification of the electron signal to detectable levels. Finally the amplified electron signal is accelerated towards a 50 Ω impedance detector anode attached to a BNC feed through cable. The amplified signal is connected to a preamp (Phillips 6954 10x) for further amplification and then sent to a Constant Fraction Discriminator (CFD) (Tennelec TC455). The CFD serves to shape the amplified electron signal providing a reliable timing pulse which is then sent to a Delay box (Ortec 425 A) and then finally to a Time-to-Amplitude (TAC) converter. The amplified photoemitted electron signal serves as the stop pulse for time-of-flight detection.

A start timing pulse is provided by a fast photodiode (Thorlabs DET110A). A portion

of the laser pulse before entering the UHV chamber is directed to the photodiode, creating a signal ($\approx$ 1 V) which is sent to CFD for a reliable start timing pulse. The start timing signal is then additionally sent to the TAC unit (Ortec 566). The TAC generates a pulse by a capacitor which is charged during the duration of the start (photodiode) and stop (MCP) pulses. Thus, the voltage generated by the TAC pulse is directly proportional to the time-of-flight of the photoemitted electron. The TAC pulse is then sent to a Multichannel Analyzer (Ortec 927) which counts and stores the signals by sending the specified voltage output to its specific "bin". In this way, a histogram of photoemitted electrons with a specified flight time is built up during the course of spectra collection. After the scan, the multichannel analyzer sends the histogram to a computer, which analyzes the data and converts flight times to kinetic energy. Count rates during electron detection are typically kept $\leq$ 20 kcps (kilocounts per second). Noting that the repetition rate of the laser is 300 kHz, this ensures that less than 1 electron is photoemitted per laser pulse in order to prevent space charge broadening produced by multiple photoemitted electrons interacting and distortion of flight time. Finally, in recent years, electron lifetimes $\gg$ fs have been observed for ionic liquids and ionic crystalline solids which requires scans that track the ultrafast fs dynamics to hundreds of ps in time delay. This results in long scan times (10 - 20 min), which often is longer than the stability of laser pulse power. Care should be taken to compromise scan collection time, number of delay steps, and choice of delay steps for data collection. This issue can be further mitigated by taking scans in the forward and backward direction and averaging the scans.

The detection electronics are calibrated by using known binding energy values of the n = 1 IPS of the corresponding metal substrate. A time zero pulse which serves as reference for determining flight times is determined by the scattered UV light pulse, which typically requires using UV pulses $\leq$ 290 nm. The time for scattered light to traverse the flight tube is instantaneous relative to photoemitted electrons with kinetic energies ranging from 0.1 to 5 eV. Next, the energy separation between the n = 1 IPS peaks probed by the visible and UV pulse are collected at a series of applied biases between the sample and detector. This establishes the calibration for correct flight time and the corresponding multiplicative factor and bias needed for high accuracy photoelectron collection.

Upon formation of an adsorbate, the workfunction of the sample changes, and consequently a corresponding potential bias exists between the sample and detector distorting electron flight times. To establish the applied bias needed for non-zero potential across the flight tube, the new sample workfunction must be determined. This is determined in one of two ways. The first is done by determining the threshold of one photon photoemission (1PPE) by systematically changing the UV pulse to shorter and shorter wavelengths. Once 1PPE is reached, the count rate changes from $\approx$ 20 kcps to the order of the laser rep rate, depending on power. The other method, which is less accurate, is to take an accelerated spectrum, and noting the location of the high energy cutoff (HEC) and the low energy cutoff (LEC). The HEC corresponds to electrons photomitted from the Fermi level by the UV and visible pulse, and the LEC corresponds to electrons photoemitted just above the threshold of the vacuum level. Noting the workfunction, Φ, is equal to E_{vac} - E_F, the workfunction from an accelerated spectra is $\Phi = 3h\nu$ - HEC + LEC. The new applied grid bias (GB) needed

for zero electron acceleration is then $GB_{cleanmetal} + \Delta\Phi\backslash(eV/V)$. The eV/V is determined from a grid bias and accounts for the non 1:1 change between eV shift versus bias (V) shift.

Chapter 3

Femtosecond Trapping of Free Electrons in Ultrathin Films of NaCl on Ag(100)

3.1 Abstract

We report the excited state electron dynamics for ultrathin films of NaCl on Ag(100). The first three image potential states (IPS) were initially observed following excitation. The electrons in the spatially delocalized n=1 IPS decayed on the ultrafast time scale into multiple spatially localized states lower in energy. The localized electronic states are proposed to correspond to electrons trapped at defects in the NaCl islands. Coverage and temperature dependence of the localized states support the assignment to surface trap states existing at the NaCl/vacuum interface. These results highlight the importance of electron trapping in ultrathin insulating layers.

3.2 Introduction

Ultrathin insulating films on conductive substrates are being widely studied for their potential role in numerous applications such as molecular electronics [67], catalysis for water splitting [68], organic photovoltaics (OPV), and organic light emitting diodes (OLED) [69]. An attractive property of alkali halides is their ability to decouple molecular properties from bulk metal in ultrathin film thicknesses. Absorbing species directly onto ultrathin films of NaCl rather than onto a metal has allowed scanning probe measurements of metastable Au atom anionic states [70], and imaging of molecular wavefunctions of organic semiconductors [71, 72]. These systems have been primarily studied by scanning probe measurements which cannot track ultrafast electronic processes in real time, and there remain to date, few time-resolved spectroscopic studies of these systems leaving many unanswered questions about the electron dynamics. Given their importance in molecular electronics and catalysis, understanding the dynamical behavior of electrons in ultrathin insulating systems is of both fundamental and technological importance.

Previous spectroscopic studies examined ultrathin NaCl films on Cu(111) [73]. An electron excited into the conduction band was observed to form a small polaron, evidenced by a dynamic and continuous increase in the electron's effective mass, i.e. moving from a delocalized state to a localized state and a corresponding energy relaxation. The case of small polaron formation was first evidenced in ultrathin layers of alkanes on Ag(111), where the free electron coupled to surface vibrational modes [47]. Our results reveal a fundamentally different mechanism for the localization of free electrons in ultrathin alkali halide films in which the free electron decays to a series of neutral localized trap states, and are of general interest wherever these materials are being employed in the fields of catalysis and devices. These measurements also represent the first experimental observation of an image potential state series of a highly ionic crystalline material.

In this study, we use angle- and time-resolved two photon photoemission (AR-TPPE) to study the excited electronic states and dynamics of ultrathin films of NaCl on Ag(100), a model system for metal/insulator properties. AR-TPPE is a pump-probe technique that measures electron dynamics at metal and metal/absorbate interfaces. Briefly, a pump pulse excites an electron from below the Fermi level to an intermediate state. After a variable time delay, the probe pulse photoemits the electron, and the electron's kinetic energy is measured [Fig. 1(a)].

Experimental Methods: Details of the experimental apparatus can be found elsewhere [43]. The pulses are created with an ultrafast commercial laser system outputting a visible tunable wavelength centered around 1.89 eV, which was then frequency doubled (3.79 eV) to provide the probe and pump pulses, respectively. Electrons are detected via time-of-flight with a typical energy resolution of ∼20 meV. The laser cross correlation is governed by ∼100 fs FWHM. The Ag(100) substrate was kept in an ultra-high vacuum (UHV) chamber and the surface was cleaned before each experiment with standard Ar^+ sputtering/annealing techniques. Surface cleanliness and order were verified with low energy electron diffraction, Auger spectroscopy, and TPPE.

High purity anhydrous NaCl was degassed and dosed from a commercial Knudsen cell at a rate of approximately 0.3 MLE / min onto Ag(100). Dosing rate was approximated from Auger spectroscopy (see Fig. S1). Growth of NaCl on Ag(100) has been well characterized [61, 62, 74, 64, 65]. NaCl islands nucleate at Ag steps and islands form carpet growth over the steps. All samples prepared herein are of NaCl grown at a substrate temperature of 400 K to form large 2 ML base height islands with sides >100 nm [61]. The workfunction, as determined from the onset of one photon photoemission for 1.67 MLE, was measured to be 3.85 ± 0.06 eV ($\Delta\Phi$ = -0.58 eV), and found to be constant after the first MLE. A bias potential was applied to match the vacuum level of the detector to the vacuum level of the sample to give a field free region to the detector.

3.3 Results

TPPE spectra of 2 monolayer equivalent (MLE) of NaCl reveal three electronic states after initial excitation, as seen in Figure 3.1(b) and (c). The binding energies (BE) of these states with respect to E_{vac}, located at 3.85 eV above the Fermi level, are 0.90 ± 0.03, 0.38 ± 0.02, and 0.20 ± 0.02 eV, respectively. These numbers reflect that over many measurements, but it should be noted the absolute error is dominated by the 0.06 eV uncertainty in the workfunction. We assign these three states to the n=1, n=2 and n=3 image potential states (IPS) based on their energetic location and Rydberg like progression. IPS reside in the vacuum and arise from the induced attractive polarization of free charges in the substrate. The IPS series was theoretically calculated to exist for NaCl/Cu(111) and was predicted to have mixing with the conduction band of NaCl [75]. These states were also observed as field emission resonances on ultrathin NaCl/Ag(100) [65]. The three observed IPS showed poor quality of fit to the accepted quantum defect formula,

$$E_n = V_0 - 0.85\,eV/(n+a)^2$$

where V_0 is the vacuum level, n is the principle quantum number (n=1,2,3..) and a is the quantum defect parameter. The deviation from a pure hydrogenic Rydberg progression is likely due to the IPS coupling to the conduction band and having mixed character, which was theoretically predicted in reference [75] and also calculated for LiF on Li(110) where the IPS coupled to bulk resonances [76].

The n=2 and n=3 IPS' remain constant in energy over time, but the n=1 undergoes a significant shift in energy to the state labeled B in Fig. 3.1(b). The final energy of state B, taken at 500 fs, corresponds to an energy decrease from the n=1 at t = 0 fs of 280 ± 20 meV. The intensities of the states integrated over the small energy windows shown in Fig. 3.1(c) are plotted as a function of time in Fig. 3.1(d). Single exponential fits convoluted with the measured instrument response function were employed for the n=3 and n=1, but were insufficient to model the complete population dynamics of the n=2 and state B. Instead, states B and n=2 were fitted with a truncated single exponential as shown in Fig. 3.1(d).

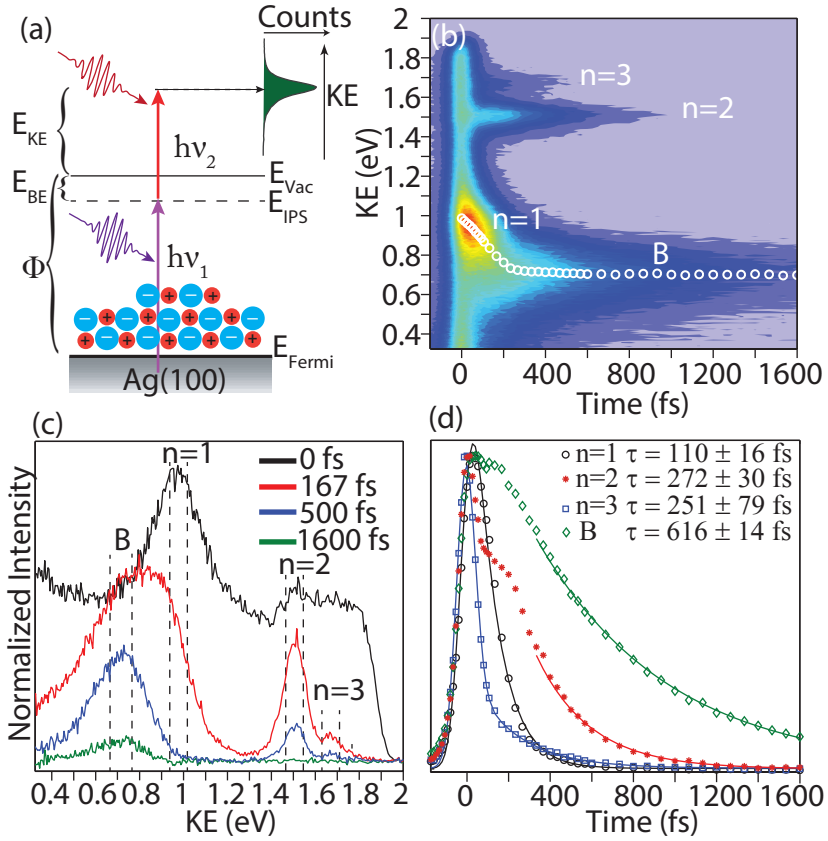

Figure 3.1: (a) TPPE schematic of 2-3 ML NaCl/Ag(100). Pump pulse, hν_1, excites an electron to an unoccupied IPS. After a variable delay, the probe pulse, hν_2, photoemits the electron, whose kinetic energy is measured. (b) False color contour plot of 2 MLE taken at 125 K. White circles guided the eye to the Voigt fit peak center of the n=1 state. (c) Time slices of (b) at specified time delays. Dotted lines provide windows of integration. (d) Normalized cross correlations of (c) with exponential fits.

The interfacial band structure can be measured by varying the angle of the sample with respect to the detector. The parallel momentum of the electron is given by,

$$k_{||} = \left(2m_e E_{kin}/\hbar^2\right)^{1/2} \sin(\theta)$$

where m_e is the electron's mass, E_{kin} is the measured kinetic energy, and θ is the angle of the sample with respect to the detector. Fitting to the parabolic dispersion relation, $E = E_0 + \hbar^2 k_{||}/2m^*$ yields the electron's effective mass, m^*. The measured effective mass reveals the spatial extent of the electron, with a free electron ($m^* \approx 1m_e$) being spatially delocalized, and a heavy effective mass ($m^* >> 1m_e$) corresponding to a spatially localized state. Thus, the dynamical lateral spatial behavior of the electron can be tracked. Figure 3.2(a-c) shows the time dependent band structure measurements. At t = 0 fs, the n=1 IPS

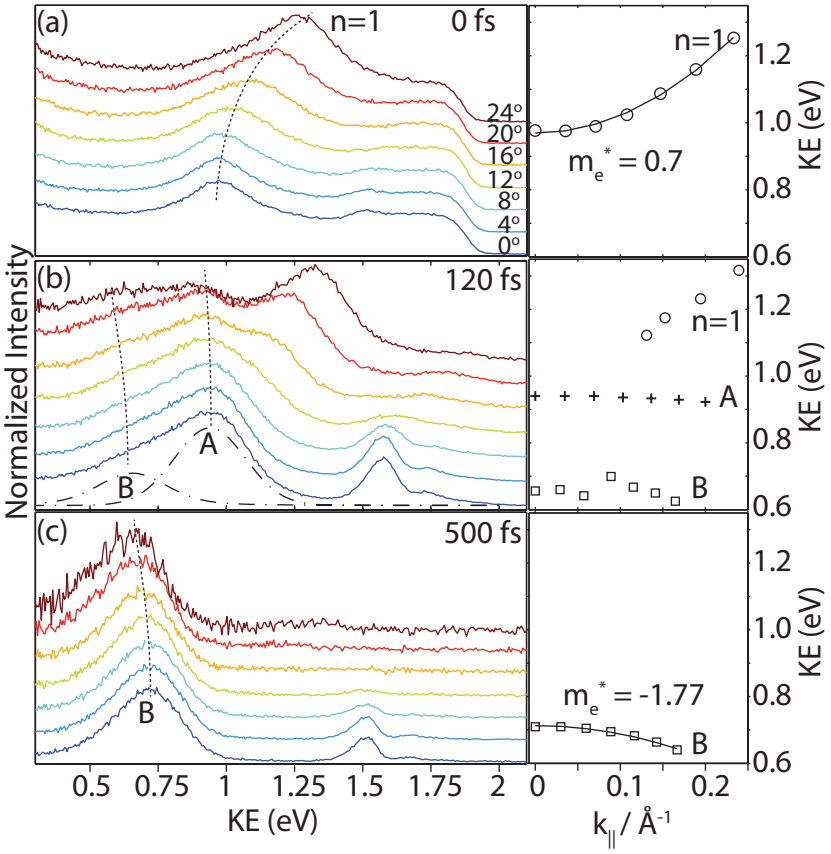

Figure 3.2: (a) Angle resolved measurements of 2 MLE NaCl taken at 125 K and times delays of (a) 0 fs, (b) 120 fs, and (c) 500 fs time delays and corresponding effective masses. Spectra are normalized to max peak height and shifted for viewing. Dotted lines serve to guide the eye to states of interest.

has an effective mass of $m^* = 0.70 \pm 0.11\ m_e$ indicating a spatially delocalized state. The predicted effective mass is $m^* = 1m_e$ on NaCl/Cu(111), the value typically measured for IPS. As mentioned, the n=1 IPS was predicted to have some mixing with the conduction band of NaCl [75], whose theoretically calculated effective mass of the bulk conduction band was $0.6m_e$ [77], and thus we believe this coupling effect accounts for our measured effective mass. A lighter effective mass than $1m_e$ was also observed for 1-4 ML of Xe on Ag(111) where the measured m^* of the n=1 decreased from $0.95m_e$ for 1 ML to $0.6m_e$ at 4 ML, whose value is closer to the Xe conduction band effective mass of $0.35m_e$ [78]. After 120 fs, the n=1 appears to decay into two discrete states labeled A and B, which are localized (energy independent of angle). After 500 fs, the delocalized n=1 and the localized state A have decayed and state B is clearly observed to be localized with an effective mass of $m^* =$ -1.77 $\pm$ 0.71 m_e. The phenomenon of an 'apparently negative dispersion' has been discussed in detail for the case of amphorous D_2O/Cu(111) [79] and is indicative of a localized state.

We emphasize the dispersion measurements taken at intermediate time delay of 120 fs [Fig. 3.2(b)]. At this time delay, both delocalized and localized states exist simultaneously, in contrast to the continuous localization observed on Cu(111) [73]. Furthermore, at higher angles, the presence of multiple localized states, labeled A and B, are observed, and can be seen by the presence of two flat bands in Fig. 3.2(b) and Fig. 3.7. The mechanism of localization in the present system is fundamentally different and unexpected from that known previously observed [73]. For NaCl on Ag(100), localization and decrease in energy are due to population transfer between distinct states. The localized state B is thus differentiated from previous studies and is the focus for the remainder of this work.

Unlike thin films of NaCl on Cu(111) [73], our studies show strong dependence of the localized state dynamics versus coverage [Fig. 3.3(a)]. Increasing coverage reveals that state B's lifetime shows exponential dependence on film thickness, which can be described by

$$\tau(d) \propto \exp(\beta \cdot d)$$

where τ is the electron lifetime, d is the distance from the metal surface, and β is the inverse range parameter and reflects the magnitude of the tunneling barrier [80]. Assuming the crude approximation that each MLE represents an average height increase of 0.282 nm, the distance between NaCl planes, yields $\beta = 3.4 \pm 0.8[2\sigma]$ nm^{-1}. An exponential increase in lifetime with increasing insulator layer thickness was also observed for an electron residing at the sample/vacuum interface of NH_3/Cu(111) [81]. The observed exponential dependence of lifetime with film thickness due to an increased tunneling barrier is consistent with the localized state residing at the NaCl surface/vacuum interface. Further experimental evidence for the state B residing at the surface/vacuum interface comes from the absorption of 1 ML of nonane on the NaCl/Ag(100) sample which quenched stated B (see Fig. 3.7).

The dynamics and energetics of state B also reveal strong temperature dependence. The decay time of the localized state B as a function of temperature is shown in Fig. 3.3(b) and shows that as the temperature decreases from 350 K to 125 K, the lifetime of state B increases. The lifetimes over this temperature range show Arrhenius like behavior, which is consistent with electron transfer (ET) to metal via thermally activated tunneling. The temperature dependent decay lifetime suggests the case of the weak coupling limit of ET, and is in contrast to the temperature independent ET observed for amorphous ice on metal substrates [45]. The localization energy, defined as the difference between the delocalized n=1 at t = 0 fs and the localized state B's energy at t = 500 fs, also shows strong temperature dependence. From 125 K to 350 K, a linear increase in this energy difference versus temperature is observed of 1.0 meV/K.

To determine if the existence of state B was a system specific phenomenon or a general feature we carried out preliminary measurements for other alkali halide/metal systems, including KCl/Ag(100) and NaF/Ag(100) (see Fig. 3.8 and 3.9). These systems show a delocalized n=1 state decaying into a localized state several hundred meV more bound, which is qualitatively consistent with NaCl. The band gaps of NaCl and KCl are similar, 8.5 and 8.4 eV, respectively, however, the band gap of NaF is 11.6 eV [82]. If mid-gap alignment is

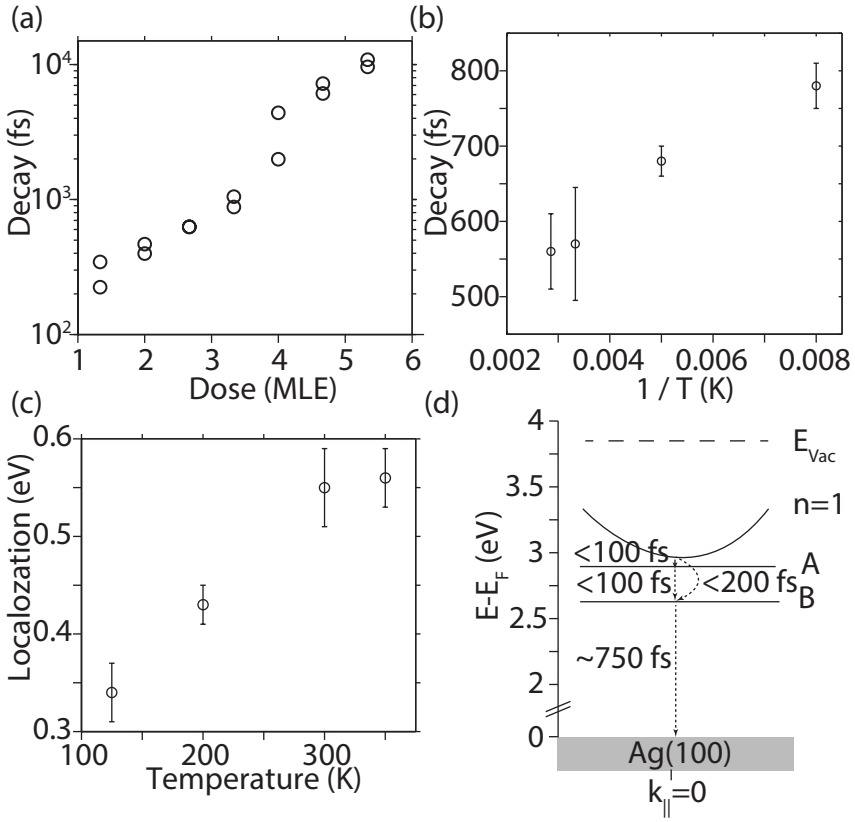

Figure 3.3: (a) Plot of localized state B lifetimes as a function of (a) coverage and (b) temperature. For (a) dynamics were recorded at Ag = 200 K, whereas (b) represents 3 MLE of NaCl grown at Ag = 400 K but measured at various substrate temperatures. Fits are only to the exponentially decaying portion of the population as discussed. (c) Localization energy of 3 MLE, defined as Voigt fits of the delocalized n=1 at t=0 fs minus the localized state B at 500 fs.(d) Band structure diagram summarizing electron decay for an initially free electron in 3 MLE of NaCl at ∼125 K.

assumed, then the conduction band of NaF would exist well above the vacuum level, and thus we attribute the initial delocalized state to be dominantly n=1 in character. Near mid-gap alignment was found for thin films of KCl and NaCl on Ge(100) [83], and weaker interfaction was found for NaCl on Ag substrates versus Cu substrates [64], supporting the mid-gap alignment assumption.

3.4 Discussion

We now discuss the nature of electron localization for NaCl on Ag(100). Our results show that a free electron at the NaCl/Ag(100) interface decays into two discrete localized states

labeled A and B. Initially a free electron localizes to state A in <100 fs, which is stabilized on the order of 75 meV relative to the delocalized n=1 state. Because of this small localization energy and a lifetime comparable to the n=1, we believe it largely retains the probability distribution of the n=1 perpendicular to the surface. The localization of free electrons in two dimensions is known as the marginal case, because the localization and delocalization terms have equal dimensional scaling. Thus, localization is easily assisted by disorder/inhomogeneity in the potential as is present in the current system [41, 84].

At later times (∼200 fs), state B dominates the spectra. Due the complex dynamics at early times, we cannot resolve whether state B is populated through state A or whether state B is directly populated from the delocalized n=1 state. The likely source of a tightly bound trapped state in NaCl films would be bulk-like F-centers. We rule these out because forming these defects in pristine films is difficult [85]. The electrons are observed to undergo trapping with a high probability, and thus a large number of trap defects must exist, further ruling out trapping at F-centers. Additionally, no changes were observed in the spectra over the course of laser experiments. Thus, State B is assigned to an electron trapped at low coordinated neutral defects such as step edges, terraces, corners, kinks in the islands, and NaCl pair vacancies. All these sites exist on the surface/vacuum interface, where state B was experimentally shown to reside, in contrast to the small polaron that resided inside the NaCl film [73]. Trapping of electrons at neutral defects rather than anion vacancies further supports the accepted site of electron trap states at MgO surfaces which were concluded to occur at low coordinated sites rather than F-centers [86]. The magnitude of electron trapping energy we observe is in reasonable agreement with theoretical calculations for electron trap states at grain boundaries of NaCl, MgO, and LiF, which found a trap state inside a dislocation core 0.3 eV below the NaCl conduction band [87]. While we propose the trap states in our study exist at low coordinated atoms, and LEED studies show islands with preferential alignment either 0° or 45° to the Ag(100) steps ruling out a large presence of grain boundaries, it is noted, however, the calculated grain boundaries have similar properties to their surfaces. The decay processes are summarized in Fig. 3.3(d), which depict the relevant energy levels and and an upper bound of the times scales of decay for the initially free electron.

State B was found to fit well to a single Gaussian with a FWHM of 0.3 eV at 125 K, and showed a constant lineshape for times ≥ 500 fs. The broad lineshape can be partially explained by strong electron phonon coupling as seen in scanning tunneling spectroscopy and photoelectron spectroscopy studies [88, 89]. The localized state of Cl vacancies in bilayer NaCl films were measured to have a Gaussian linewidth of 0.32 V, and this unexpected broad and Gaussian lineshape was explained by the electron coupling to the bulk longitudinal optical phonons with energies $\hbar\omega = 32$ meV [90]. At higher temperatures the increase ion mean-square displacement and deformability [91] is better able to stabilize the trapped electron, resulting in the increased trapping energy with temperature we observed.

Theoretical calculations of the excited states of the NaCl/Cu(111) surface found a n=1 IPS and a n=2 and n=3 IPS with mixed IPS and conduction band character [75]. The authors note the results of their calculated n=2 and n=3 IPS show similar behavior to

the states assigned to the surface conduction band conduction band [73], and also point out that no surface conduction band was found in their calculations. Our work further supports the assignment of the conduction band and surface conduction band as the n=2 and n=3 IPS, although a more detailed study to confirm this is underway. As mentioned, our results of electron localization for NaCl/Ag(100) show different behavior than observed for the small polaron formed in NaCl/Cu(111) [73]. We observed localization through multiple discrete states rather than a continuous process, and observed the presence of delocalized and localized states existing simultaneously, further evidence against small polaron formation in the present system, but we cannot definitively rule out the possibility of a surface bound small polaron. The drastically different behavior of electrons at the NaCl/Cu(111) versus the NaCl/Ag(100) interface demonstrates the apparent complexity of the forces that drive localization at surfaces and highlights the need for future experiments and theory to seek insight into the dynamic processes of these systems.

3.5 Conclusions

In conclusion, we used AR-TPPE to observed the dynamics of excited electrons in ultrathin films of NaCl on Ag(100). The first three image potential states were observed directly following excitation. These laterally free electrons decayed with a high probability to defect states proposed to exist at step edges of NaCl islands. Experiments on NaF and KCl demonstrate these trap states are a general feature of alkali halides, and we believe these types of processes likely extend to the technologically important metal oxides insulating surfaces. Given the numerous applications of thin insulating films in technological devices, we believe these trap states could potentially have an impact on electron transport.

3.6 Supplemental Information

Dosing Calibration and Film Characterization

Dosing calibration was measured by slope changes in Auger electron spectroscopy of the Cl peak-to-peak height intensity (Fig. 3.4). The Ag substrate was held at 125 K in order to minimize NaCl diffusion and induce growth of 1 ML height islands rather than 2 ML height. These conditions lead to a more uniform coverage of NaCl on the Ag silver surface in order to determine dosing rate. Figure S4 shows a change in slope in Cl Auger intensity at approximately 3 $\pm$ 0.5 min leading to a dosing rate of $\sim$0.3 MLE / min (monolayer equivalent). Using this definition of a MLE, we find that the n = 1 of Ag(100) becomes nearly extinguished around 6 7 MLE, in good agreement with [61] that reported under their definition of 6 MLE, 98% of the silver surface was covered by NaCl films. This is further supported by calculating the adsorbate thickness by correlating the Ag peak intensity to the inelastic mean free path (IMFP). The Ag auger intensity can be described by,

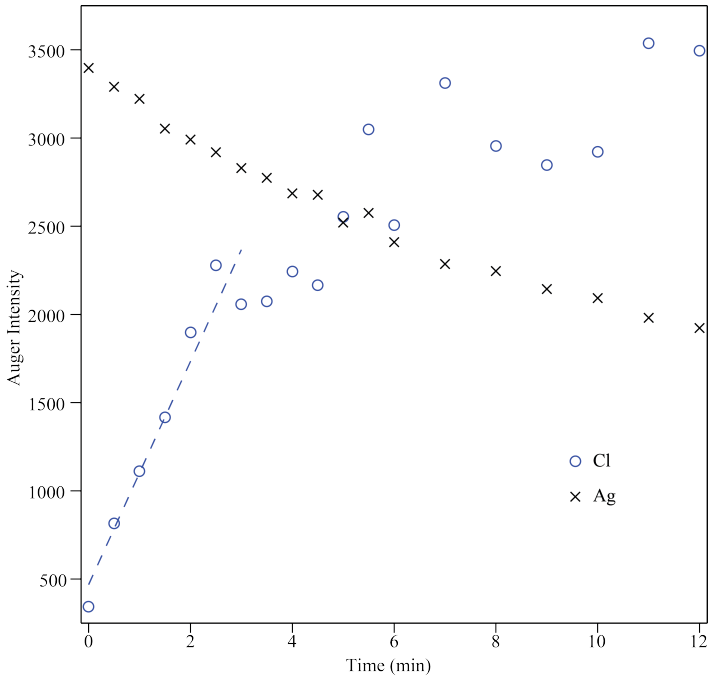

Figure 3.4: Dosing calibration rate for NaCl dosed at 810 K and Ag substrate held at 125 K for dosing and spectra. Auger intensity (Peak-to-Peak height) normalized against I_E emission current for Ag and Cl peaks. Beam energy = 1000 eV.

$$I_{Ag} = I^0_{Ag} e^{-d/eff} (1)$$

where I_{Ag} is the auger intensity, I^0_{Ag} is the auger intensity of the bare Ag substrate, d is the NaCl thickness, and $_{eff}$ is effective the IMFP. The effective IMFP determined by

$$\frac{1}{eff} = \frac{1}{355} + \frac{1}{1000} (2)$$

which accounts for the IMFP of the 355 eV electrons (16 Å) and IMFP of the attenuated beam at 1000 eV (36.8 Å) through the NaCl film, yielded eff = 11.15 Å [92]. Application of equation (1) yields the MLE occurs at 4.5 ± 0.5 min, by setting d to 2.82 Å, the distance between NaCl planes. Given that this latter method is prone to underestimate the rate of growth, we consider this be good agreement with the defined 3 MLE in this work. Application of equation (1) to calibrate growth rate is applicable to layer by layer growth, whereas NaCl shows much more complex island growth, and thus this method only serves as qualitative agreement. The slope change in the Cl peak showed to be the most sensitive and reproducible method, and is therefore taken to calibrate the dosing rate. The Auger data unambiguously demonstrates the film thicknesses studied herein are of ultrathin dimensions.

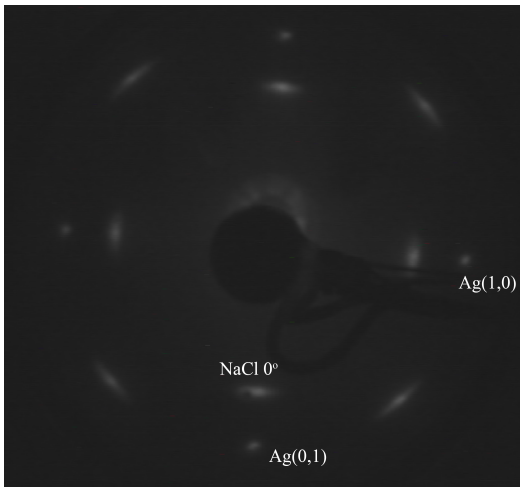

Figure 3.5: LEED of 2 MLE grown at Ag = 400 K. Spectra taken at 120 K with beam energy of 54 eV. Ag(100) and NaCl spots corresponding to 0° islands are labeled.

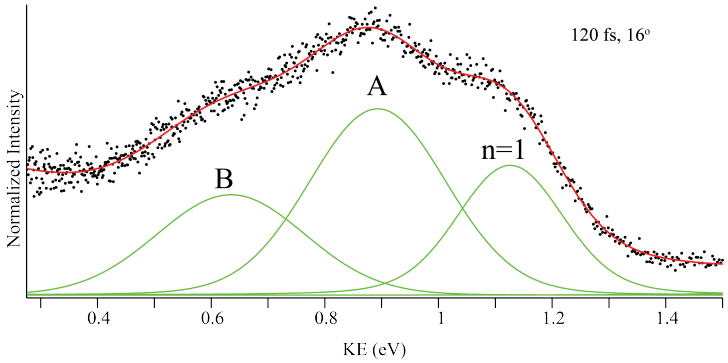

Figure 3.6: Fits of localized and delocalized states to 3 Voigts of 16° spectra at 120 fs time delay. Solid red line shows total fit, which includes an exponential multiplied by a Fermi Dirac to represent the hot electron distribution background (not shown).

Surface characterization was verified by LEED measurements as shown in Fig. 3.5. LEED measurements confirm crystalline material, and that NaCl islands are aligned 0° with respect to Ag(100). These images agree well those taken in references [61, 62, 74].

Multiple State Determination

At high dispersion angles at intermediate delays three separate states are observed. This can clearly be observed in Fig. 3.6, where the spectra in the region of interest are fit to three Voigts corresponding to the localized states A and B and the delocalized n=1 IPS.

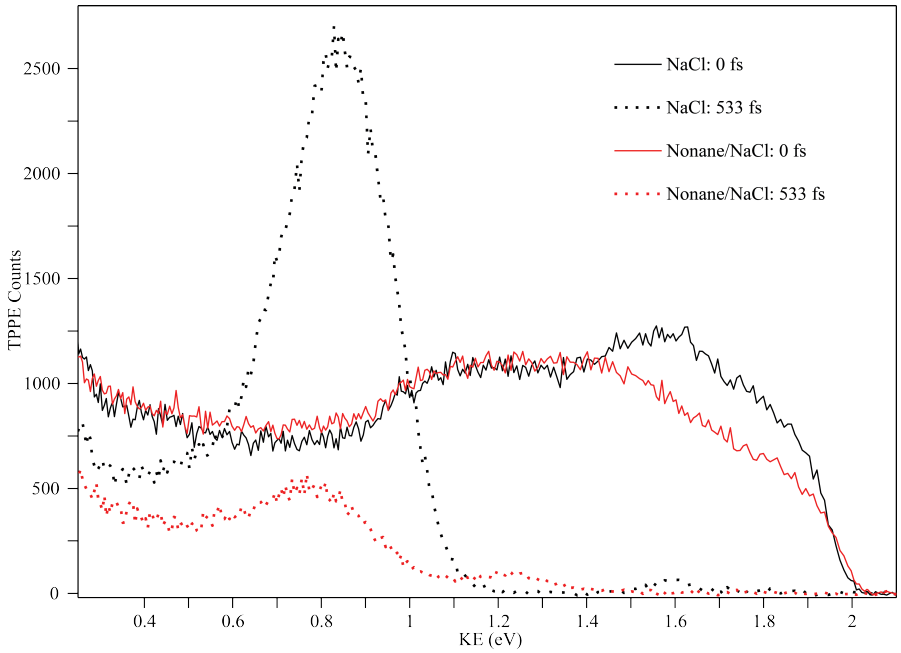

Figure 3.7: TPPE spectra 6 MLE NaCl (black) and 1 ML nonane / 6 MLE NaCL (red) at 52 K. Solid lines correspond to 0 fs delay, and dashed lines to 533 fs delay.

Nonane Overlayers

Figure 3.7 shows TPPE spectra of 6 MLE NaCl and a corresponding 6 MLE NaCl covered with $\sim$ 1 ML of nonane as calibrated with temperature programmed desorption. Nonane serves as a dielectric overlayer to distinguish whether states reside in the vacuum or inside the material. For an electron residing in the material, the electronic state should remain largely unaffected by the overlayer, but for states residing at the sample/vacuum or in the vacuum, they should be changed by the negative electron affinity of the nonane and quenched. This technique was used to show that the electron resided inside the NaCl for the case of a small polaron [73]. Our results show the populations of the initial states are similar in magnitude, but the localized state is largely decreased by the nonane overlayer, further supporting this state resides at the NaCl surface/vacuum interface. Some intensity of the localized state likely remains due incomplete uniform coverage by the nonane.

Preliminary KCl and NaF Results

Preliminary studies of KCl and NaF, shown in Fig. 3.8 and Fig. 3.9, are presented as a qualitative comparison to NaCl/Ag(100). A similar phenomena is observed, where the delocalized n = 1 IPS (0 fs, dotted line to guide the eye) undergoes population transfer to localized state with an apparent negative effective mass after a few hundred femtoseconds. The KCl data at intermediated delays (Fig. 3.8(c)) clearly show the presence of both delo-

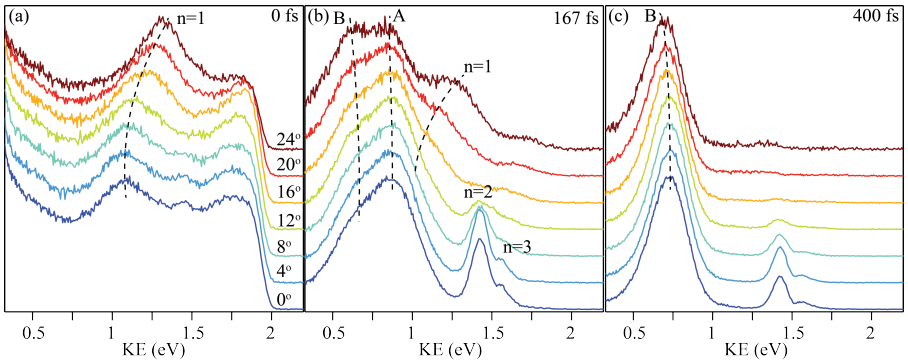

Figure 3.8: TPPE spectra of KCl dosed for 16 min at 773 K and Ag(100) at 400 K. Spectra taken at ∼130 K with pump = 3.67 eV and probe = 1.84 eV. Dispersion spectra taken at time delays of (a) 0 fs, (b) 167 fs, and (c) 667 fs.

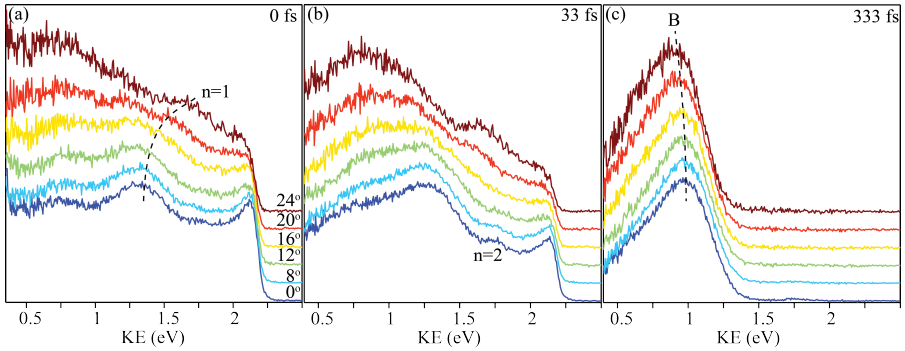

Figure 3.9: TPPE spectra of NaF dosed for 52 min at 900 K and Ag(100) at 400 K. Spectra taken at 120 K with pump = 3.79 eV and probe = 1.89 eV. Dispersion spectra taken at time delays of (a) 0 fs, (b) 33 fs, and (c) 333 fs.

calized and multiple localized states. This behavior agrees well with that observed for NaCl, and as mentioned, the band gap of NaF would exclude the conduction band from being observed in our measurements.

Chapter 4

Small Polaron Formation via Defect Intermediates at the NaCl/Ag(100) Interface

Content and figures of this chapter are reprinted or adapted from "Small Polaron Formation via Defect Intermediates at the NaCl/Ag(100) Interface" by David E. Suich, Benjamin W. Caplins, Alex J. Shearer, and Charles B. Harris.

4.1 Abstract

The trapping of delocalized electrons at ultrathin layers of NaCl on Ag(100) is investigated in real time using two-photon photoemission. Above 80 K, electrons localize to deep trap states located at low coordinated sites on the NaCl surface. Below 80 K, these trap sites serve as precursor intermediates to a new a trap state assigned to the formation of a small polaron. In contrast, electron polarons are theoretically unstable in bulk NaCl. This study is the first to directly observe the sequential population of multiple metastable deep trap states at two dimensional interfaces in real time.

4.2 Introduction

The design of molecular and nanoelectronic devices, such as transistors, memory storage, sensors, and molecular switches, requires that the active components and electrode are connected by tunneling barriers, necessitating the need for thin layer dielectrics on the nanometer scale [93]. Ultrathin layers of alkali halides have been actively studied due their strong ability to decouple molecular properties from metal electrodes. This decoupling property has been demonstrated in a variety of systems. Deposition of molecules and atoms on bilayer NaCl insulating films has allowed scanning probe measurements of neutral and metastable anionic and cationic Au states [70, 94], the isomerization of azobenzene [95], the tautomerization of naphthalocyanine [96], and imaging of molecular orbitals [90, 97].

As the length scale of future electronics is reduced to the nano-regime, electron transport across the tunneling barrier will be dominated by single electron effects [93] and carrier localization will lead to charging effects in electron transport [98]. Therefore, the identification and characterization of trap states present at the dielectric interface becomes increasingly important.

In this Letter, the excited states dynamics of NaCl/Ag(100) are investigated using angle- and time-resolved two-photon photoemission (TPPE). TPPE is an ultrafast pump-probe technique that measures photoemitted electrons as a function of time, energy, and momentum. This study builds upon our recent publication on NaCl/Ag(100), where the initial excited states observed were the delocalized image potential states (IPS) of the NaCl/Ag(100) interface [99]. Image potential states are a well known class of surface states, and arise from a free electron in the vacuum inducing an attractive polarization of charges in the sample [35, 100]. These initially delocalized electrons were observed to undergo localization by trapping at defect sites on the NaCl surface. Presently, we identify a new trap state emerging at low temperatures, and characterize the timescales and energetics of the cascade of electron localization through multiple trap states. This study is the first to observe multiple metastable trap states at two dimensional interfaces. The emerging trap state is evidence of small polaron formation via trap state intermediates in contrast to direct electron polaron formation from a free state which is known to be unstable in the bulk [101].

Experimental Methods All experiments were performed in an UHV chamber with a base pressure $\sim$5 x 10^{-10} torr. The Ag(100) surface was cleaned by standard Ar^+ sputtering and annealing for all experiments. Three monolayer equivalents (MLE) of high purity (99.999%) anhydrous NaCl was degassed and dosed from a commercial Knudsen cell setup, with the Ag substrate held at temperature of 400 K to induce large island growth of NaCl [61] at a rate of $\sim$ 0.3 MLE/min as described previously [99]. The sample could be resistively heated or cooled with LN_2 or LHe. TPPE experiements were performed using a commercial Ti:Saph oscillator and regenerative amplifier operating at 297 kHz, which was used to pump an optical parametric amplifier (OPA). The output of the OPA provided the probe pulse ($h\nu_{probe}$ = 1.89 eV), and a portion of this was frequency doubled to provide the pump ($h\nu_{pump}$ = 3.79 eV), with a combined cross correlation of $\sim$100 fs. The energy and parallel momentum of the photoemitted electrons was detected by a time-of-flight detector.

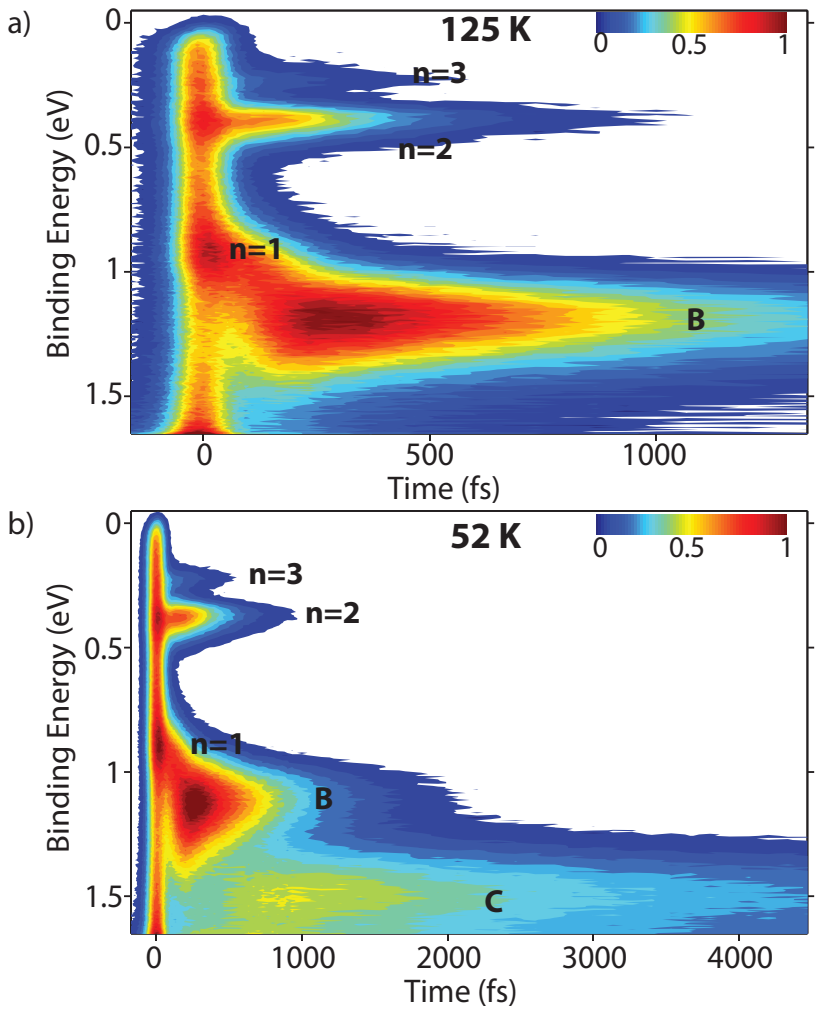

Figure 4.1: (a) False color contour plot of 3 MLE taken at 125K. (b) 3 MLE NaCl at 52 K. Note the different time scales of the two plots.

4.3 Results

Deposition of 3 MLE of NaCl on Ag(100) resulted in a workfunction decrease of $\Delta\Phi$ = -0.58 eV and global workfunction of 3.85 eV. For temperatures $\geq$ 125 K, initial excitation resulted in the population of the n = 1, 2, and 3 IPS. The delocalized n = 1 IPS electrons, as indicated in their light effective mass, m*, of 0.7 m_e (relative to a free electron, m* = 1), were shown to undergo a high probability of trapping due to electron transfer to the final localized state B [Fig 4.1(a)]. The effective mass and binding energy (BE) we reported for the n = 1 IPS deviate from that typically expected for IPS (m* $\approx$ 1 and a BE $\leq$ 0.85 eV) which is due to mixing of the n = 1 IPS and conduction band (CB) of NaCl [75, 99]. At 125 K, electron trapping in state B resulted in a binding energy (BE) gain of 0.34 $\pm$ 0.03

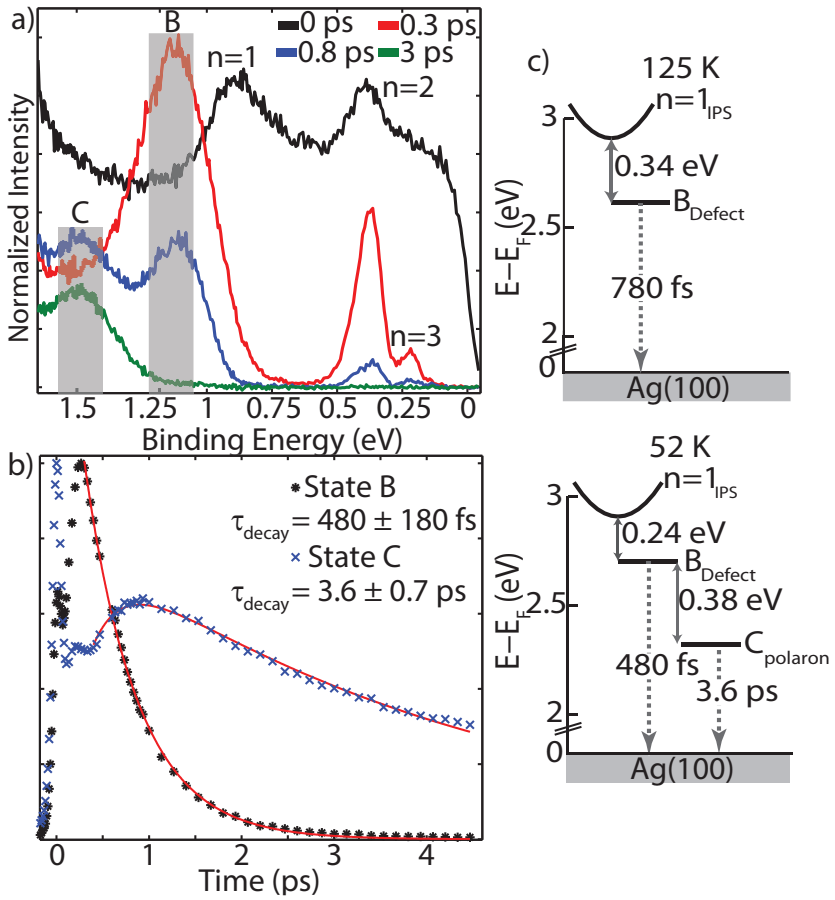

Figure 4.2: (a) Time slices of Fig. 4.1(b). Grey boxes are 100 meV integration windows for population dynamics. (b) Population dynamics for state B and C. State B is fit to a single exponential decay, whereas state C shows a delayed exponential rise and decay. See Supporting Information for further details. (c) Summary of electron trapping and decay lifetimes at 125 K and 52 K.

eV and an increased decay lifetime, τ_d, of 780 fs.

This picture significantly changes when the sample is cooled to ∼50 K. Shown in Figure 4.1(b), a new state, labeled C, appears at long time delays and higher BE. For 3 MLE NaCl, the n = 1 has a BE of 0.88 ± 0.02 eV relative to E_{vac}. Electrons trapping to state B results in a BE gain of 0.24 ± 0.02 eV, and are located at a BE of 1.25 eV. This is in good agreement with the linear temperature dependent trapping energy of 1 meV/K between the n = 1 IPS and B observed for 125 - 350 K [99]. Further trapping to state C leads to an additional energy gain of 0.38 ± 0.02 eV to a final BE of 1.5 eV, and a combined final trapping energy of 0.62 eV. Angle-resolved measurements for state C at time delays of 0.5 and 1 ps show the state to have a flat band indicating its localized character [Fig. 4.5].

Having established the trap state energetics, we now turn to the timescales of electron

trapping at ∼50 K [Fig. 4.2]. Electrons initially excited into the delocalized n = 1 IPS decay on the ∼100 fs timescale, and localize due to population transfer to state B. Electrons trapped in state B, stabilized by 240 meV, have an increased decay time, τ_d = 480 ± 180 fs. At longer timescales (∼500 fs), state C becomes observable, but shows a nearly order of magnitude increased τ_d = 3600 ± 700 fs compared to state B. A summary of the trap state energetics and decay lifetimes are presented in Figure 4.2(c).

Next, we quantify the transition temperature for observing state C. Figure 4.3(a) shows the energetic region of state B and C at Δt = 2 ps for various temperatures. At this time delay, all IPS electrons have decayed, and only B and C are observed. At 90 K, the majority of trapped electrons reside in state B. Cooling to 80 K results in approximately equal intensity in state C and B. Finally, at 70 K, the majority of trapped electrons now reside in state C. Taking the Voigt fitted amplitude difference between state B and C at Δt = 2 ps from 60 K - 110 K, we find step like behavior [Fig. 4.3(b)]. Fitting this data to a sigmoid function, we extract a transition temperature, T_C, of 81 ± 8 K. Additionally, we find the disappearance (emergence) of C is reversible upon heating (cooling) the sample.

The shift in the majority of the trapped electron population from state B to C as the sample is cooled from 100 K to 60 K arises due to the change in state B's decay lifetime [Fig 4.3(c)]. As the sample is cooled, B's τ_d shows a step like decrease, and additional fitting of this trend to a sigmoid extracts T_C = 77 ± 8 K. The decreasing lifetime versus decreasing temperature from 60 K - 100 K contradicts the behavior reported previously from 125 K - 350 K. Over that range, B's τ_d exhibited Arrhenius-like behavior where τ_d increased as temperature decreased, due to thermally activated tunneling back to the metal substrate. The reversed behavior arises from state C opening a new pathway for decay of state B in addition to decay back to the metal substrate. While the two analyses of the transition temperature are in good agreement with one another, it is important to note the two are directly linked to each other, i.e. as the lifetime changes, the intensity at long time delays will change. However, if the two states were not coupled, there is no reason for this redundancy to exist. This serves to support the conclusion that state C is populated from electron transfer from trapped electrons in state B. Electron transfer from state B to C is also supported by the delayed observation of C after state B intensity maximum and after the majority of the IPS electron population has decayed.

4.4 Discussion

We note neither of the deep trap states observed herein have been previously identified in numerous scanning probe measurements of the NaCl/metal interface [102, 103, 104, 88, 64, 65], which is likely due to the fact that population of the trap states B and C in our experiments are dynamical in nature and occur on ultrafast timescales making them inaccessible to scanning probe measurements that have poor time resolution. Nor has dynamic electron localization at two dimensional interfaces, such as trapping at preexisting surface defect sites on amorphous ice [21], small polaron formation in alkane overlayers [47], or solvation in thin

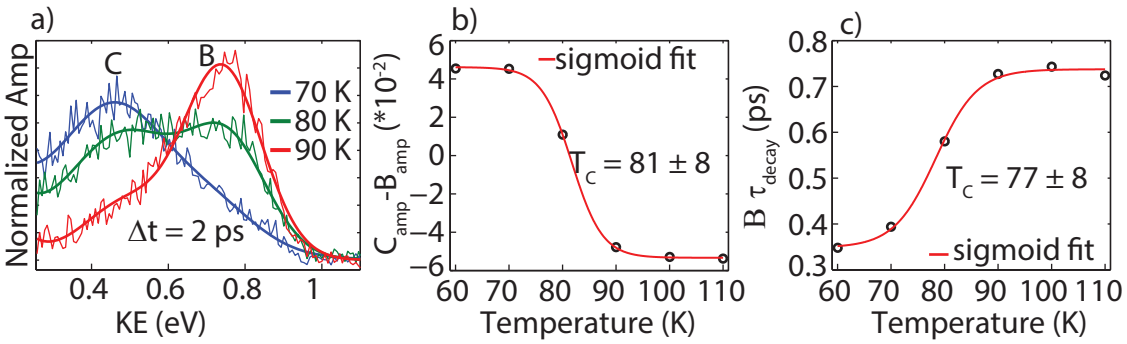

Figure 4.3: (a) 3 MLE of NaCl grown at decreased a rate of 0.02 MLE/min. Zoom in on region of state B and C at a time delay of 2 ps for temperatures of 70, 80, and 90 K. (b) Sigmoid fit of the Voigt amplitude difference between B and C for Δt = 2 ps versus temperature. (c) Sigmoid fit to State B's τ_d versus same temperature range.

films of acetonitrile [42], identified multiple distinct deep trap states. Previous reported cases of electron localization in two dimensions observe an initially delocalized electron's wavefunction collapsing to a single localized state, whereas presently, we observe the cascade of electron transfer between multiple trap states.

Trap state B is assigned to low coordinated defect sites, such as step edges and kinks, on the NaCl surface [99], and further supported by dynamic force microscopy experiments which observed an increased negative tip-sample interaction at step edges and kinks relative to terrace sites [102]. However, assigning state C proves more difficult. Previous TPPE studies of 2-5 ML NaCl/Cu(111) assigned an electron excited into the delocalized CB and surface CB formed a small polaron, evidenced by a dynamic and continuous increase in the electron's effective mass, i.e. moving from a delocalized state to a localized state. Localization coincided with a continuous energy relaxation of 60 meV occurring on the 100 fs timescale [73]. This is in stark contrast to our results, which shows localization to be a discrete process, i.e. distinct delocalized and localized states exist simultaneously after early time delays [99]. Additionally, localization in our experiment occurs through multiple localized states and a much greater energy gain and enhanced lifetime. Theoretical calculations of 1-4 ML NaCl on Cu(111) found the lowest excited states correspond to the n = 1-3 IPS mixed with the conduction band [75]. Our results [99] and these theoretical calculations support the assignment of the CB and surface CB as the n = 2 and n = 3 IPS in reference [73]. It should be noted that because the n = 1 of clean Cu(111) was observed, the Shockley state is also experimentally accessible though it was not commented on in [73]. Based on the experimental energies used, this would place the virtual intermediate state of the SS at $\sim$3.79 E-E_F eV, which directly overlaps with the reported surface CB. Thus, part of the light $m^* = 0.6$ observed for the surface CB and energetic relaxation arises due to overlap of the surface state of Cu(111) with the n = 2 IPS, and that insufficient probe energy prevented observation of the deep trap states.

We rule out state C as a different pre-existing defect site, because if state C were pre-existing, electrons would preferentially localize to state C over B due it being more energetically favorable. This can be further ruled out from establishing that state C forms from pre-localized electrons in state B and after the initial delocalized electrons have decayed. We can also rule out state C being a charged defect, such as an F-center, because as mentioned these require large energies to form and not present in sufficient concentration. The sample was periodically flashed to temperatures > 175 K and immediately cooled, which had no effect on observing state C at low temperatures. Thus we rule out state C being caused by adsorption of residual gases. By reason of the highly localized state B serving as an intermediate to the formation state C, it follows state C exists spatially in close proximity to state B while itself not being another pre-existing defect. Consequently, we conclude a dynamic change occurs in the system allowing state B to evolve into state C, which we assign to the formation of a small polaron.

A small polaron arises from charge carrier in a solid inducing a polarization and displacement of the lattice atoms resulting in an attractive potential well [105]. Forming a small polaron involves the competition between delocalization and localization energies, and can be expressed as,

$$E_{st} = E_{loc} - E_{rel}$$

where E_{st} is the self trapping energy, E_{loc} is the localization energy, and E_{rel} is the lattice relaxation energy [Fig. 4.4] [101]. Localizing an electron residing in its lowest kinetic energy state at the bottom of a free band without lattice distortion, point F, requires the mixing of all Bloch states to form a localized wave packet, point C. The cost of localization, E_{loc}, can be approximated from half the band width ΔE, and due to the large conduction bandwidth of NaCl, makes electron polaron formation unstable [73, 106]. Localization is favored by an attractive potential well created by electron induced lattice distortion, termed E_{rel} at point S in Figure 4.4. Only when E_{st} is ≤ 0 is a small polaron formation stable. The rate of polaron formation will also depend on energy barriers, E_a, and transfer matrix elements between localized states.

We propose state C corresponds to the formation of a small polaron, however, we note a critical distinction from TPPE studies of polaron formation reported for NaCl [73] and alkanes [47]. Rather than direct formation of a small polaron from an initially delocalized state, state C only forms after electron transfer through intermediate localized states. Polaron formation in alkane thin films was supported by an analysis of the temperature and driving force dependent localization rates. The present system prevents a similar analysis because the assigned polaron is only stable at low temperatures and the precursor state is localized rather than delocalized. Theoretical calculations of an electron in deformable medium is often treated adiabatically using the the Holstein model [107]. In this model, polaronic states are localized stationary states of the Hamiltonian, which can be written as $H_{tot} = H_{el} + H_{lat} + H_{int}$, where H_{el} describes an electron in a tight-binding picture, H_{lat} describes the phonons as independent oscillators, and H_{int} describes the electron-lattice interaction [108]. Interestingly, our results are in qualitative agreement with simulations

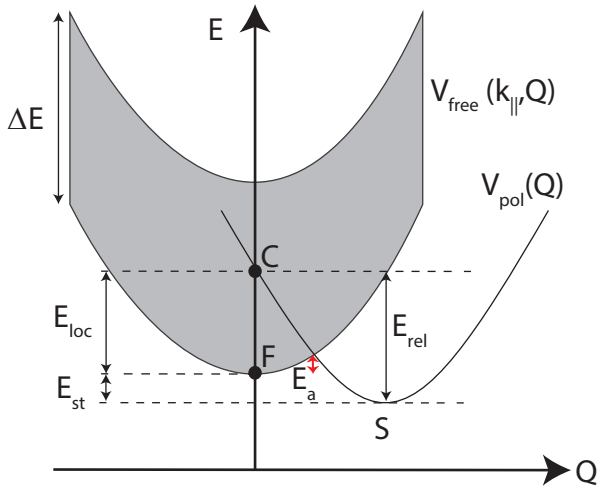

Figure 4.4: Adiabatic curves for electron self trapping along lattice coordinate, Q. $V_{free}(k_{||}, Q)$ and $V_{pol}(Q)$ represent the free and polaron states, respectively. Light grey shaded curve represents distribution of free states of different $k_{||}$. ΔE represents the band width, E_{st} is the self trapping energy, E_{loc} is the localization energy, E_{rel} is the lattice relaxation energy, and E_a is the activation energy.

using the Holstein model to describe electron dynamics in a 2D system which predicted self trapping occurred through a series of intermediate localized states rather than directly from a free electron state. Localization to intermediate states was found to lower the energetic barriers to localization creating the fastest path to polaron formation [109]. The combination of defect trapping and self trapping is well established [110, 111, 112, 106, 113], where energetic disorder can reduce electron-phonon coupling needed to result in stable small polaron formation [110]. Further results from Holstein model suggest lower coordination sites, as proposed herein, facilitate the lattice deformation in electron trapping [108]. Because the electron is trapped *a priori* to the polaron, the large barrier to go from a delocalized electron to localized polaron is removed, and formation then should strongly depend on the matrix elements determining the diffusion between the two localized states.

Another possible assignment for state C comes from gas phase photoelectron studies of stable $(NaCl)_n^-$ clusters (n = 2-13) [89]. Modeling of these systems found the excess localized at corner Na^+ ions, F-center like states, or states spread over the cluster surface. However, one important feature was that all possible modes resulted in significant deformation of the lattice to accommodate the excess electron. Although these clusters are too small to make detailed comparisons to the present work, we note that they found that the theoretical electron binding energies for the unrelaxed clusters were spread from 0.06 eV to 1.0 eV depending on the cluster, which is on the same scale to the present results [114]. Thus the other possibility is that after the electron has localized at low coordinated defect sites, at low temperatures the lattice is able to deform about the excess trap electron forming state C.

The emerging trap state, observed for thermal energies < 7 meV, cannot be assigned to any physical change in structure, as no significant change in surface structure was observed from Tensor low-energy electron diffraction studies over the range of 25 K to 230 K. The study did find a potentially greater cation vibrational amplitude (compared to anion amplitude) below a temperature of 100 K [91], which could create a favorable potential to bind the electron [75]. The ability of the NaCl to polarize and stabilize a negative charge has been demonstrated by the STM observation of stable Au^{-1} on a bilayer NaCl substrate and explained due to the NaCl lattice polarizing about the anion [70]. Supporting DFT calculations found a lowering of the Au^{-1}/relaxed NaCl lattice potential energy curve of 0.53 eV relative to the neutral Au^0/NaCl geometry [115], which is of a similar magnitude to our observed electron self trapping energy of 0.38 eV. One possible explanation for the observed transition temperature is that as temperature increases, phonon population increases, but can result in a decreased electron-phonon interaction that might prevent polaron formation [116].

The mechanism of small polaron formation remains an ongoing debate as to whether (i) carrier self trapping occurs at "preexisting precusor states" or (ii) the initially excited carrier induces its own potential well in a perfect lattice [117]. Dosing 3 MLE at an order of magnitude decreased dosing rate of 0.02 MLE/min results in a loss of a pronounced rise and overall intensity loss state C's population [Fig. 4.7]. Reduction in dosing rate should result in a decrease of defect density, which results in a loss of defect precursor sites for small polaron formation. Our results strongly support a polaron formation mechanism that only occurs at "preexisting precursor states". Ultimately, further detailed experimental and theoretical studies are needed to provide further insight into the nature of the emerging trap state at low temperatures.

4.5 Conclusions

In conclusion, we used time-resolved TPPE to identify and characterize the excited state dynamics of excess electrons at the NaCl/Ag(100) interface. After initial excitation to the delocalized IPS, electrons are observed to go through a series of deep trap states. The first deep trap state is assigned to electrons trapped at low coordinated sites on the NaCl surface such as step edges and island kinks. Below the transition temperature of 79 K, a new trap state emerges, and is assigned to small polaron formation. Unlike previous theoretical calculations that predict a delocalized conduction band electron in NaCl undergoing self trapping to be unstable, we identify a stable route to small polaron formation. The initially delocalized n = 1 IPS is first trapped at defects, and then is able to form a small polaron.

4.6 Supplemental Information

State C Dispersion

Angle-resolved measurements for state C are provided to show the localized nature of the state. Due to state C's energy overlap of the low energy cutoff, accurate peak determination and effective mass fits were prevented. However, once state C was experimental observable, no dispersive feature for the state was observed, and only a flat band was observed indicating state C's localized wavefunction character.

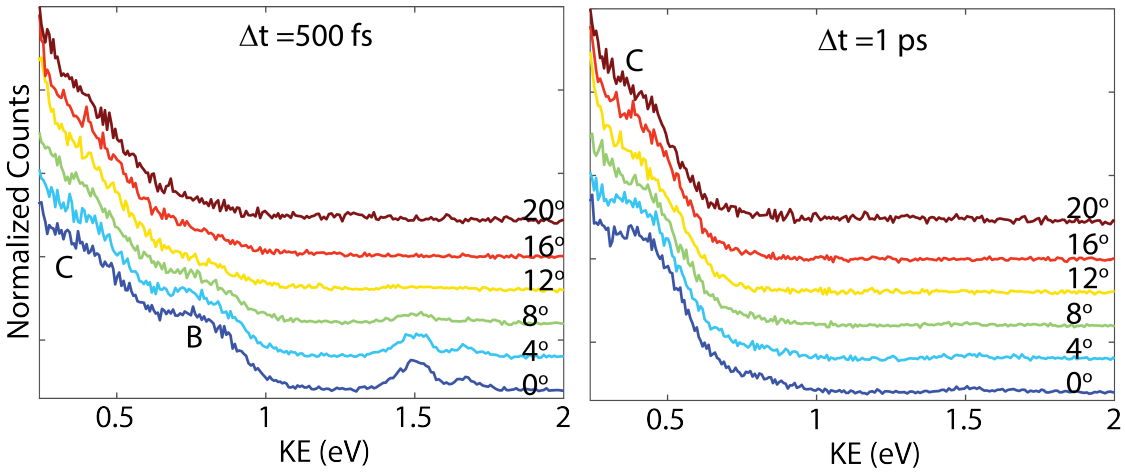

Figure 4.5: Angle-resolved measurements of state C taken at time delays of 500 fs (left) and 1 ps (right). Sample is of 3 MLE NaCl on Ag(100) at ∼50 K and taken with pump-probe wavelengths of 327 nm and 653 nm. Spectra are normalized and shifted for viewing.

Time Fits for Trap States

As noted in Figure 4.2, the population intensity for state C at 52 K exhibits an exponential rise and decay, and is fit to,

$$N_C(t) = A * \frac{k_1}{(k_2 - k_1)} * [exp(-k_1 t) - exp(-k_2 t)] + baseline$$

where $N_C(t)$ is the population of state C at time t, A is a pre-exponential factor, and k_1 and k_2 are the rates for decay and rise. The observed rise time is not intrinsic to the formation and population of state C, but rather depends on the film thickness and dosing conditions, as evidence below. Additionally, due to the island growth nature of NaCl on noble metal surfaces, trap state population kinetics reflect that of an ensemble of trap states over a distribution of configurations. The delayed rise in state C is further complicated by the delayed rise in state B from inter- and intra-band relaxation for higher lying states. As a

result of these factors, the rise time extracted from the above fit does not physically represent the decay rate for B $\rightarrow$ C population transfer, and is therefore not reported.

Behavior of Trap States on Film Conditions

As noted above, the observed rise time is not intrinsic to small polaron formation, but rather dependent on film conditions. This is demonstrated in Figure S1 and S2. Figure S1 shows the behavior of trap states above and below the state Cs critical temperature for 6 MLE, double the coverage, at a dosing rate of 0.3 MLE/min. We observe an exponential increase in state Bs decay lifetime at 125 K of 8.4 ps (versus 0.78 ps for 3 MLE) because NaCl serves as a tunneling barrier for electron decay back to the metal substrate. Upon cooling to 55 K, we observe qualitatively similar behavior of decrease in state Bs decay to 1.1 ps as electrons in B can transfer population to state C in addition to decay to the metal. Additionally, we observe an increased rise time of 700 fs of state C (compared to 230 fs 3 MLE), indicating the formation of state C is linked to the decay time of state B. At these thicker coverages, state Cs τ_d is also observed to exponentially increase to 73 ps.

For 3 MLE of NaCl dosed a slower rate of 0.02 MLE/min shown in Figure S2, we again observe different behavior in the trapping timescales. Below the state Cs critical temperature at 60 K, we no longer measure an observable rise time in state Cs population, and τ_d has decreased to 1.6 ps. The most likely explanation for the difference observed in state Cs behavior for the same coverage at different dosing rates is due to difference in defect density (step edges and kinks).

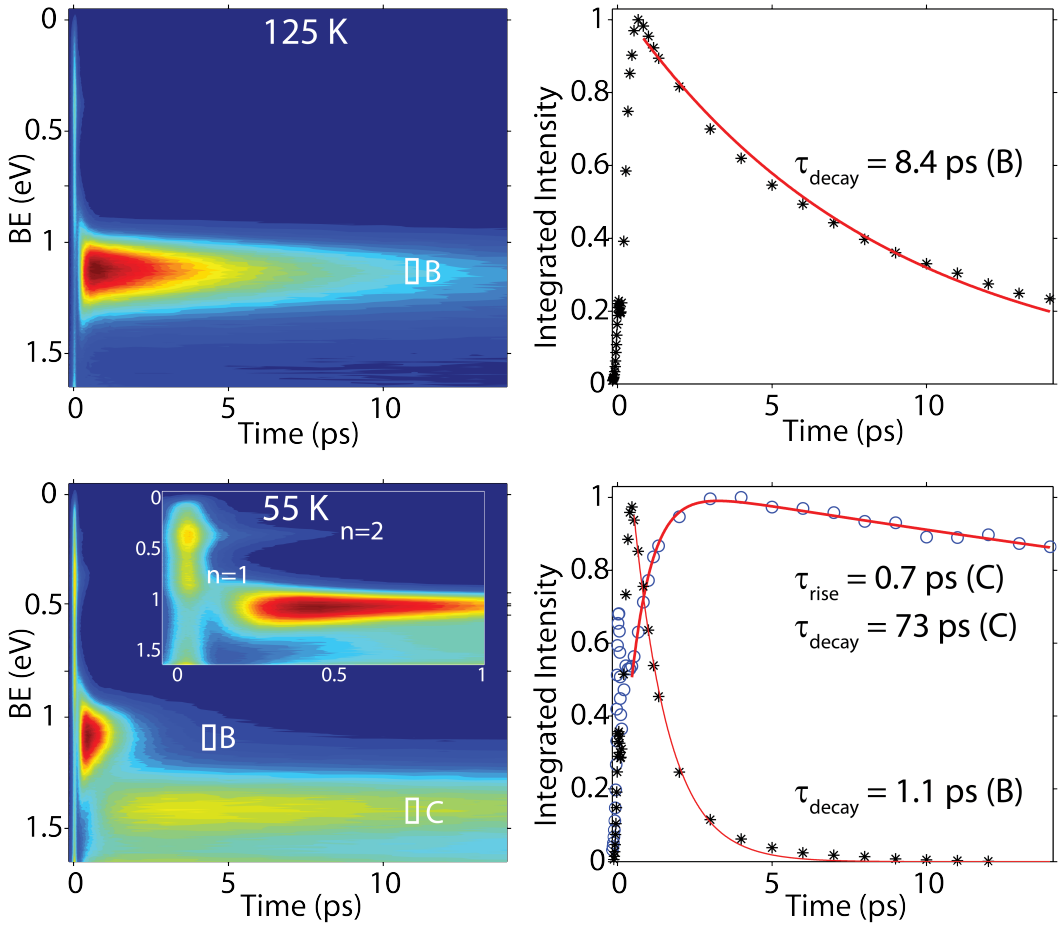

Figure 4.6: False color contour plots of 6 MLE of NaCl grown at a dosing rate of 0.3 MLE/min and corresponding 100 meV integration normalized windows (white boxes) for trap state cross correlations and time fits. Top panel shows spectrum at 125 K when state C is not observed and bottom, spectrum at 55 K. Inset shows the first picosecond after excitation.

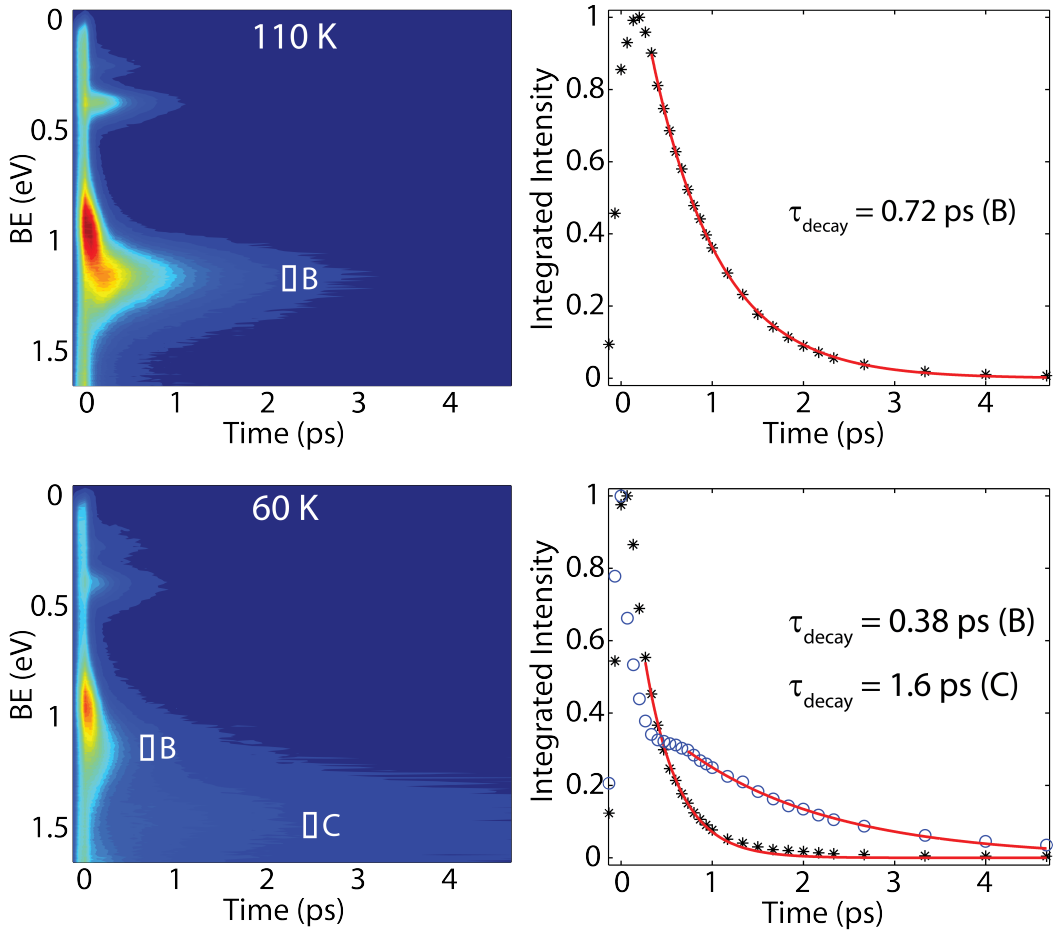

Figure 4.7: False color contour plots of 3 MLE of NaCl grown at a dosing rate of 0.02 MLE/min and corresponding 100 meV integration normalized windows (white boxes) for trap state cross correlations and time fits. Top panel shows spectrum at 110 K when state C is not observed and bottom, spectrum at 60 K.

Chapter 5

Variations on a Theme: Alkali Halides on Noble Metal Surfaces

5.1 NaCl on Cu(111)

Prior to the work in this thesis, the only ultrafast studies of electronic states and dynamics at alkali halide-metal interfaces were those carried out by Muntwiler, M. and Zhu, X. Y. of 2-5 ML NaCl on Cu(111) which has been discussed in Chapters 3 and 4 [73]. A brief discussion of their conclusions is provided to explain the discrepancies between their work and the work herein. Upon initial excitation, electrons were injected into the conduction band (CB) and surface conduction band. Both of these states showed dispersive (delocalized) features, with $m^* = 0.8m_e$ and $0.6m_e$ for the CB and surface CB, respectively. The delocalized CB and surface CB electrons were observed to undergo a continuous energetic relaxation of 60 and 85 meV, respectively, over the course of the first 100 fs. The continuous energetic relaxation coincided with a continuous flattening of the band dispersion, i.e. moving from a delocalized wavefunction to a localized wavefunction. The cause of energy relaxation and localization was assigned to the formation of a small polaron. This was further supported by the adsorption of a nonane overlayer, which was shown to have little impact on the CB and surface CB dynamics and intensity, indicating these states exists within the NaCl film. Finally, the decay lifetimes of the small polarons formed from the CB and surface CB were 110 and 170 fs, and noted to be independent of film thickness [73].

The energy of polaron formation (self-trapping energy) was estimated according to the equation,

$$E_{ST} = E_{pol} + E_{loc} + E_{bond}$$

where E_{ST} is the self-trapping energy, E_{pol} is the energy gained from lattice polarization, E_{loc} is the cost of electron localization estimated by $\approx 0.5\Delta E$ (half the CB bandwidth), and E_{bond} corresponds to the bond energies formed as a result of lattice distortion ($Na\text{-}Na^+$). Using literature values and approximations, the estimated self-trapping energy for an electron polaron in NaCl in 2D was $E_{ST} \approx$ -0.3 eV. This is clearly much larger than

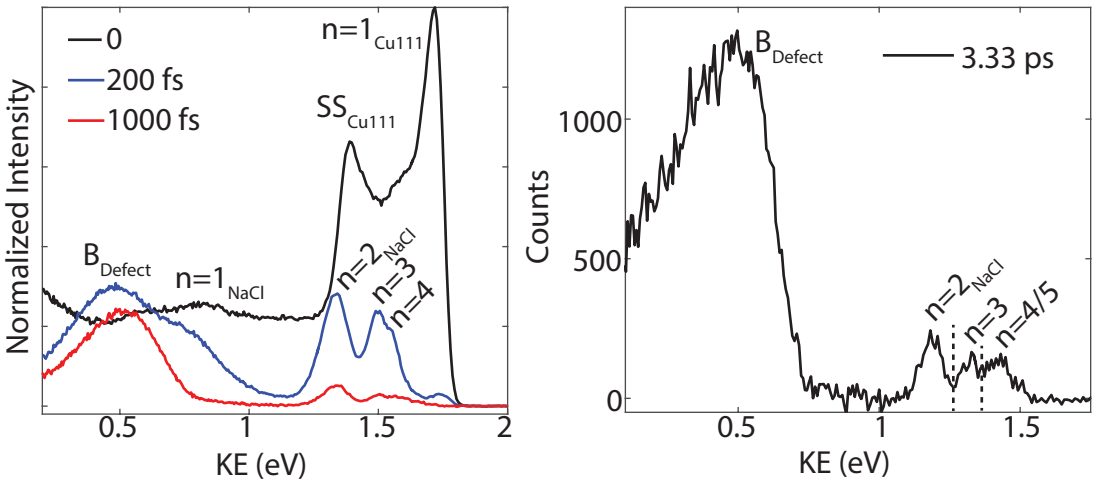

Figure 5.1: TPPE time slices of 26 min NaCl dosed at 790 K, Cu = 400 K, spectra = 120 K, 600 nm vis probe, 300 nm UV pump. Time slices show clear evidence of IPS series of the NaCl/Cu(111) interface, up through the n = 5 IPS.

the energetic relaxation observed for polaron formation of 0.06 and 0.085 eV. Interestingly, the estimated E_{ST} is of similar magnitude with the energetic stabilization observed between states B and C in Chapter 5. However, prior to undertaking the experiments of NaCl in our lab, the expected result was to observe the CB and surface CB and the dynamic formation of a polaron. There clearly exists a number of major differences between our two conclusions, and these will be discussed in the following and supported by our own measurements of the time-resolved photoelectron spectra of NaCl on Cu(111).

INITIAL EXCITED STATES: The first major differing conclusion is the assignment of the initial excited states corresponding to the CB and surface CB versus the IPS series of the NaCl/Cu(111) interface. As noted in Chapter 4 and theoretical calculations of the excited states of NaCl/Cu(111) interface [75], our conclusion was that initial excited states correspond to the IPS series. Shown in figure 5.1 are TPPE spectra of an ultrathin film of NaCl on Cu(111). Upon initial excitation, much of the spectrum is dominated by the Shockley surface state (SS) and n = 1 IPS of clean Cu(111) patches of the sample. At later time delays, the SS and n = 1 of clean Cu(111) have quickly decayed, and the IPS series of NaCl is clearly observed. The right-hand side of figure 5.1 shows a long time delay of 3.33 ps and long integration time showing the peaks for IPSs of n $\geq$ 4, thus unambiguously establishing the initial excited states of the NaCl/Cu(111) correspond to the IPS and not the CB and surface CB of NaCl. The likely interpretation is that the CB and surface CB are the n = 2 and n = 3 IPS in reference [73].

ENERGETIC RELAXATION AND LOCALIZATION: The next difference in conclusions concerns the magnitude of energetic relaxation and localization. In reference [73], localization was observed to occur as a continuous increase in the effective mass and flattening of the band. This is in sharp contrast to the localization observed in Chapter 4, which

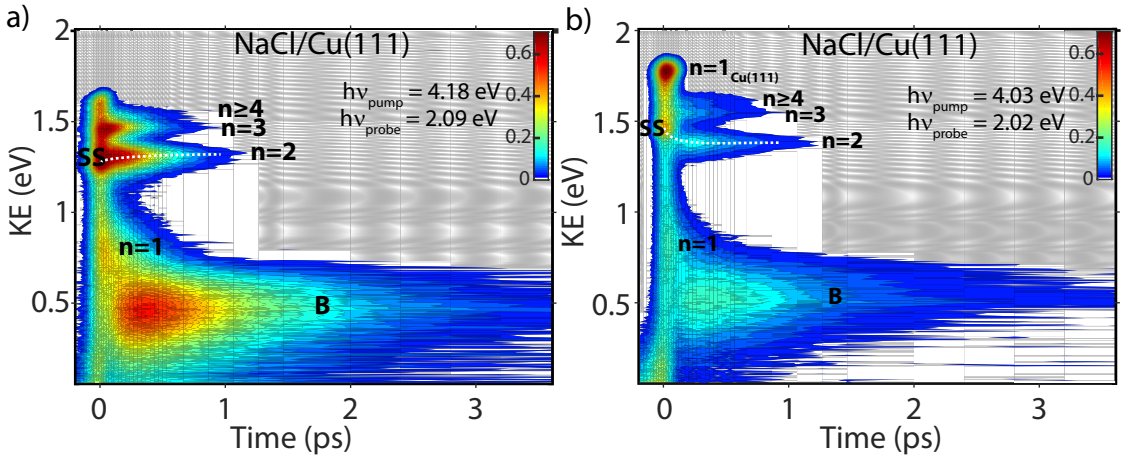

Figure 5.2: (a) Log scale false color contour plots of ∼2 MLE of NaCl on Cu(111) at a sample temperature of 130 K and pump-probe wavelengths of 297 nm and 597 nm. b) Same as (a) but with pump-probe wavelengths of 308 nm and 615 nm. White dotted lines serves to guide the eye to the apparent blue shift or red shift of the n = 2 IPS due its overlap with the Shockley state (SS) of clean Cu(111).

observed it to be a discrete process where localized and delocalized states existed simultaneously. Thus localization arose from population transfer from the delocalized n = 1 IPS of NaCl/Ag(100) to the localized defect trap state B. It should be noted in the work of [73] that n = 1 of clean Cu(111) was observed, whereas the SS of clean Cu(111) was not. Shown in figure 5.2 are two contour plots of ultrathin layers of NaCl on Cu(111) at wavelengths of 594 nm and 615 nm. The plot serves to show the critical point that thr SS is clearly experimentally observed, and overlaps strongly with the n = 2 IPS of the NaCl/Cu(111) interface. Depending on the wavelength selection, the location of the virtual intermediate state of the SS shifts, and results in an apparent red or blue shift of the n = 2 IPS. Consequently, it seems plausible part of the 85 meV energetic relaxation observed in reference [73] arises as a result of the overlap of the SS and the n = 2 IPS. Another important consequence is the impact of the light effective mass observed of $0.6m_e$. Noting that the SS of clean Cu(111) has an $m^* = 0.412m_e$ [29], this would result in lighter observed effective mass for the overlapping SS and n = 2 IPS at early delays.

The next matter to verify is the consistency of observed electron localization for NaCl on Ag(100) and on Cu(111). Shown in figure 5.3 are angle-resolved measurements of ultrathin layers of NaCl on Cu(111) at time delays of 0 fs, 107 fs, and 400 fs- similar to that shown in Chapter 3 and [99]. At 0 fs, the higher-lying IPSs are obscured by the n = 1 and SS of clean Cu(111), and thus accurate measurements of their effective masses are prevented. The n = 1 has an $m^* = 0.6m_e$, similar to the observed n = 1 $m^* = 0.7m_e$ for NaCl on Ag(100) at $\Delta t = 0$ fs [99]. The light effective mass ($m^* < 1$) was explained due to mixing of the n = 1 IPS and dispersive CB of NaCl. Accurate determination of the effective mass

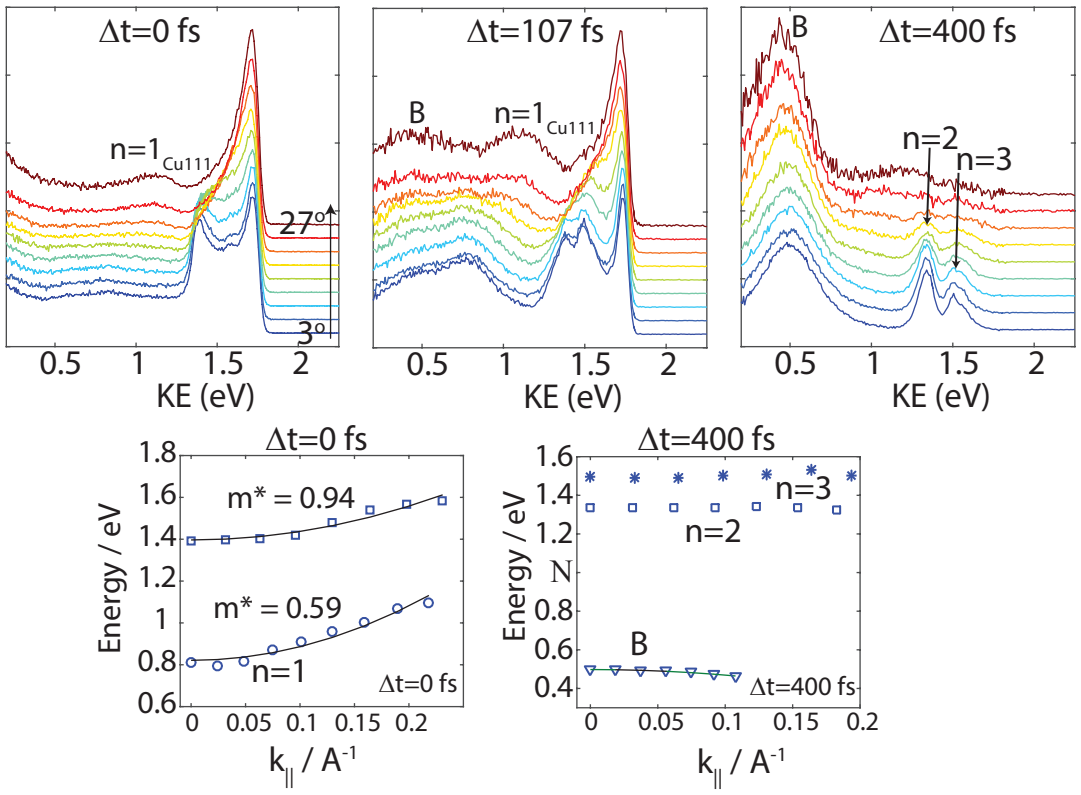

Figure 5.3: NaCl on Cu(111). Angle-resolved measurement of 26 min NaCl dosed at 790 K, Cu = 400 K, spectra = 130 K, and 601 nm at time delays of 0, 107, and 400 fs. Effective mass fits are shown for time delays of 0 fs and 400 fs, revealing the dispersive n = 1 IPS and localized state B.

is also complicated by the broad feature for the n = 1 and large hot electron background present at early delays. However, evidence of the dispersive and therefore delocalized nature of the n = 1 IPS is clear. Similar to NaCl on Ag(100), at intermediate delays of $\approx$ 100 fs, the delocalized n = 1 and localized state B are observed simultaneously, as well as some evidence of the short-lived localized state A. Finally, at longer time delays of hundreds of fs, the localized state B (flat band) is evident and dominates the spectra. These results are in very good qualitative agreement with our results on Ag(100), indicating the physics of localization is the same, and the results are generalizable.

These results show the consistency of the dynamics of NaCl on Ag(100) and Cu(111) and serve to answer the discrepancy between the work herein and that of reference [73]. There is clear evidence of localization in [73], but this could likely be attributed to the inhomogeneous energetic landscape causing localization. Additionally, because the probe wavelength was 800 nm in those experiments, the n = 1 and trap states were likely inaccessible.

A question that might arise is whether electron trapping occurs from population transfer from the n = 1, or whether higher-lying IPS (n $\geq$ 2) must be populated to observe the

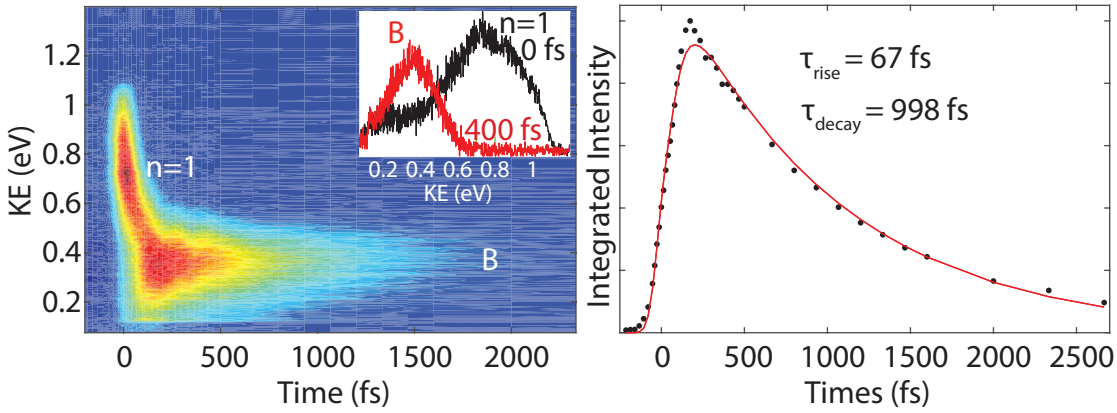

Figure 5.4: Left: False color contour plot of 26 min NaCl dosed at 790 K, Cu = 400K, spectra = 130 K, and 690 nm. Inset: Time slices at 0 and 400 fs. Right: Integrated population intensity and time fits for state B.

long-lived trap state. Because Cu(111) has a greater workfunction compared to Ag(100) and Ag(111), this could be tested by taking spectra at red shifted wavelengths. Shown in figure 5.4 is false color contour plot of ultrathin layers of NaCl on Cu(111) taken at 690 nm. The contour plot, and inset showing individual time slices, clearly shows only the n = 1 IPS of NaCl is populated at this wavelength without being obscured by the surface states of Cu(111). The n = 1 IPS electrons are shown to undergo population transfer on the sub-100 fs timescale to state B, where they are energetically stabilized and have a substantially longer lifetime of nearly 1 ps compared the $\approx$ 50 fs lifetime of the n = 1. Thus, it seems plausible that the primary source of state B's population is the trapping of the n = 1 electrons.

5.2 NaCl on Ag(100)

In Chapter 2, the temperature of the substrate during dosing was shown to have a large impact on NaCl island growth. If the substrate is held at temperatures $\leq$ room temperature (RT), islands of 1 ML height form. However, if the substrate is held elevated temperatures above RT, islands of 2 ML in height were shown to form. As temperature increases, the rectangular size of the 2 ML height islands increases. One obvious question then becomes what is the impact of 1 ML versus 2 ML islands on the excited state dynamics. This question is answered in Figure 5.5, which shows 6 min of NaCl (2 MLE) dosed while the substrate was held at 122 K (top) and 400 K (bottom) in order to grow 1 ML and 2 ML islands. LEED images for each sample are shown to the right of the contour plots and taken at the same beam energy for comparison. The contour plots are taken at the same sample temperature of 122 K. When 1 ML islands are grown, the clear image potential state series disappears. While some energetic relaxation is observed, it is less than that of 2 ML, and the electron dynamics show much shorter lifetimes. However, when 2 ML islands are grown, the clear

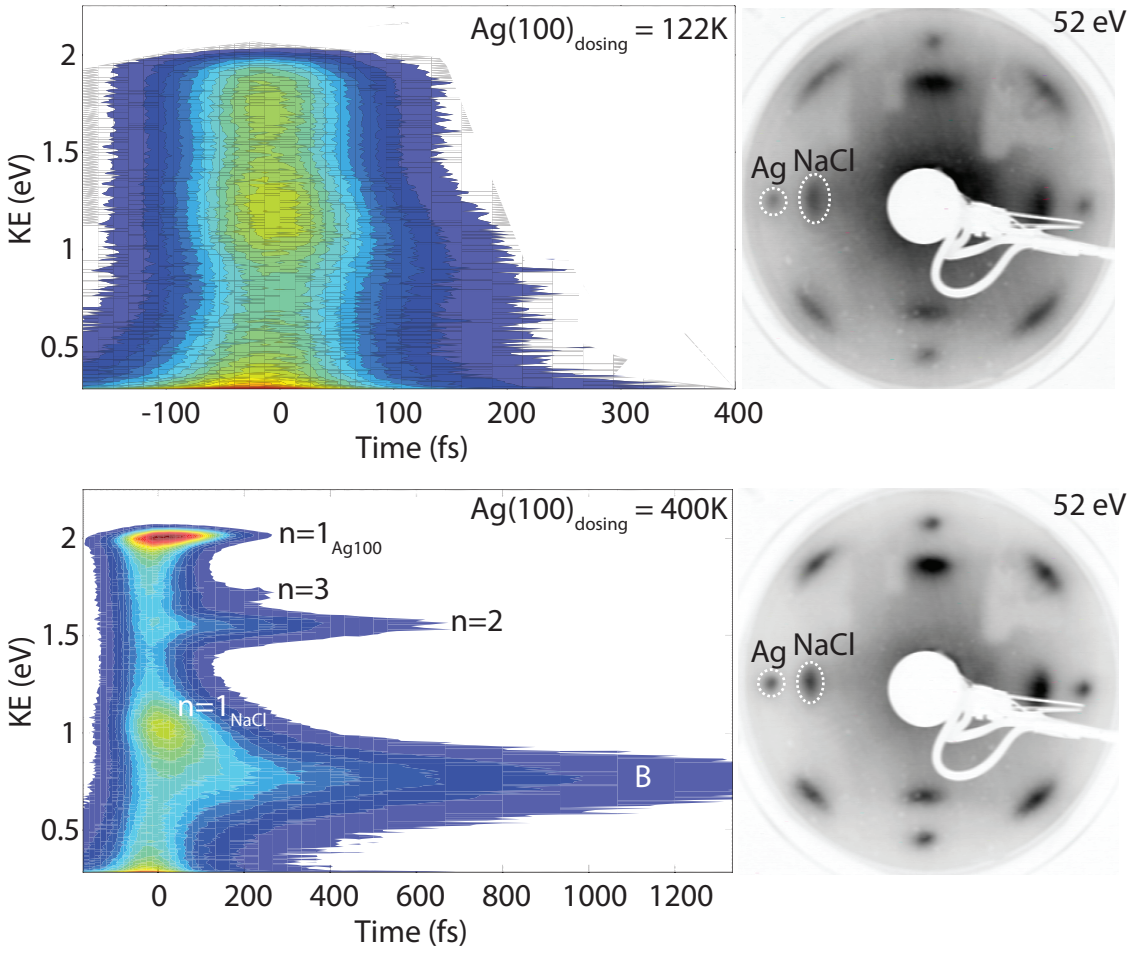

Figure 5.5: Top: 6 min NaCl (2 MLE) dosed while Ag(100) = 122 K. Contour plot taken at 122 K sample temperature and 638 nm. LEED image of cold sample dosing at 52 eV. Bottom: 6 min NaCl (2 MLE) dosed while Ag(100) = 400 K. Contour plot taken at 122 K sample temperature and 638 nm. LEED image of hot sample dosing at 52 eV. Note the difference in time axis between the contour plots.

image potential state progression is observed, and peak structure for the long lived state B is also evident. The LEED image for 2 ML also shows smaller and more intense spots, indicating higher crystallinity and long range order. The data presented suggests that 2 ML islands are necessary to form the IPS and long-lived trap states.

5.3 Other Alkali Halides on Ag(100)

Next, we show that the IPS and long lived trap states exists not only for NaCl on different noble metal surfaces, but also for other alkali halides on noble metals. Shown in figure 5.6

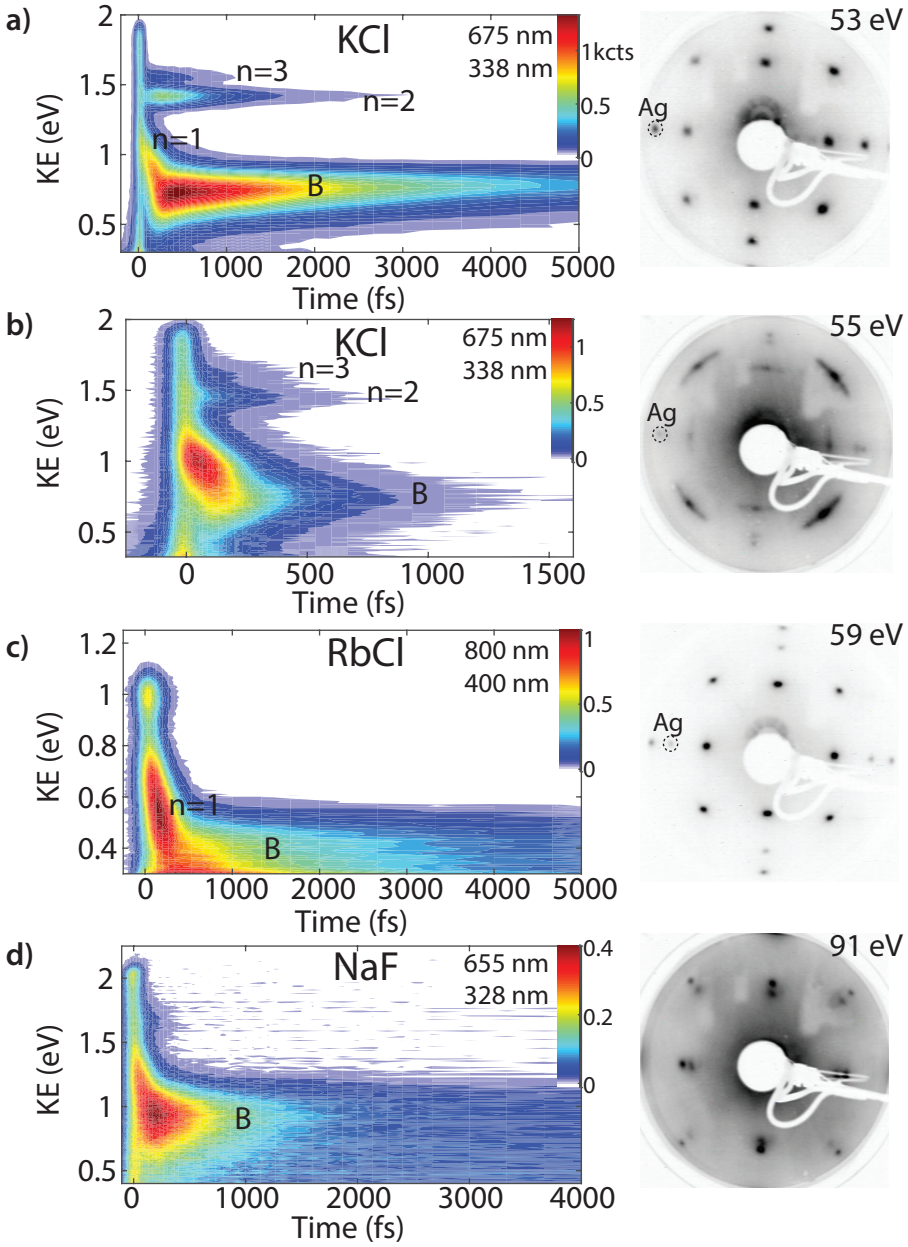

Figure 5.6: a) 16 min of KCl dosed at 773 K, with Ag substrate = 400 K during dosing. Spectra taken at 125 K and pump/probe wavelengths of 338/675 nm, respectively. LEED sample = 120 K and 53 eV. b) Same as (a), except Ag = 125 K during dosing. Note the difference in time axis for (a) and (b). c) 4 min RbCl dosed at 780 K, Ag = 400 K, spectra = 200 K, and pump/probe = 400/800 nm. LEED = 120 K and 59 eV beam. d) 50 min of NaF dosed at 900 K, Ag = 400 K, spectra = 120 K, pump/probe = 328/655 nm. LEED image is of 45 min NaF under same conditions. Image = 120 K and 91 eV beam.

are false color contour plots and corresponding LEED structure images for KCl, RbCl, and NaF on Ag(100). All the spectra are for uncalibrated dosing rate, however, the appearance of Ag(100) spots in LEED images indicate the ultrathin limit coverage. Growth of KCl on Ag(100) has been characterized by spot-profile-analysis low energy electron diffraction (SPA-LEED) and scanning tunneling microscopy (STM) in reference [118]. The growth modes of KCl and NaCl on Ag(100) show similar 3D island formation nucleating at Ag step edges; however, a few minor differences do exist. Whereas the lattice constant of NaCl on Ag(100) is a_{NaCl} = 3.99 Å, KCl on Ag(100) has a slightly larger lattice constant of a_{KCl} = 4.45 Å (a_{Ag100} = 2.89 Å) [119]. The resulting lattice mismatch of NaCl and KCl on Ag(100) is -2.5% and 9.9%, respectively. While both NaCl and KCl have incommensurate growth with Ag(100), KCl shows no rotational mosaicity of island alignment with the Ag(100) lattice that NaCl shows [118]. This can seen in figure 5.6(a), where the LEED image of KCl grown on a hot Ag(100) substrate shows high quality diffraction pattern with no spread in the (1,1) diffraction spots, whereas the NaCl diffraction patterns show the mosaic spread. This is not the case for KCl grown on cold Ag substrates (figure 5.6(b)), which do show a large mosaic spread. The band gaps of bulk NaCl and KCl are also quite similar, of $E_{g,NaCl}$ = 8.97 eV and $E_{g,KCl}$ = 8.69 eV [120]. Due to the structural and electronic similarity between these two systems, it should be no surprise they show similar ultrafast electron dynamics. Figure 5.6(a) shows a false color contour plot of KCl on Ag(100) grown under similar conditions to that presented in Chapter 3; however, the quantity is not calibrated; therefore, a quantitative comparison cannot be made. Nevertheless, the KCl shows clear evidence of the n = 1, 2, and 3 IPS of KCl. Note that the IPSs of clean Ag(100) are inaccessible at the wavelengths used. The dispersion of KCl, presented in Chapter 3, also shows clear evidence of the initially delocalized nature of the n = 1 IPS. At long time delays, the final localized trap state B (low coordinated defect sites) is also clearly evident.

Dosing KCl on cold substrates also shows a substantial impact on the electron dynamics similar to NaCl dosed under hot and cold conditions. While the n = 1-3 IPS and state B are still observed under cold dosing conditions, the lifetimes of all states are substantially reduced. This is likely due to island growth being primarily 1 ML (cold) versus 2 ML (hot), and therefore a reduced tunneling barrier back to the metal. While the lifetimes are reduced for both NaCl and KCl dosed on cold substrates, NaCl lacks the clear evidence of the n = 1-3 IPS peak structure compared to KCl. This could be due to either a smaller total amount of NaCl dosed in figure 5.5 versus KCl in 5.6(b), or it could arise from higher quality film growth observed for KCl. Future experiments done with careful dosing calibration are needed to solve this question.

Finally, excited state dynamics are shown for RCl and NaF in figure 5.6(c-d). Angle-resolved measurements for NaF are shown in Chapter 3, and angle-resolved measurements for RbCl are shown in figure 5.7. Both NaF and RbCl show a short-lived, dispersive n = 1 IPS and a long-lived, localized state. Note that experiments on RbCl used 400 nm and 800 nm wavelengths, thus predominately selectively exciting only the lowest lying n = 1 IPS. The long-lived localized state is still evident in the spectra, indicating many of the trapped electrons arise from the n = 1 IPS electrons. However, due to the red shifted probe wavelength,

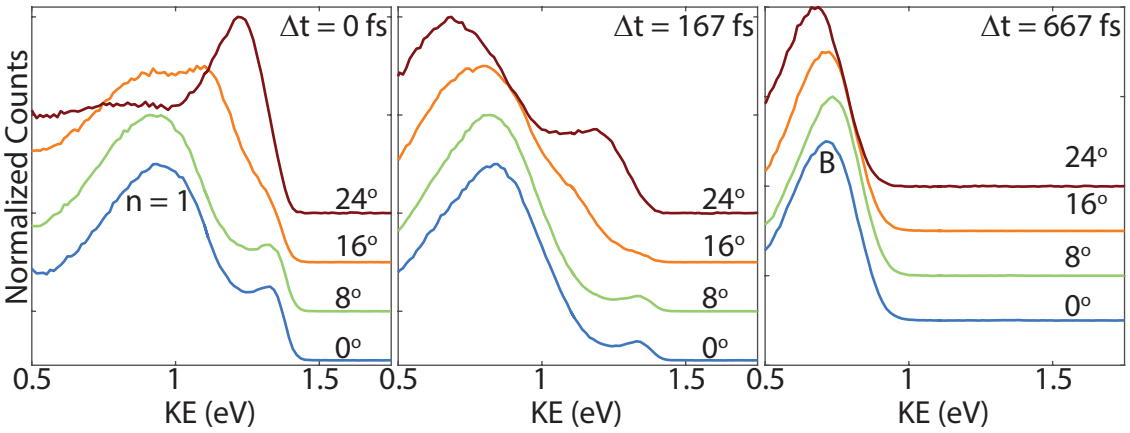

Figure 5.7: RbCl on Ag(100). Angle-resolved band structure measurements at time delays of 0 fs, 167 fs, and 667 fs of 4 min of RbCl dosed at 780 K, Ag = 400 K during dosing, spectra = 130 K, pump/probe = 400/800 nm.

the localized state overlaps with the low energy cutoff of the spectra. Also of note is the high quality LEED pattern for RbCl on Ag(100). Similar to KCl, RbCl shows no rotational mosaicity of island alignment with the Ag lattice. This indicates RbCl as a good candidate for studying electron dynamics with high quality films. Future experiments should note the roughly linear relationship with contact potential difference (change in workfunction) versus cation radius of alkali halides going through NaCl, KCl, RbCl, where RbCl has the largest contact potential difference [121]. A final note is that for NaF some evidence of sample degradation and sample charging were present. This could arise from slightly thicker films and larger band gap of NaF.

5.4 Low Temperatures: State C on Ag(111) and Cu(111)

In the last section, NaCl on Ag(111) will be shown, as well as the appearance of state C (polaron) for NaCl on Ag(111) and Cu(111). In chapter 2, LEED images of NaCl on Ag(100), Ag(111), and Cu(111) were compared. Whereas NaCl/Ag(100) showed preferential alignment of the NaCl(100) terminated islands with the Ag(100), on Ag(111), the diffraction pattern showed a ring pattern for NaCl, indicating a random orientation of NaCl islands with substrate. Despite the more random orientation of NaCl on Ag(111), the dynamics and dispersion again show very qualitatively similar behavior (figure 5.8). Upon initial excitation, a dispersive, n = 1 IPS with an effective mass $\approx 1m_e$ is observed. At intermediate time delays, a short-lived, localized state is observed at the bottom of the free electron band, and finally, at long time delays, the localized state B is observed with a negative effective mass of $\approx$ -1.5m_e. For comparison, state B's m^* on Ag(100) is -1.77m_e. However, one clear difference

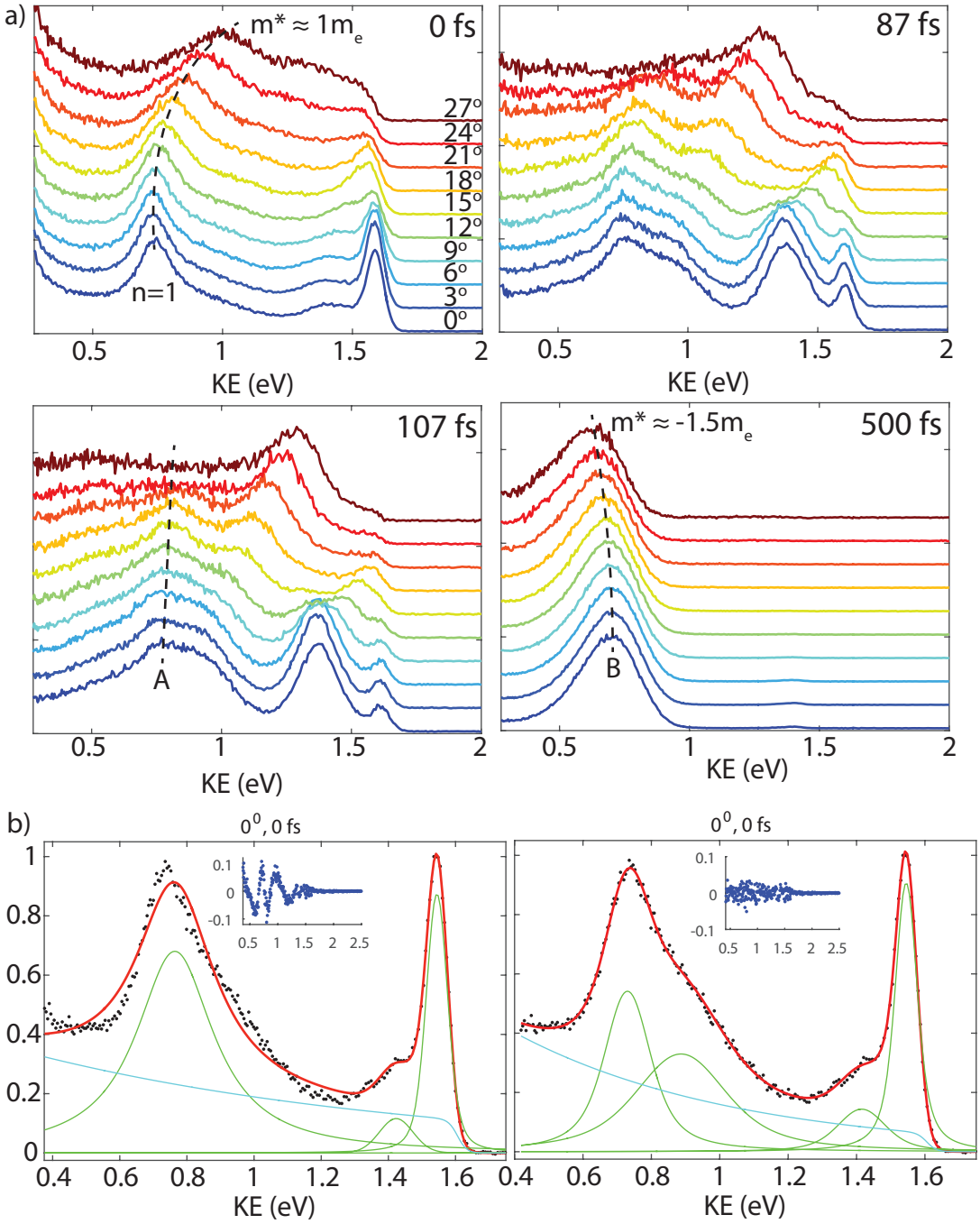

Figure 5.8: NaCl on Ag(111). a) Angle-resolved band structure measurements at time delays of 0 fs, 87 fs, 107 fs and 500 fs of 35 min of NaCl dosed at 775 K, Ag = 400 K during dosing, spectra = 130 K, pump/probe = 328/656 nm. b) Spectral fits to 21 min of NaCl(775K), Ag = (400K), spectra(130K). Fits are sum of Voigt functions and an exponential background convoluted with the Fermi-Dirac function. Inset shows residual errors of fit.

exists for the n = 1 IPS. On Ag(111), the n = 1 IPS shows a clear peak asymmetry, and at time delays of 50 - 100 fs, it appears as if there are two separate peaks for the n = 1 IPS. Figure 5.8(b) shows spectral fits for NaCl on Ag(111) at t = 0 fs and 0^o. The IPSs and SS are fit to Voigt functions, and the hot electron background to an exponential decay convoluted with a Fermi-Dirac function. The data reveals that adequate fitting of the spectra requires two Voigt functions to fit the n = 1 IPS. Both Voigt functions have an $m^* \approx 1m_e$ at t = 0 fs. One possible explanation is that there exist two different islands structures with different workfunctions. Another difference is that on Ag(100) and Cu(111), the n = 1 had an effective mass $< 1m_e$ and closer to the m^* of the conduction band of bulk NaCl. On Ag(111), the n = 1 IPS has an effective mass typically measured for IPS, i.e. $m^* = 1m_e$. However, further experiments are needed to address these issues.

The emergence of trap state C is also observed for NaCl on Ag(111), and shown in figure 5.9. Consistent with previous results, the state is only observed for temperatures $\ll$ 120 K and long time delays ($\geq$ 300 fs). The energetic difference between state B and C is 340 $\pm$ 40 meV, and in good agreement to that observed for Ag(100) of 380 meV. State C additionally shows a clear rise in intensity after the decay of state B, and substantially increased lifetime. Whereas state B decays $<$ 1 ps, state C has a decay lifetime of 17 ps (figure 5.9(c)). While this does appear to be longer than that observed for state C on Ag(100), a direct comparison cannot be made due to uncalibrated dosing conditions. The localized nature of state C is shown in figure 5.9(d), which reveals state C's dispersion to be independent of angle. However, due to its low kinetic energy and overlap with the low energy cutoff, a quantitative analysis of its effective mass is prevented.

Preliminary data to quantify the transition temperature for state C on Ag(111) is shown in figure 5.10. Individual time slices show the clear appearance and disappearance at 85 K and 95 K, respectively, for state C at long time delays. This is further demonstrate in figure 5.10(c), showing a zoom in on the kinetic energy region of state B and C at a long time delay of 2.3 ps. For temperatures of 67 K to 85 K, there is effectively no intensity of state B at this time delay. Heating the sample further to $\geq$ 95 K results in clear decrease in state C's intensity, and the reappearance of state B's population. Following a similar analysis used in Chapter 3, figure 5.10(d) shows the Voigt fitted amplitude difference between B and C at time delay of 2.3 ps as a function of temperature. Fitting this data to sigmoid shows the transition temperature for observing state C occurs between 85 K and 90 K, in good agreement with that quantified on Ag(100).

State C is also observed for NaCl on Cu(111) at low sample temperatures. Shown in figure 5.11 (a) and (b) is a log-scale false color contour plot of an ultrathin film of NaCl on Cu(111) at 65 K and 100 K, respectively. State C is clearly observed and long-lived at sample temperatures of 65 K, whereas at 100 K, state C is not evident. Similar to state C on Ag(111), state B shows a decrease in lifetime upon sample cooling as a result of state C opening a new pathway for decay. State C again shows a delayed rise in intensity after state's B maximum intensity. In agreement with state C on Ag(100) and Ag(111), state C on Cu(111) additionally shows a substantially enhanced lifetime compared to state B (26 ps versus 1.7 ps). In all observations of state C, a substantial increase in binding energy

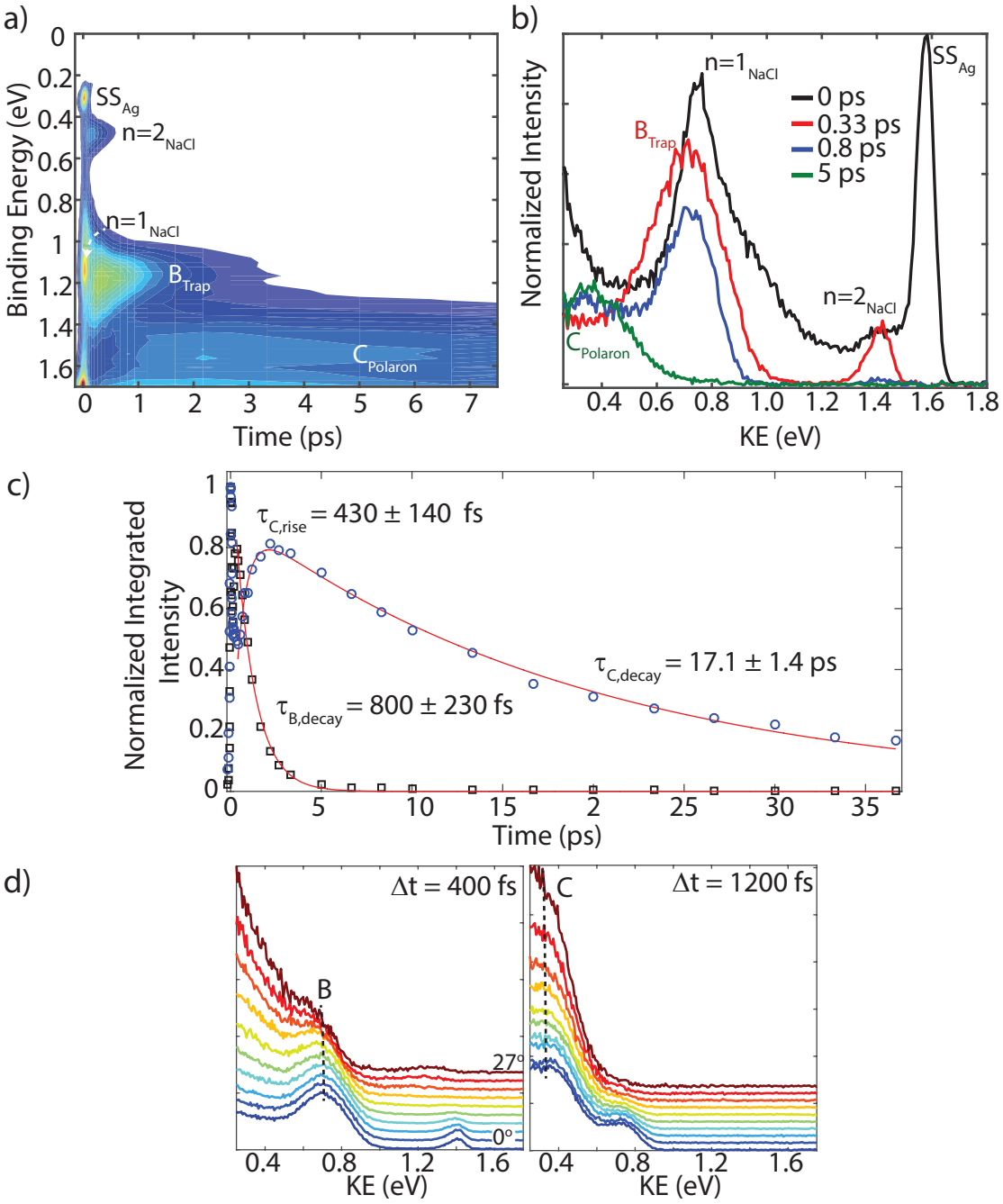

Figure 5.9: NaCl on Ag(111). a) Low temperature false color contour plot of 21 min NaCl (2-3 MLE) dosed at 775 K, Ag = 400 K, spectra = 67 K, 0^o, and pump/probe = 328/656 nm. b) Individual time slices of (a). c) Lifetime fits of trap states B and C of samples formed under the above conditions. Fits are to normalized integrated intensity using exponential decay and rise functions. d) Angle-resolved measurements of sample in (a) at time delays of 400 fs and 1200 fs.

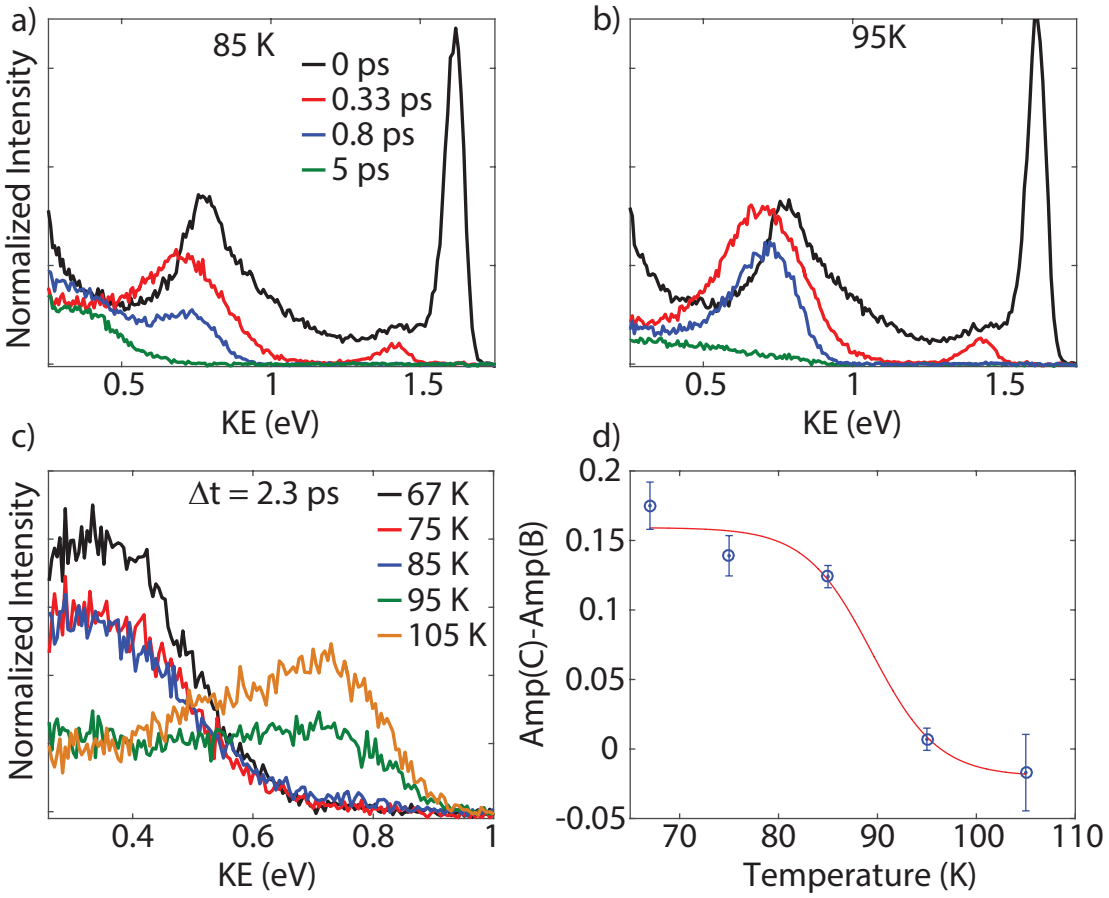

Figure 5.10: a) Times slices of sample in figure 5.9 at 85 K. b) Same as (a), but at 95 K. c) Zoom in on KE region of state B and C at time delay of 2.3 ps and various temperatures. d) Voigt fit amplitude difference of (c) and fit to sigmoid.

and lifetime for electrons trapped at low coordinated defect sites transferring to state C is found. The energy difference between state B and C on Cu(111) is 430 ± 20 meV at ≈ 70 K, in good agreement with that observed on silver substrates. Shown in figure 5.11 (d) and (c) are individual time slices of NaCl on Cu(111) aimed at providing preliminary quantification of the transition temperature. At 80 K, state C is observed with clear peak structure, primarily Gaussian in character, at low kinetic energies (high binding energies) and long time delays (> 500 fs). However, upon heating to 100 K, no peak structure and very minimal spectral intensity is observed for the energetic region of state C. This places the transition temperature in a very similar range as that observed for state C on Ag(111). Also of note is the increase in state C's amplitude at 1 ps compared to 0.5 ps, well after the instrument response function. This is also in agreement that state is populated by transfer of electrons from state B.

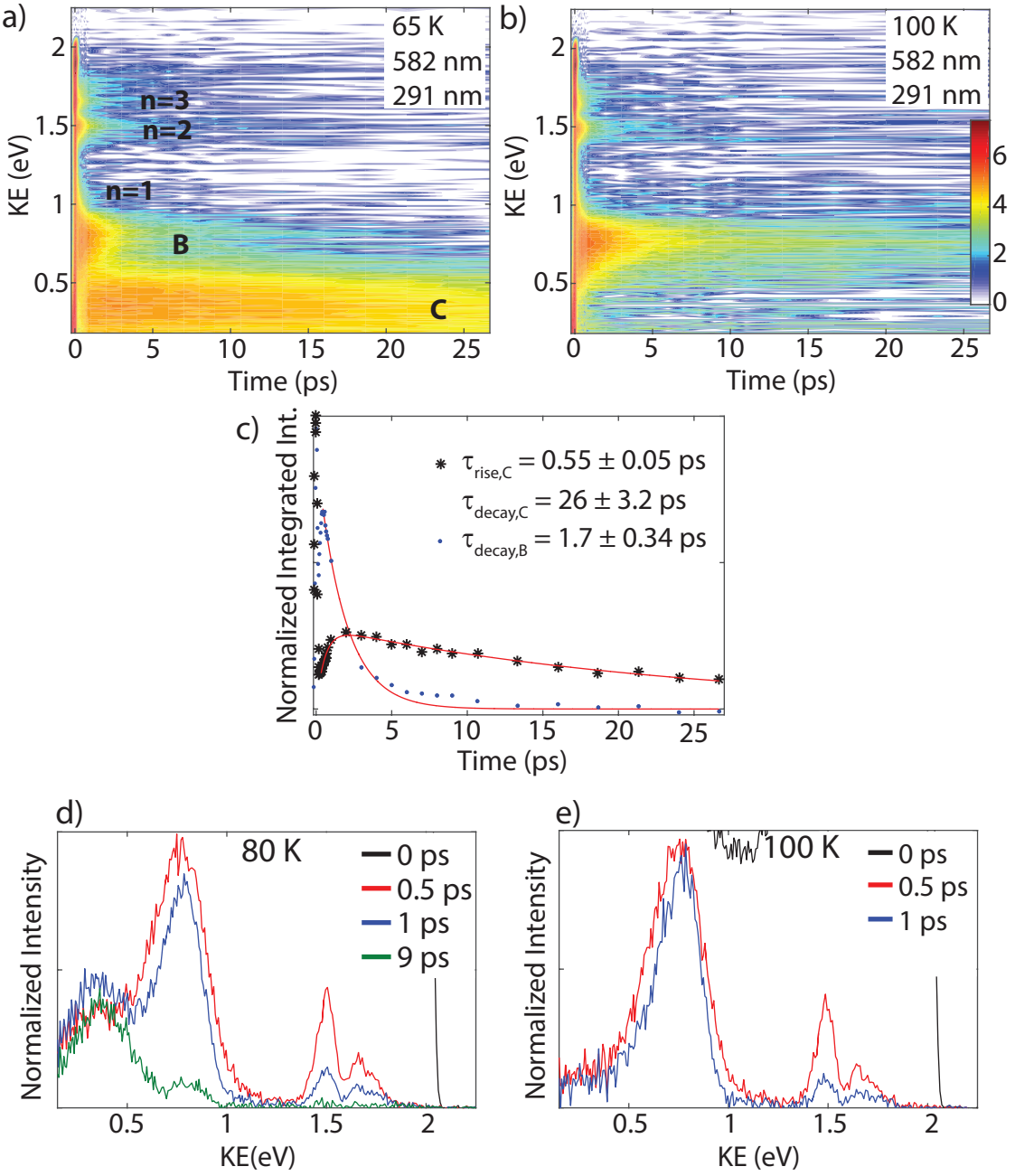

Figure 5.11: Log-scale false color contour plot of 26 min NaCl (790 K) on Cu(111) = 400 K during dosing, pump/probe = 291/582 nm, spectra = 65 K. b) Same as (a) but spectra = 100 K showing the disappearance of state C. c) Normalized 100 meV integrated population intensity window about peak center of (a) for states B and C versus time. Fits are to exponential decay and exponential rise and decay for B and C, respectively. d) and e) Time slices of sample (a) at 80 K and 100 K, respectively.

Chapter 6

Summary and Outlook

The work presented in this dissertation focuses on the excited states and ultrafast electron dynamics at alkali halide-metal interfaces. My initial work in the Harris group aimed at observing exciton dynamics in thin films of small molecule organic semiconductors (OSC), primarily α-ω-dihexyl-sexithiophene (DH6T) and 6,13-Bis(triisopropylsilylethynyl)pentacene (TIPS-pentacene). However, in both systems only the image potential states of the adsorbate were observed. The Harris group has spent many years attempting to observe excitonic states in organic semiconductor films, as these are the states relevant to molecular electronics and organic photovoltaics, but none have been observed. One idea to enable to the observation of the exciton was to insert an exciton blocking layer between the metal and the OSC film. This was the impetus for studying alkali halide thin films, the idea being that the alkali halide would decouple the exciton from the metal and prevent the metal from quenching the excitonic state. Fortuitously, the alkali halide-metal interface proved to be interesting and full of rich physics in its own right. Additionally, prior to the work in this dissertation, only one ultrafast study electron dynamics had been carried out on alkali halide-metal interfaces. To date, many of the studies of these interfaces have used scanning probe measurements which cannot track the real-time behavior of electrons at these interfaces. As detailed in the previous chapter, the conclusions between that in reference [73] and the Harris group are very different, and part of my efforts were aimed at resolving these discrepancies.

The primary system in this work were ultrathin films of NaCl on noble metal surfaces. Initial excitation resulted in the population of the image potential states of the NaCl-metal interface. The data and theoretical calculations also revealed that the IPS showed some mixed character with the conduction band of NaCl. After initial excitation, the delocalized n = 1 electrons, indicated by an $m^* \leq 1m_e$, were found to be localized through a series of discrete trap states on the hundreds of femtosecond timescale. The first of these was found at the bottom of the free IPS band and observed only at time delays of ca. 100 fs due to their lifetime being comparable to or less than the duration of the experimental cross correlation (100 fs). This state was assigned to energetic disorder induced localization, also termed Anderson localization. The second discrete localized state was observed at hundreds of meV increased binding energies and showed a delayed rise in intensity. The second localized state

was assigned to electron trapping at low coordinated defect sites on the NaCl surface such as corner sites, step edges, and NaCl pair vacancies, and had a substantially increased decay lifetime. The third discrete localized state was observed only at sample temperatures < 100 K. This third trap state resulted in an additional binding energy gain of ca. 400 meV and an additional increase in lifetime to multiple picoseconds. This final state was assigned to small polaron formation via defect intermediates.

These results were the first to observe the multiple deep trap states present at alkali halide-metal interfaces. As mentioned, much of the previous work has been done by scanning probe measurements, primarily scanning tunneling microscopy (STM). However, due to the dynamical trapping and ultrafast timescales of these states and localized nature of these states, it seems unlikely STM measurements are capable of observing these deep trap states. This was also the first observation of electron migration between multiple metastable localized trap states at two-dimensional interfaces. Furthermore, the work identified a fast and stable route to electron small polaron formation, where rather than direct formation of the polaron from the free electron state, the electron goes through a localized defect intermediate, enabling the formation of a small polaron. This is in contrast to the electron small polaron in defect-free bulk NaCl crystal which is known to be unstable.

This dissertation and that of Alex Shearer will represent the last full graduate students of Charles Harris. Wrapping up the Harris group's work on surface electron dynamics has certainly been an interesting and humbling experience. Charles has always claimed his greatest scientific legacy is his students, and I have had many interactions with other professors who have commented on the highest quality of his students. Living up to the legacy and accomplishments of the many graduate students and post-docs before me seems a certainly daunting and impossible task. As one of two of Charles's last students, this is also means there will be no further studies to follow up this work. As such, I want to outline to some of the future work I see valuable to pursue in hopes other groups might pursue and answer many outstanding questions.

The observation of an emerging discrete trap state only at low temperatures was a very interesting and perplexing result. An emerging state at low temperatures or electron migration between multiple metastable is a new phenomenon in two-photon photoemission studies, and as such offers much rewarding new physics to discover. While I made efforts to show these results were generalizable, the emerging trap at low temperatures has not yet been characterized in other alkali halide systems. Making direct comparisons between different alkali halides is complicated by the well characterized island growth of these systems and therefore non uniform samples. This results in an ensemble of islands with different concentrations of low-coordinated defect sites. However, some of these complications can be mitigated using a quartz crystal micro-balance to quantify sample dosing to allow precise and controlled quantities of each alkali halide to be studied. For comparable films of a series of alkali halides (NaCl, KCl, RbCl, KBr, NaF, etc.), it would interesting to compare the first trapping energy between the delocalized n = 1 IPS and electrons trapped at low coordinated defect sites. Specifically, one question would be does the trapping energy correlate to the cation series, as the first proposed deep trap site is electrons trapped in low

coordinate environments where they experience more cation electrostatic interaction. The next major question would address the existence of the emerging trap states for the alkali halide series. If the state should exist, the next question to answer would be the correlation with the transition temperature and the identity of the cation/anion pair. As this state was assigned to small polaron formation, it should follow the transition temperature should have some dependence on the cation/anion pair as this changes the vibrational frequencies of the lattice. However, this correlation would be complicated by the inherent change in bandgap and energetics associated with changing the cation/anion identities.

Conclusive assignment of the low temperature emerging trap state would be greatly aided by confirmation of the first deep trap state assigned to low coordinated defect sites. Complete theoretical calculation and simulations of the full experimental results are prohibitive due to the large-condensed matter phase of the system, the inherent disorder of the system and therefore non-repeating unit cell, and dynamical electron migration between delocalized excited states and localized trap states. However, the assignment of the defect trap states should be theoretically tractable but non-trivial by creating a NaCl island with terrace, corner, step edge, and NaCl pair vacancy sites, and placing an excess electron at each site and comparing the binding energies of the electron. If the first deep trap state can be conclusively assigned, the emerging trap state can more easily be determined as it forms from those electrons trapped at the initial deep trap state.

It would also be interesting to study the generalizability of these trap states to other insulating films, primarily metal-oxide films. Thin films of metal-oxides are interesting to study as they are more device-relevant to microelectronics and photo-catalytic reactions. Unfortunately, they are much harder to form, as noted in the dissertation of the former Harris group member James Johns, who attempted to grow thin films of MgO for many years to no avail.

Finally, future experiments should follow up with the impetus for studying this system in the the first place, i.e. having the alkali halide film serve as an exciton blocking layer. After forming the thin insulating film, a small molecule organic semiconductor can subsequently be dosed, and decoupled from the perturbative effects of the metal substrates. The decoupling ability of NaCl has already been established in many STM experiments on metal/2ML-NaCl/adsorbate systems outlined in Chapter 4. A very brief attempt was made in our group by dosing TIPS-pentacene on an ultrathin film of NaCl on Ag(100). No exciton was observed, and the spectrum contained minimal peak structure. However, it should be noted this was a very inhomogeneous system with bare patches of clean Ag, NaCl islands of different heights, and non-uniform coverage of TIPS-pentacene across the surface. This can be partially circumvented by growing NaCl or other alkali halide on high vicinal metal surfaces as opposed to low index Miller indice surfaces which can result in a more uniform covered surface. Growth of NaCl on vicinal surfaces has been studied for Au(11,12,12) [122], on Cu(532) which shows pyramid-like growth [123], and on Ag(1,1,19) [62]. Another interesting choice of substrate for future studies is Ge(100), which allows for epitaxial growth of NaCl and therefore minimal lattice mismatch and reduced lattice strain [124]. Additionally, many studies of adsorbates on insulating films have been characterized such as 3,4,9,10-

perylenetetracarboxylic diimide (PTCDI) and 1,4-bis-(2,4-diamino-1,3,5,-triazine)-benzene (BDATB) [122, 125], Copper-Octaethyl Porphyrin (CuOEP) [126], and fullerenes [127] to provide a few examples of potential future ultrafast studies.

Two-photon photoemission as an experimental technique still has much to offer in addressing questions and challenges facing both fundamental physics and future technologies. The last three decades of the TPPE experiments have transformed from surface states of clean metal surfaces, to surfaces covered with simple solvent molecules and small molecule organic semiconductors, to more complex systems such as donor/acceptor interfaces in organic photovoltaics, photocatalytic reactions, and other multi-component interfaces. One of the benefits to TPPE is its ability to study well characterized and controlled growth of homogenous samples. However, one of the challenges for this technique will be moving away from well controlled model systems to device-relevant interfaces, which will inherently be more heterogeneous and therefore complicate spectral dynamics. Studies can be greatly improved by scanning probe sample imaging with molecular resolution in-situ, something many TPPE groups have adapted. Many of the studies in this work would have greatly benefited from in-situ scanning tunneling microscopy or atomic force microscopy measurements of our samples.

Bibliography

[1] A. L. Linsebigler, G. Lu, and J. T. Yates. Photocatalysis on TiO2 Surfaces: Principles, Mechanisms, and Selected Results. *Chem. Rev.*, 95(3):735–758, 1995.

[2] M. Bonn, S. Funk, C. Hess, D. N. Denzler, C. Stampfl, M. Scheffler, M. Wolf, and G. Ertl. Phonon- Versus Electron-Mediated Desorption and Oxidation of CO on Ru(0001). *Science*, 285(5430):1042–1045, 1999.

[3] M. A. Fox and M. T. Dulay. Heterogeneous Photocatalysis. *Chem. Rev.*, 93(1):341–357, 1993.

[4] P. V. Kamat. Photochemistry on Nonreactive and Reactive (Semiconductor) Surfaces. *Chem. Rev.*, 93(1):267–300, 1993.

[5] S. C. Roy, O. K. Varghese, M. Paulose, and C. A. Grimes. Toward Solar Fuels: Photocatalytic Conversion of Carbon Dioxide to Hydrocarbons. *ACS Nano*, 4(3):1259–1278, 2010.

[6] D. Gust, T. A. Moore, and A. L Moore. Solar Fuels via Artificial Photosynthesis. *Acc. Chem. Res.*, 42(12):1890–1898, 2009.

[7] J.-L. Brédas, J. E. Norton, J. Cornil, and V. Coropceanu. Molecular Understanding of Organic Solar Cells: the Challenges. *Acc. Chem. Res.*, 42(11):1691–1699, 2009.

[8] T. M. Clarke and J. R. Durrant. Charge Photogeneration in Organic Solar Cells. *Chem. Rev.*, 110(11):6736–6767, 2010.

[9] A. A. Bakulin, A. Rao, V. G. Pavelyev, P. H. M. van Loosdrecht, M. S. Pshenichnikov, D. Niedzialek, J. Cornil, D. Beljonne, and R. H. Friend. The Role of Driving Energy and Delocalized States for Charge Separation in Organic Semiconductors. *Science*, 335(6074):1340–1344, 2012.

[10] A. E. Jailaubekov, A. P. Willard, J. R. Tritsch, W.-L. Chan, N. Sai, R. Gearba, Loren G. Kaake, K. J. Williams, K. Leung, P. J. Rossky, and X. Y. Zhu. Hot Charge-Transfer Excitons Set the Time Limit for Charge Separation at Donor/Acceptor Interfaces in Organic Photovoltaics. *Nat. Mater.*, 12(1):66–73, 2013.

[11] G. Grancini, M. Maiuri, D. Fazzi, A. Petrozza, H. J. Egelhaaf, D. Brida, G. Cerullo, and G. Lanzani. Hot Exciton Dissociation in Polymer Solar Cells. *Nat. Mater.*, 12(1):29–33, 2013.

[12] J. Lee, K. Vandewal, S. R. Yost, M. E. Bahlke, L. Goris, M. A. Baldo, J. V. Manca, and T. V. Voorhis. Charge Transfer State Versus Hot Exciton Dissociation in PolymerFullerene Blended Solar Cells. *J. Am. Chem. Soc.*, 132(34):11878–11880, 2010.

[13] S. R. Yost, L.-P. Wang, and T. Van Voorhis. Molecular Insight Into the Energy Levels at the Organic Donor/Acceptor Interface: A Quantum Mechanics/Molecular Mechanics Study. *J. Phys. Chem. C*, 115(29):14431–14436, 2011.

[14] G. Dutton and X. Y. Zhu. Unoccupied States in C60 Thin Films Probed by Two-Photon Photoemission. *J. Phys. Chem. B*, 106(23):5975–5981, 2002.

[15] Q. Zhong, C. Gahl, and M. Wolf. Two-Photon Photoemission Spectroscopy of Pyridine Adsorbed on Cu(111). *Surf. Sci.*, 496(12):21–32, 2002.

[16] M. Marks. *On the Dynamics of Electrons on Silver Single Crystal Surfaces, at Metal-Organic Interfaces, and in PTCDA-Monolayers*. Philipps-Universität Marburg, 2013.

[17] E. Varene, L. Bogner, C. Bronner, and P. Tegeder. Ultrafast Exciton Population, Relaxation, and Decay Dynamics in Thin Oligothiophene Films. *Phys. Rev. Lett.*, 109(20):207601, 2012.

[18] E. Varene, I. Martin, and P. Tegeder. Optically Induced Inter- and Intrafacial Electron Transfer Probed by Two-Photon Photoemission: Electronic States of Sexithiophene on Au(111). *J. Phys. Chem. Lett.*, 2(3):252–256, 2011.

[19] R. Hoffmann. How Chemistry and Physics Meet in the Solid State. *Angew. Chem. Int. Ed.*, 26(9):846–878, 1987.

[20] T. Ichibayashi and K. Tanimura. Identification of the Conduction-Band Photoemission in Time-Resolved Two-Photon Photoemission Spectroscopy of Si Surfaces. *Phys. Rev. B*, 75(23):235327, 2007.

[21] Gahl, C. and Bovensiepen, U. and Frischkorn, C. and Wolf, M. Ultrafast dynamics of electron localization and solvation in ice layers on cu(111). *Phys. Rev. Lett.*, 89(10):107402, 2002.

[22] J. Stähler, J.-C. Deinert, D. Wegkamp, S. Hagen, and M. Wolf. Real-Time Measurement of the Vertical Binding Energy during the Birth of a Solvated Electron. *J. Am. Chem. Soc.*, 137(10):3520–3524, 2015.

[23] Y. H. Wang, D. Hsieh, E. J. Sie, H. Steinberg, D. R. Gardner, Y. S. Lee, P. Jarillo-Herrero, and N. Gedik. Measurement of Intrinsic Dirac Fermion Cooling on the Surface of the Topological Insulator Bi_2Se_3 Using Time-Resolved and Angle-Resolved Photoemission Spectroscopy. *Phys. Rev. Lett.*, 109(12):127401, 2012.

[24] M. Hajlaoui, E. Papalazarou, J. Mauchain, G. Lantz, N. Moisan, D. Boschetto, Z. Jiang, I. Miotkowski, Y. P. Chen, A. Taleb-Ibrahimi, L. Perfetti, and M. Marsi. Ultrafast Surface Carrier Dynamics in the Topological Insulator Bi2Te3. *Nano Lett.*, 12(7):3532–3536, 2012.

[25] J. Reimann, J. Güdde, K. Kuroda, E. V. Chulkov, and U. Höfer. Spectroscopy and Dynamics of Unoccupied Electronic States of the Topological Insulators Sb_2Te_3 and Sb_2Te_2S. *Phys. Rev. B*, 90(8):081106, 2014.

[26] W. Shockley. On the Surface States Associated with a Periodic Potential. *Phys. Rev.*, 56(4):317–323, 1939.

[27] N. Ashcroft and D. Mermin. *Solid State Physics*. Thomson Learning, 1976.

[28] S. Grothe, S. Johnston, Shun Chi, P. Dosanjh, S. A. Burke, and Y. Pennec. Quantifying Many-Body Effects by High-Resolution Fourier Transform Scanning Tunneling Spectroscopy. *Phys. Rev. Lett.*, 111(24):246804, 2013.

[29] F. Reinert, G. Nicolay, S. Schmidt, D. Ehm, and S. Hüfner. Direct Measurements of the L -Gap Surface States on the (111) Face of Noble Metals by Photoelectron Spectroscopy. *Phys. Rev. B*, 63(11):115415, 2001.

[30] S. D. Kevan and R. H. Gaylord. High-Resolution Photoemission Study of the Electronic Structure of the Noble-Metal (111) Surfaces. *Phys. Rev. B*, 36(11):5809–5818, 1987.

[31] B. Reihl, K. H. Frank, and R. R. Schlittler. Image-Potential and Intrinsic Surface States on Ag(100). *Phys. Rev. B*, 30(12):7328–7331, 1984.

[32] M. W. Cole and M. H. Cohen. Image-Potential-Induced Surface Bands in Insulators. *Phys. Rev. Lett.*, 23(21):1238–1241, 1969.

[33] C. C. Grimes and T. R. Brown. Direct Spectroscopic Observation of Electrons in Image-Potential States Outside Liquid Helium. *Phys. Rev. Lett.*, 32(6):280–283, 1974.

[34] P. M. Echenique and J. B. Pendry. The Existence and Detection of Rydberg States at Surfaces. *J. Phys. C*, 11(10):2065, 1978.

[35] T. Fauster and W. Steinmann. *Chapter 8 - TWO-PHOTON PHOTOEMISSION SPECTROSCOPY OF IMAGE STATES*, pages 347–411. Elsevier, Amsterdam, 1995.

[36] P. M. Echenique, J. M. Pitarke, E. V. Chulkov, and V. M. Silkin. Image-Potential-Induced States at Metal Surfaces. *J. Electron. Spectrosc. Relat. Phenom.*, 126(13):163–175, 2002.

[37] P. M. Echenique, R. Berndt, E. V. Chulkov, T. Fauster, A. Goldmann, and U. Höfer. Decay of Electronic Excitations at Metal Surfaces. *Surf. Sci. Rep.*, 52(78):219–317.

[38] E. V. Chulkov, V. M. Silkin, and P. M. Echenique. Image Potential States on Metal Surfaces: Binding Energies and Wave Functions. *Surf. Sci.*, 437(3):330–352, 1999.

[39] E. V. Chulkov, A. G. Borisov, J. P. Gauyacq, D. Sánchez-Portal, V. M. Silkin, V. P. Zhukov, and P. M. Echenique. Electronic Excitations in Metals and at Metal Surfaces. *Chem. Rev.*, 106(10):4160–4206, 2006.

[40] G. Dutton, J. Pu, G. Truhlar, and X.-Y. Zhu. Lateral Confinement of Image Electron Wave Function by an Interfacial Dipole Lattice. *J. Chem. Phys.*, 118(10):4337–4340, 2003.

[41] K. J. Gaffney, C. M. Wong, S. H. Liu, A. D. Miller, J. D. McNeill, and C. B. Harris. Femtosecond Electron Dynamics at the Benzene/Ag(111) Interface. *Chem. Phys.*, 251(13):99–110, 2000.

[42] A. Miller. *Femtosecond Studies of Electron Dynamics and Structure at Metal-Molecular Interfaces*. University of California, Berkeley, 2002.

[43] C. B. Harris, N. H. Ge, R. L. Lingle, J. D. McNeill, and C. M. Wong. Femtosecond Dynamics of Electrons on Surfaces and at Interfaces. *Ann. Rev. Phys. Chem.*, 48(1):711–744, 1997.

[44] U. Bovensiepen, C. Gahl, J. Stähler, M. Bockstedte, M. Meyer, F. Baletto, S. Scandolo, X. Y. Zhu, A. Rubio, and M. Wolf. A Dynamic Landscape from Femtoseconds to Minutes for Excess Electrons at IceMetal Interfaces. *J. Phys. Chem. C*, 113(3):979–988, 2009.

[45] J. Stähler, M. Mehlhorn, U. Bovensiepen, M. Meyer, D. O. Kusmierek, K. Morgenstern, and M. Wolf. Impact of Ice Structure on Ultrafast Electron Dynamics in D_2O Clusters on Cu(111). *Phys. Rev. Lett.*, 98(20):206105, 2007.

[46] J. T. Devreese. *Polarons*. WILEY-VCH Verlag GmbH Co KGaA, 2003.

[47] N.-H. Ge, C. M. Wong, R. L. Lingle, J. D. McNeill, K. J. Gaffney, and C. B. Harris. Femtosecond Dynamics of Electron Localization at Interfaces. *Science*, 279(5348):202–205, 1998.

[48] J. E. Johns, E. A. Muller, J. M. J. Frechet, and C. B. Harris. The Origin of Charge Localization Observed in Organic Photovoltaic Materials. *J. Am. Chem. Soc.*, 132(44):15720–15725, 2010.

[49] E. A. Muller, M. L. Strader, J. E. Johns, A. Yang, B. W. Caplins, A. J. Shearer, D. E. Suich, and C. B. Harris. Femtosecond Electron Solvation at the Ionic Liquid/Metal Electrode Interface. *J. Am. Chem. Soc.*, 135(29):10646–10653, 2013.

[50] A. J. Shearer, D. E. Suich, B. W. Caplins, and C. B. Harris. Impact of Film Thickness and Temperature on Ultrafast Excess Charge Dynamics in Ionic Liquid Films. *J. Phys. Chem. C*, 119(43):24417–24424, 2015.

[51] W. Merry, Jr. *Image Potential States at Metal-Dielectric Interfaces*. University of California, Berkeley, 1992.

[52] J. McNeill. *Ultrafast Dynamics of Electrons at Interfaces*. University of California, Berkeley, 1999.

[53] B. Caplins. *Electronic Structure of the Metal/Phthalocyanine Interface Probed by Two-Photon Photoemission*. University of California, Berkeley, 2014.

[54] K. Giesen, F. Hage, F. J. Himpsel, H. J. Riess, W. Steinmann, and N. V. Smith. Effective Mass of Image-Potential States. *Phys. Rev. B*, 35(3):975–978, 1987.

[55] K. Giesen, F. Hage, F. J. Himpsel, H. J. Riess, and W. Steinmann. Binding Energy of Image-Potential States: Dependence on Crystal Structure and Material. *Phys. Rev. B*, 35(3):971–974, 1987.

[56] S. Schuppler, N. Fischer, T. Fauster, and W. Steinmann. Bichromatic Two-Photon Photoemission Spectroscopy of Image Potential States on Ag(100). *Appl. Phys. A*, 51(4):322–326, 1990.

[57] K. Duncker, M. Kiel, and W. Widdra. Momentum-Resolved Lifetimes of Image-Potential States on Ag(001). *Surf. Sci.*, 606(2122):L87–L90, 2012.

[58] I. L. Shumay, U. Höfer, C. Reuß, U. Thomann, W. Wallauer, and T. Fauster. Lifetimes of Image-Potential States on Cu(100) and Ag(100) Measured by Femtosecond Time-Resolved Two-Photon Photoemission. *Phys. Rev. B*, 58(20):13974–13981, 1998.

[59] R. W. Schoenlein, J. G. Fujimoto, G. L. Eesley, and T. W. Capehart. Femtosecond Relaxation Dynamics of Image-Potential States. *Phys. Rev. B*, 43(6):4688–4698, 1991.

[60] E. Muller. *Electron Dynamics and Symmetries at the Metal-Molecule Interface Probed by Two Photon Photoemission*. University of California, Berkeley, 2012.

[61] G. Cabailh, C. R Henry, and C. Barth. Thin NaCl Films on Silver (001): Island Growth and Work Function. *New J. Phys.*, 14(10):103037, 2012.

[62] J. Kramer, C. Tegenkamp, and H. Pfnür. The Growth of NaCl on Flat and Stepped Silver Surfaces. *J. Phys.: Condens. Matter*, 15(38):6473, 2003.

[63] M. Friederike, H. Sarah, B. Konrad, B. Cord, S. Ali, H. Jörg, and M. Karina. Coulomb Attraction During the Carpet Growth Mode of NaCl. *J. Phys.: Condens. Matter*, 24(35):354006, 2012.

[64] M. Pivetta, F. Patthey, M. Stengel, A. Baldereschi, and W.-D. Schneider. Local Work Function Moire Pattern on Ultrathin Ionic Films: NaCl on Ag(100). *Phys. Rev. B*, 72(11):115404, 2005.

[65] H.-C. Ploigt, C. Brun, M. Pivetta, F. Patthey, and W.-D. Schneider. Local Work Function Changes Determined by Field Emission Resonances: NaCl/Ag(100). *Phys. Rev. B*, 76(19):195404, 2007.

[66] R. Bennewitz, V. Barwich, M. Bammerlin, C. Loppacher, M. Guggisberg, A. Baratoff, E. Meyer, and H. J. Güntherodt. Ultrathin Films of NaCl on Cu(111): a LEED and Dynamic Force Microscopy Study. *Surf. Sci.*, 438(13):289–296, 1999.

[67] C. Bombis, F. Ample, L. Lafferentz, H. Yu, S. Hecht, C. Joachim, and L. Grill. Single Molecular Wires Connecting Metallic and Insulating Surface Areas. *Angew. Chem. Int. Ed.*, 48(52):9966–9970, 2009.

[68] M. G. Walter, E. L. Warren, J. R. McKone, S. W. Boettcher, Q. Mi, El. A. Santori, and N. S. Lewis. Solar Water Splitting Cells. *Chem. Rev.*, 110(11):6446–6473, 2010.

[69] C. J. Brabec, S. E. Shaheen, C. Winder, N. S. Sariciftci, and P. Denk. Effect of LiF/Metal Electrodes on the Performance of Plastic Solar Cells. *Appl. Phys. Lett.*, 80(7):1288–1290, 2002.

[70] J. Repp, G. Meyer, F. E. Olsson, and M. Persson. Controlling the Charge State of Individual Gold Adatoms. *Science*, 305(5683):493–495, 2004.

[71] L. Gross, N. Moll, F. Mohn, A. Curioni, G. Meyer, F. Hanke, and M. Persson. High-Resolution Molecular Orbital Imaging Using a p-Wave STM Tip. *Phys. Rev. Lett.*, 107(8):086101, 2011.

[72] O. Guillermet, S. Gauthier, C. Joachim, P. de Mendoza, T. Lauterbach, and A. Echavarren. STM and AFM High Resolution Intramolecular Imaging of a Single Decastarphene Molecule. *Chem. Phys. Lett.*, 511(46):482–485, 2011.

[73] M. Muntwiler and X. Y. Zhu. Formation of Two-Dimensional Polarons that are Absent in Three-Dimensional Crystals. *Phys. Rev. Lett.*, 98(24):246801, 2007.

[74] E. Le Moal, M. Müller, O. Bauer, and M. Sokolowski. Misfit Driven Azimuthal Orientation of NaCl Domains on Ag(100). *Surf. Sci.*, 603(16):2434–2444, 2009.

[75] S. Díaz-Tendero, A. G. Borisov, and J.-P. Gauyacq. Theoretical Study of the Electronic Excited States in Ultrathin Ionic Layers Supported on Metal Surfaces: NaCl/Cu(111). *Phys. Rev. B*, 83(11):115453, 2011.

[76] L. Sementa, A. Marini, G. Barcaro, F. R. Negreiros, and A. Fortunelli. Electronic Excited States at Ultrathin Dielectric-Metal Interfaces. *Phys. Rev. B*, 88(12):125413, 2013.

[77] L. J. Page and E. H. Hygh. Calculation of Energy Bands in Alkali Halides. *Phys. Rev. B*, 1(8):3472–3479, 1970.

[78] J. D. McNeill, R. L. Lingle, R. E. Jordan, D. F. Padowitz, and C. B. Harris. Interfacial Quantum Well States of Xe and Kr Adsorbed on Ag(111). *J. Chem. Phys.*, 105(9):3883–3891, 1996.

[79] U. Bovensiepen, C. Gahl, and M. Wolf. Solvation Dynamics and Evolution of the Spatial Extent of Photoinjected Electrons in D2O/Cu(111). *J. Phys. Chem. B*, 107(33):8706–8715, 2003.

[80] A. Nitzan. *Chemical Dynamics in Condensed Phases: Relaxation, Transfer and Reactions in Condensed Molecular Systems: Relaxation, Transfer and Reactions in Condensed Molecular Systems*. Oxford University Press, 2006.

[81] J. Stähler, M. Meyer, D. O. Kusmierek, U. Bovensiepen, and M. Wolf. Ultrafast Electron Transfer Dynamics at NH3/Cu(111) Interfaces: Determination of the Transient Tunneling Barrier. *J. Am. Chem. Soc.*, 130(27):8797–8803, 2008.

[82] R. T. Poole, J. G. Jenkin, J. Liesegang, and R. C. G. Leckey. Electronic Band Structure of the Alkali Halides. I. Experimental Parameters. *Phys. Rev. B*, 11(12):5179–5189, 1975.

[83] U. Barjenbruch, S. Fölsch, and M. Henzler. Surface States on Epitaxial Thin Films of NaCl and KCl. *Surf. Sci.*, 211212(0):749–758, 1989.

[84] R. Fischer, T. Fauster, and W. Steinmann. Three-Dimensional Localization of Electrons on Ag Islands. *Phys. Rev. B*, 48(20):15496–15499, 1993.

[85] C. Tegenkamp, H. Pfnür, W. Ernst, U. Malaske, J. Wollschläger, D. Peterka, K. M. Schröder, V. Zielasek, and M. Henzler. Defects in Epitaxial Insulating Thin Films. *J. Phys.: Condens. Matter*, 11(49):9943, 1999.

[86] G. Pacchioni and H. Freund. Electron Transfer at Oxide Surfaces. The MgO Paradigm: from Defects to Ultrathin Films. *Chem. Rev.*, 113(6):4035–4072, 2013.

[87] K. P. McKenna and A. L. Shluger. Electron-Trapping Polycrystalline Materials with Negative Electron Affinity. *Nat. Mater.*, 7(11):859–862, 2008.

[88] J. Repp, G. Meyer, S. Paavilainen, F. E. Olsson, and M. Persson. Scanning Tunneling Spectroscopy of Cl Vacancies in NaCl Films: Strong Electron-Phonon Coupling in Double-Barrier Tunneling Junctions. *Phys. Rev. Lett.*, 95(22):225503–4, 2005.

[89] P. Xia, Naichang Yu, and L. A. Bloomfield. Experimental and Theoretical Studies of Single Excess Electrons in Sodium Chloride Cluster Anions. *Phys. Rev. B*, 47(15):10040–10043, 1993.

[90] J. Repp, G. Meyer, S. M. Stojković, A. Gourdon, and C. Joachim. Molecules on Insulating Films: Scanning-Tunneling Microscopy Imaging of Individual Molecular Orbitals. *Phys. Rev. Lett.*, 94(2):026803, 2005.

[91] J. Vogt. Tensor LEED Study of the Temperature Dependent Dynamics of the NaCl(100) Single Crystal Surface. *Phys. Rev. B*, 75(12):125423, 2007.

[92] C. J. Powell and A. Jablonski. NIST Electron Effective-Attenuation-Length Database - Version 1.3. Technical report.

[93] A. Tekiel, Y. Miyahara, J. M. Topple, and P. Grutter. Room-Temperature Single-Electron Charging Detected by Electrostatic Force Microscopy. *ACS Nano*, 7(5):4683–4690, 2013.

[94] W. Steurer, J. Repp, L. Gross, I. Scivetti, M. Persson, and G. Meyer. Manipulation of the Charge State of Single Au Atoms on Insulating Multilayer Films. *Phys. Rev. Lett.*, 114(3):036801, 2015.

[95] A. Safiei, J. Henzl, and K. Morgenstern. Isomerization of an Azobenzene Derivative on a Thin Insulating Layer by Inelastically Tunneling Electrons. *Phys. Rev. Lett.*, 104(21):216102, 2010.

[96] P. Liljeroth, J. Repp, and G. Meyer. Current-Induced Hydrogen Tautomerization and Conductance Switching of Naphthalocyanine Molecules. *Science*, 317(5842):1203–1206, 2007.

[97] F. Mohn, L. Gross, N. Moll, and G. Meyer. Imaging the Charge Distribution within a Single Molecule. *Nat. Nano.*, 7(4):227–231, 2012.

[98] C. Brun, K. H. Müller, I. P. Hong, F. Patthey, C. Flindt, and W.-D. Schneider. Dynamical Coulomb Blockade Observed in Nanosized Electrical Contacts. *Phys. Rev. Lett.*, 108(12):126802, 2012.

[99] D. E. Suich, B. W. Caplins, A. J. Shearer, and C. B. Harris. Femtosecond Trapping of Free Electrons in Ultrathin Films of NaCl on Ag(100). *J. Phys. Chem. Lett.*, 5(17):3073–3077, 2014.

[100] U. Höfer, I. L. Shumay, C. Reuß, U. Thomann, W. Wallauer, and T. Fauster. Time-Resolved Coherent Photoelectron Spectroscopy of Quantized Electronic States on Metal Surfaces. *Science*, 277(5331):1480–1482, 1997.

[101] A. L. Shluger and A. M. Stoneham. Small Polarons in Real Crystals: Concepts and Problems. *J. Phys.: Condens. Matter*, 5(19):3049, 1993.

[102] R. Bennewitz, A. S. Foster, L. N. Kantorovich, M. Bammerlin, C. Loppacher, S. Schär, M. Guggisberg, E. Meyer, and A. L. Shluger. Atomically Resolved Edges and Kinks of NaCl Islands on Cu(111): Experiment and Theory. *Phys. Rev. B*, 62(3):2074–2084, 2000.

[103] J. Repp, S. Fölsch, G. Meyer, and K.-H. Rieder. Ionic Films on Vicinal Metal Surfaces: Enhanced Binding due to Charge Modulation. *Phys. Rev. Lett.*, 86(2):252–255, 2001.

[104] J. Repp, G. Meyer, and K.-H. Rieder. Snell's Law for Surface Electrons: Refraction of an Electron Gas Imaged in Real Space. *Phys. Rev. Lett.*, 92(3):036803, 2004.

[105] A. J. Fisher, W. Hayes, and D. S. Wallace. Polarons and Solitons. *J. Phys.: Condens. Matter*, 1(33):5567, 1989.

[106] A. M. Stoneham, J. Gavartin, A. L. Shluger, A. V. Kimmel, D. Muñoz Ramo, H. M. Rnnow, G. Aeppli, and C. Renner. Trapping, Self-Trapping and the Polaron Family. *J. Phys.: Condens. Matter*, 19(25):255208, 2007.

[107] D. Emin and T. Holstein. Adiabatic Theory of an Electron in a Deformable Continuum. *Phys. Rev. Lett.*, 36(6):323–326, 1976.

[108] G. Kalosakas, S. Aubry, and G. P. Tsironis. Polaron Solutions and Normal-Mode Analysis in the Semiclassical Holstein Model. *Phys. Rev. B*, 58(6):3094–3104, 1998.

[109] G. Kalosakas and I. Bezel. Electron Dynamics in Two-Dimensions: a Hunt for the Ground-State Polarons. *Chem. Phys. Lett.*, 403(13):89–94, 2005.

[110] D. Emin and M. N. Bussac. Disorder-Induced Small-Polaron Formation. *Phys. Rev. B*, 49(20):14290–14300, 1994.

[111] A. L. Shluger and J. D. Gale. One-Center Trapping of the Holes in Alkali Halide Crystals. *Phys. Rev. B*, 54(2):962–969, 1996.

[112] S. Iwai, T. Tokizaki, A. Nakamura, K. Tanimura, N. Itoh, and A. Shluger. One-Center Small Polarons as Short-Lived Precursors in Self-Trapping Processes of Holes and Electron-Hole Pairs in Alkali Iodides. *Phys. Rev. Lett.*, 76(10):1691–1694, 1996.

[113] J. P. Hague, P. E. Kornilovitch, and A. S. Alexandrov. Trapping of Lattice Polarons by Impurities. *Phys. Rev. B*, 78(9):092302, 2008.

[114] N. Yu, P. Xia, L. A. Bloomfield, and M. Fowler. Structure and Electron Localization of Anionic NaCl Clusters with Excess Electrons. *J. Chem. Phys.*, 102(12):4965–4972, 1995.

[115] I. Scivetti and M. Persson. A Simplified Density Functional Theory Method for Investigating Charged Adsorbates on an Ultrathin, Insulating Film Supported by a Metal Substrate. *J. Phys.: Condens. Matter*, 26(13):135003, 2014.

[116] C. M. Lee, S. W. Gu, and C. C. Lam. Temperature Dependence of Strongly Coupled Surface Polaron in Potassium Iodide Semi-Infinite Polar Crystal. *Physica B*, 229(34):361–368, 1997.

[117] D. Muñoz Ramo, A. L. Shluger, J. L. Gavartin, and G. Bersuker. Theoretical Prediction of Intrinsic Self-Trapping of Electrons and Holes in Monoclinic HfO_2. *Phys. Rev. Lett.*, 99(15):155504, 2007.

[118] M. Müller, J. Ikonomov, and M. Sokolowski. Structure of Epitaxial Layers of KCl on Ag(100). *Surf. Sci.*, 605(1112):1090–1094, 2011.

[119] E. Le Moal, M. Müller, O. Bauer, and M. Sokolowski. Stable and Metastable Phases of PTCDA on Epitaxial NaCl Films on Ag(100). *Phys. Rev. B*, 82(4):045301, 2010.

[120] D. M. Roessler and W. C. Walker. Electronic Spectra of Crystalline NaCl and KCl. *Phys. Rev.*, 166(3):599–606, 1968.

[121] L. Christian, Z. Ulrich, and M. E. Lukas. Kelvin Probe Force Microscopy of Alkali Chloride Thin Films on Au(111). *Nanotechnology*, 15(2):S9, 2004.

[122] M. E. Cañas Ventura, W. Xiao, P. Ruffieux, R. Rieger, K. Müllen, H. Brune, and R. Fasel. Stabilization of Bimolecular Islands on Ultrathin NaCl Films by a Vicinal Substrate. *Surf. Sci.*, 603(15):2294–2299, 2009.

[123] S. Fölsch, A. Riemann, J. Repp, G. Meyer, and K. H. Rieder. From Atomic Kinks to Mesoscopic Surface Patterns: Ionic Layers on Vicinal Metal Surfaces. *Phys. Rev. B*, 66(16):161409, 2002.

[124] K. Glöckler, M. Sokolowski, A. Soukopp, and E. Umbach. Initial Growth of Insulating Overlayers of NaCl on Ge(100) Observed by Scanning Tunneling Microscopy with Atomic Resolution. *Phys. Rev. B*, 54(11):7705–7708, 1996.

[125] X. Sun and F. Silly. NaCl Islands Decorated with 2D or 3D 3,4,9,10-Perylene-Tetracarboxylic-Dianhydride Nanostructures. *Appl. Surf. Sci.*, 256(7):2228–2231, 2010.

[126] L. Ramoino, M. von Arx, S. Schintke, A. Baratoff, H. J. Güntherodt, and T. A. Jung. Layer-Selective Epitaxial Self-Assembly of Porphyrins on Ultrathin Insulators. *Chem. Phys. Lett.*, 417(13):22–27, 2006.

[127] F. Rossel, M. Pivetta, F. Patthey, E. Ćavar, A. P. Seitsonen, and W.-D. Schneider. Growth and Characterization of Fullerene Nanocrystals on NaCl/Au(111). *Phys. Rev. B*, 84(7):075426, 2011.